TECHNICAL REPORT C&OM-5

ARMOR MATERIALS RESEARCH

Part I

Proceedings of a
Meeting of Armor Materials Research Contractors
19-20 May 1964

AUGUST 1965

U. S. ARMY NATICK LABORATORIES
Natick Massachusetts

TECHNICAL REPORT
C&OM-5

ARMOR MATERIALS RESEARCH

Part I

Proceedings of a

Meeting of Armor Materials Research Contractors
U. S. Army Natick Laboratories
Natick, Massachusetts
May 19-20, 1964

June 1965

U. S. Army Materiel Command
U. S. ARMY NATICK LABORATORIES
Natick, Massachusetts

BLANK PAGE

FOREWORD

The United States Army Natick Laboratories called a meeting of its contractors who are conducting research on armor penetration or the development of armor materials and its own personnel who are likewise engaged. Other scientists and technologists from the government laboratories were invited to attend and to participate in the discussions. The objectives of the meeting were not only to present past work and recent progress but to facilitate the exchange of information, both during and after the meeting, through personal contact, and also to stimulate ideas for new approaches to the general problem of armor.

The great interest in the meeting was demonstrated by an unexpectedly high attendance (52) and by the vigorous question-and-answer period after each paper. The panel discussion developed into a stimulating session which, despite its length, was apparently considered not long enough.

Through this meeting, Natick Laboratories reviewed its armor programs and received ideas and comments from many individuals who are either managing or conducting armor materials research and development.

Future meetings of this kind will be held at appropriate intervals.

These proceedings are presented in two parts: Part I is unclassified, Part II is CONFIDENTIAL. This division avoids the large bulk of a single volume and makes the unclassified material more easily accessible.

S. J. KENNEDY
Director
Clothing & Organic Materials Division

Approved:

DALE H. SIELING, Ph. D.
Scientific Director

W. W. VAUGHAN
Brigadier General, USA
Commanding

CONTENTS

Meeting of Armor Materials Research Contractors

19 - 20 May 1964

Agenda

19 May 1964

0930	Welcome	Dr. G. R. Thomas
0945	Introduction by Chairman	Mr. A. L. Alesi

Penetration Mechanics Session

1020	Penetration of Single and Laminar Metal Plates	Mr. L. E. Fugelso MRD, Gen'l American Transportation Corp.
1130	Low-Velocity Penetration	Dr. Emerson Cannon Mr. Christopher Wylie Utah R&D Co., Inc.
1350	Penetration of Organic Fibre Felts	Mr. R. F. Recht Denver Research Institute

Materials Properties Session

1430	High Speed Impact of Textiles	Mr. Roy C. Laible
1520	Penetration Mechanics Panel Discussion and Question and Answer Session*	Dr. E. T. Cannon Mr. L. E. Fugelso Mr. R. F. Recht

*Questions may be written out on forms provided and submitted to the Chairman

20 May 1964

Materials Properties Session (continued)(Classified)

0900	(U) Cold Drawing & Orientation in Polymers	Dr. R. Andrews, Jr. M.I.T.
0940	(U) Mechanical-Optical Responses of Polymers to Impact	Dr. A. F. Wilde
1030	(U) Evaluation of Ceramics for Personnel Protection	Dr. R. Liebling Carborundum Corp.

Materials Development Session(Classified)

1100	(U) Personnel Armor Fabrics & Felts *	Mr. E. A. Snell
1130	(C) Ausformed Steel for Personnel Armor (U)	Mr. W. Gerberich Philco Corp. Research Laboratories
1200	(C) Glass-Plastic Composites for Transparent Aircraft Armor (U)	Mr. W. McLaughlin Aerojet-General Corp.
1330	(C) Ceramic-Reinforced Plastic Composites for Aircraft Armor (U)	Mr. R. V. Kolarik Goodyear Aerospace Corp.
1430	(C) Ceramics for Armor (U)*	Mr. J. McManus Coors Porcelain Co.
1510-1600	Informal Discussions	
1500-1600	Tour of Laboratories	

(C) CONFIDENTIAL

*not available for publication

Abstract

These proceedings report the technical progress presented at a meeting called by the U. S. Army Natick Laboratories of those of its contractors who are engaged in research on armor penetration and on the development of armor materials. Included also are papers presented by Natick Laboratories research workers in the same fields.

The papers represent the status of contract and in-house work in armor at the time of the meeting.

THEORETICAL STUDIES ON THE MECHANICS OF PENETRATION OF SINGLE AND LAMINATED METALLIC PLATES BY CYLINDRICAL PROJECTILES

by

L. Erik Fugelso
MRD Division
General American Transportation Corporation

CONTENTS

LIST OF FIGURES

LIST OF FIGURES (CONTINUED)

SECTION 1

INTRODUCTION

1.1 Major Problem Areas

An analytic investigation of the impact and penetration of single and laminated isotropic metal plates by a metallic projectile was conducted [3,4]. The major goal of this study was to determine the physical mechanisms of failure of the plate under the impact of a cylindrical projectile.

Projectiles striking a material give rise to momentum and energy transfer from the projectile to the material. The immediate consequences are an imparted kinetic energy to the particles composing the material, and a change in the strain energy and the internal energy. These result in the deformation of the material by penetration of the projectile and the propagation of a shock wave or stress wave. Accompanying the propagated stress wave are various and diverse effects, such as fracture and plastic flow.

The design of light personnel armor is greatly aided by the knowledge of how and when a plate deforms and fractures under stress. Adequate qualitative and quantitative information for prediction of threshold impact velocities for failure, punchout and spall masses and velocities, residual bullet velocities, and energy absorption within the plate are necessary to guide the practical engineer on his quest for improved armor.

The description of the penetration of a plate by a projectile is an intimate mixture of several theoretical descriptions. Several basic physical mechanisms, each of which may be quite complicated and involved,

occur simultaneously or successively in the course of the deformation of the plate.

At the Fourth Hypervelocity Symposium, Hopkins and Kolsky[1] presented a decomposition of impact phenomena based on the predominant mechanism or mode of deformation. Regions for predominantly elastic deformation, plastic deformation, hydrodynamic shock, etc. were estimated on the stress generated at the surface.

The upper bound on the elastic region is the impact velocity corresponding to the static yield stress which is in turn the lower bound for the plastic region. The upper bound on the plastic regime is the velocity at which the decelerating force on the projectile is greater than the yield strength of the projectile. (Figures 1 and 2)

The effects of each mode of deformation persist throughout the entire range of impact velocities. Thus a more detailed study of penetration is warranted.

The major analytical effort was conducted in two phases.

1.1.1 Dynamic Analysis

To determine the plate's failure to ballistic impact, the dynamic problem of the stress wave propagation in the plate had to be solved. After the stresses had been determined, the areas of the plate where failure was likely to occur could be delineated. Specifically the following stress wave propagation problems were solved:

1. The transient stress wave propagation in a plate system under the

$$\sigma = \frac{\rho c v_s}{2}$$ Impact Stress

$$v_1 = \frac{\sigma_y}{\rho c}$$ Elastic - Plastic Transition

$$v_2 = \left(\frac{\sigma_y}{\rho}\right)^{\frac{1}{2}}$$ Plastic - Hydrodynamic Transition

Figure 1. Definition of Transition Velocities For Dominant Physical Behavior

	Steel	Duralum	Al	Cu	Pb
v_1	46	65	13	8	2
v_2	360	430	190	130	40

∞

Figure 2. Transition Velocities for Specific Impact (M/Sec)

normal impact of a cylindrical projectile was solved analytically and numerically for:

a. Single layer of an isotropic metal.

b. Double layer of an isotropic metal.

2. An approximate solution for the perforation of the plate was established numerically for long-time shear failure of these plates.

1.1.2 Material Properties

It was found that several properties of material deformation under rapid transient loading were very ill defined. Therefore, a phase of the contractual effort was devoted to material properties at high strain rates. Specifically, the following problem areas were investigated:

1. A theory for macroscopic plastic flow under transient loading conditions was developed using the properties of inter-and intra-crystalline imperfections. These results were correlated with the experimental data available on high strain rates.

2. A theory for fracture of metals under transient loading was developed, utilizing elasticity and the flow theory developed above, and compared with existing data on fracture of metals at high stress levels.

1.2 Conclusions

1.2.1 Progression of the Stress Wave

The physical and mechanical processes that occur in the impact and perforation of a plate are: (Figure 3)

1. A large stress is generated by the impact at the interface between the projectile and plate. This stress is proportional to the acoustic impedance of the plate-projectile combination and the impact velocity.

1. Stress generated at impact

2. Longitudinal and shear wave is propagated into the plate.

3. The waves reflect from the back surface.

4. After several reflections, the normal stress becomes small.

Figure 3. Progression of the Stress Wave

2. Two stress waves are propagated into the plate, a fast dilatational wave and a slower shear wave.

3a. These stress waves reflect and refract at the interfaces between lamellae.

3b. These stress waves reflect off of the back or free surface. Meanwhile, two stress waves are propagating into the projectile and, after traversing the projectile, will reflect from the end and return to the impact interface.

4. After the stress wave has completed the first full traverse of the plate, the normal stress becomes small. The portion of the plate under the bullet is in motion with a normal velocity slightly less than the impact velocity. High radial and tangential stresses are developed in the plate. High shear stresses are generated in the plate near the lip of the projectile.

1.2.2 Modes of Failure of the Plate

In response to the stresses that are generated in the plate system, the plate may fail by several mechanisms. They are: (Figure 4)

1. Spall - the plate may fracture in response to high tensile stresses generated by the reflection of the stresses from the back surface.

2. Cavitation - the plate may fracture behind the first or direct shear wave. A significant amount of plastic flow may accompany this fracture pattern.

3. Petalling - after the passage of the first stress waves, the plate may fracture in response to high radial and circumferential tensile stresses that are developed.

1. Spall

2. Cavitation

3. Petalling

4. Plugging

5. Radial Fracture (Laminates)

Figure 4. Failure Modes

4. Plugging - after the passage of the first stress waves, the plate may fracture in response to the high shear stresses developed in the plate near the lip of the projectile.

5. Radial fracture - the plate may fracture in response to high tensile radial and circumferential stresses generated by reflection at an interior interface (laminates).

1.2.3 Material Parameters and Their Effect on the Various Modes of Failure

1. Spall: The material and geometrical parameters that govern the spall are the thickness-to-bullet-radius ratio and the tensile strength of the plate in the direction of the projectile approach. (Fig. 5) The critical perforation velocity is proportional to the tensile yield strength and proportional to $\left[1 + (\frac{h}{a})^2\right]^{1/2}$ where h is the thickness of the plate and a is the radius of the projectile.

2. Cavitation: The material parameters involved in the cavitation on the front side of the plate are the Brinell hardness of the plate or equivalent by the yield strength, the density of the plate, and the compressive ultimate stress. Increases in any of these reduce the penetration due to cavitation. The geometric factor is the same as the spall failure.

3 and 4. Plugging and Petalling: If the plate does not fail by fracture as the first stress wave passes, then the failure of the plate by plugging and petalling must be considered. Plugging is failure of the plate by shear under the rim of the bullet, whereby a plug of plate material is ejected. Petalling occurs when the plate fails in response to

1. Yield Strength

2. Acoustic Impedence of Projectile-Plate Combination

3. Plate Thickness (H/A)

4. Bullet Length (H/L)

Figure 5. Material Parameters

the tensile membrane stresses that are generated. The critical perforation velocity here is best calculated by the method of Nishiwaki[2]. For this plate the critical perforation is a monotonic function of the tensile yield stress of the plate and the plate thickness-to-bullet-length ratio.

These mechanisms are normally restricted from very thin to moderately thick elastic plates ($\frac{h}{a} < 1$) and become the dominant mechanism of failure for very thin plate and low impact velocities.

5. Radial Fracture in Laminates: The advantages of lamination in armor plates lies in the fact that the incident stress waves in one plate are only partially transmitted to the next plate, and thus the stresses in the second plate are reduced. The remaining momentum,however, must be accounted for and it remains in the first plate as a reflected wave. This stress wave has normal stresses tensile if $\rho_1 c_1 > \rho_2 c_2$ and has compressive normal stresses if $\rho_1 c_1 < \rho_2 c_2$, where ρ_1, ρ_2 are the densities of the upper and lower plate, respectively, and c_1 and c_2 are the longitudinal sonic velocities of the upper and lower plates, respectively. The character of the transverse stresses is reversed outside the bullet lip. Thus the strength of the upper plate or the plate closest to the bullet is one dominating material parameter.

SECTION 2

STRESS WAVE PROPAGATION IN THE PLATE

2.1 Introduction

During the course of this study, the determination of the stresses in the plate due to the impact was accomplished for a number of idealized problems.

2.2 Linear Elastic Wave Propagation

The simplest of all problems, conceptually anyway, was the propagation of a linear elastic stress wave.

The equations of motion are shown in Figure 6 and the linear elastic stress-strain relationship used in the computation are shown in Figure 7.

The boundary condition at the bullet plate interface was chosen to be a uniform vertical stress acting over the contact area. While this is not the exact solution, it is close enough for us to determine the physics involved in the process of deformation.

Formal solutions for the equations of motion were obtained by application of Fourier-Hankel integral transforms. These equations were solved by partially analytical and partially numerical techniques for the following three problems:

1. Elastic Stress Waves in a Half Space: The stress wave propagation in an elastic half space, under the action of a vertical stress applied uniformly over a circular region, was solved. Numerical solutions for the stresses, displacements, and velocities throughout the region were computed.

$$\frac{\partial \sigma_r}{\partial r} + \frac{\partial \tau_{rz}}{\partial z} + \frac{\sigma_r - \sigma_\theta}{} = \rho \frac{\partial^2 u_r}{\partial t^2}$$

$$\frac{\partial \tau_{rz}}{\partial r} + \frac{\partial \sigma_z}{\partial z} + \frac{\tau_{rz}}{r} = \rho \frac{\partial^2 u_z}{\partial t^2}$$

Figure 6. Equations of Motion

$$\sigma_r = (\lambda + 2\mu)\frac{\partial u_r}{\partial r} + \lambda\left(\frac{u_r}{r} + \frac{\partial u_z}{\partial z}\right)$$

$$\sigma_z = (\lambda + 2\mu)\frac{\partial u_z}{\partial z} + \lambda\left(\frac{u_r}{r} + \frac{\partial u_r}{\partial r}\right)$$

$$\sigma_\theta = (\lambda + 2\mu)\frac{u_r}{r} + \lambda\left(\frac{\partial u_r}{\partial r} + \frac{\partial u_z}{\partial z}\right)$$

$$\tau_{rz} = \mu\left(\frac{\partial u_r}{\partial z} + \frac{\partial u_z}{\partial r}\right)$$

λ, μ are Lame's constants

Figure 7. Linear Elastic Stress-Strain Law

Figures 8 and 9 show the progression of the vertical stress into the half space at various times. Figure 10 shows a profile of this vertical stress on the axis of symmetry.

Quantitative features of interest are:

a. The stress jump under the bullet is almost uniform with $\frac{z}{a}$ The magnitude of the jump decays

$$\sigma_z = \sigma_z^o \quad (1 + (\frac{z}{a})^2)^{-1/2}$$

b. This spike decays very rapidly behind the shock front with its optical decay constant being roughly $1/2 \frac{z}{a}$.

c. The static solution is established (to within 5%) after the passage of the shear wave front. The magnitude of the static part here is

$$\sigma_z^s = \sigma_z^o \quad (1 + (\frac{z}{a})^2)^{-1}$$

2. Elastic Stress Waves in Plates: The stresses on the axis of symmetry for an elastic plate in response to suddenly applied uniformly distributed vertical pressure, were calculated. (Fig. 11)

Typical values for the vertical stress for a moderately thick plate ($\frac{h}{a} = 0.8$) are shown in Figures 12 and 13.

It is seen that large compression stresses are generated as the wave travels across the plate. The vertical stress is reflected with a reversed sign at the free surface. The combined stress system becomes tensile a little way from the back or free surface. It is at this point where failure by spall will occur.

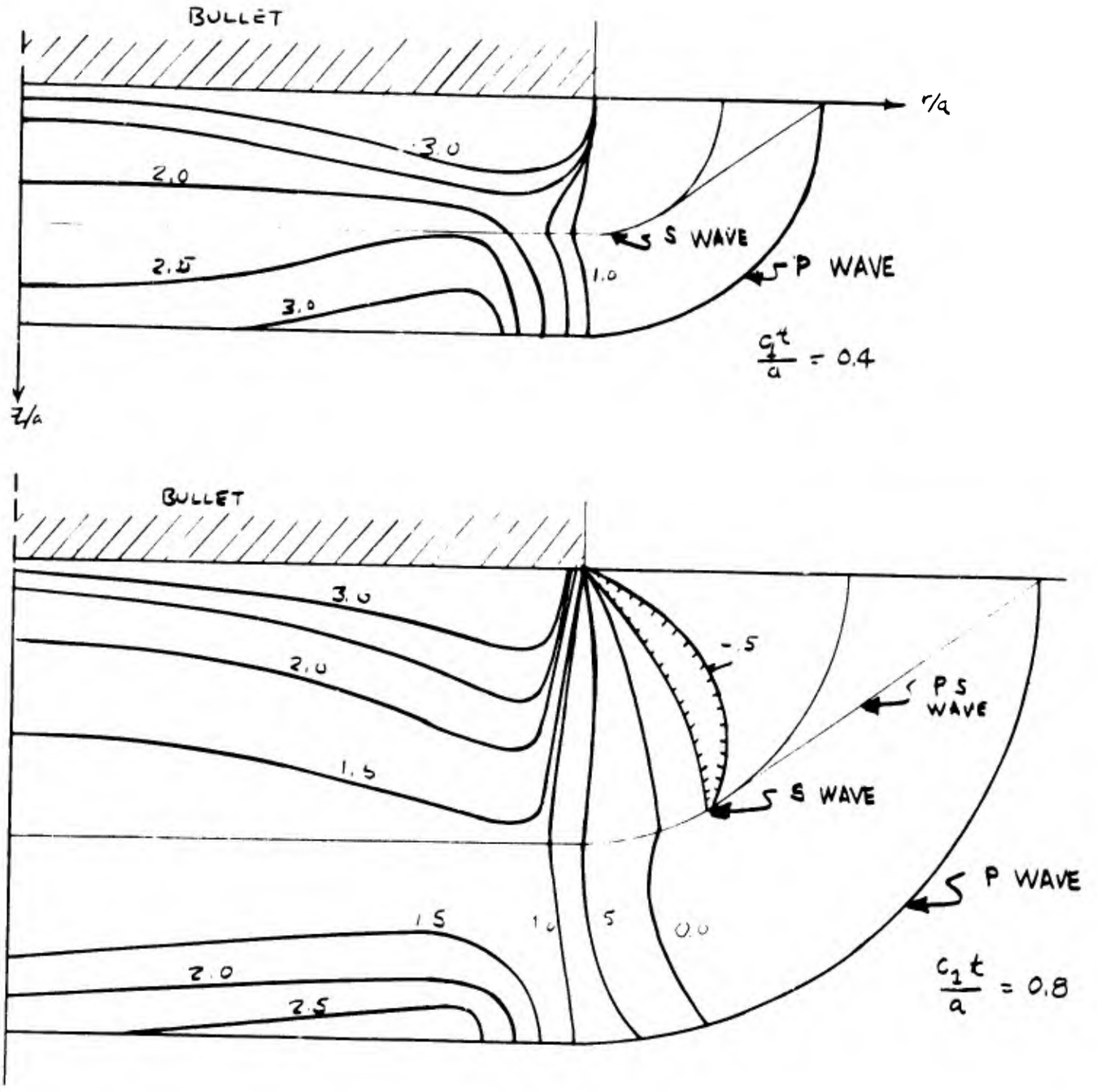

FIGURE 8

CONTOURS OF VERTICAL STRESS ($\pi \sigma_z$) UNDER THE BULLET AT VARIOUS TIMES AFTER IMPACT (POSITIVE SIGN IS COMPRESSIVE)

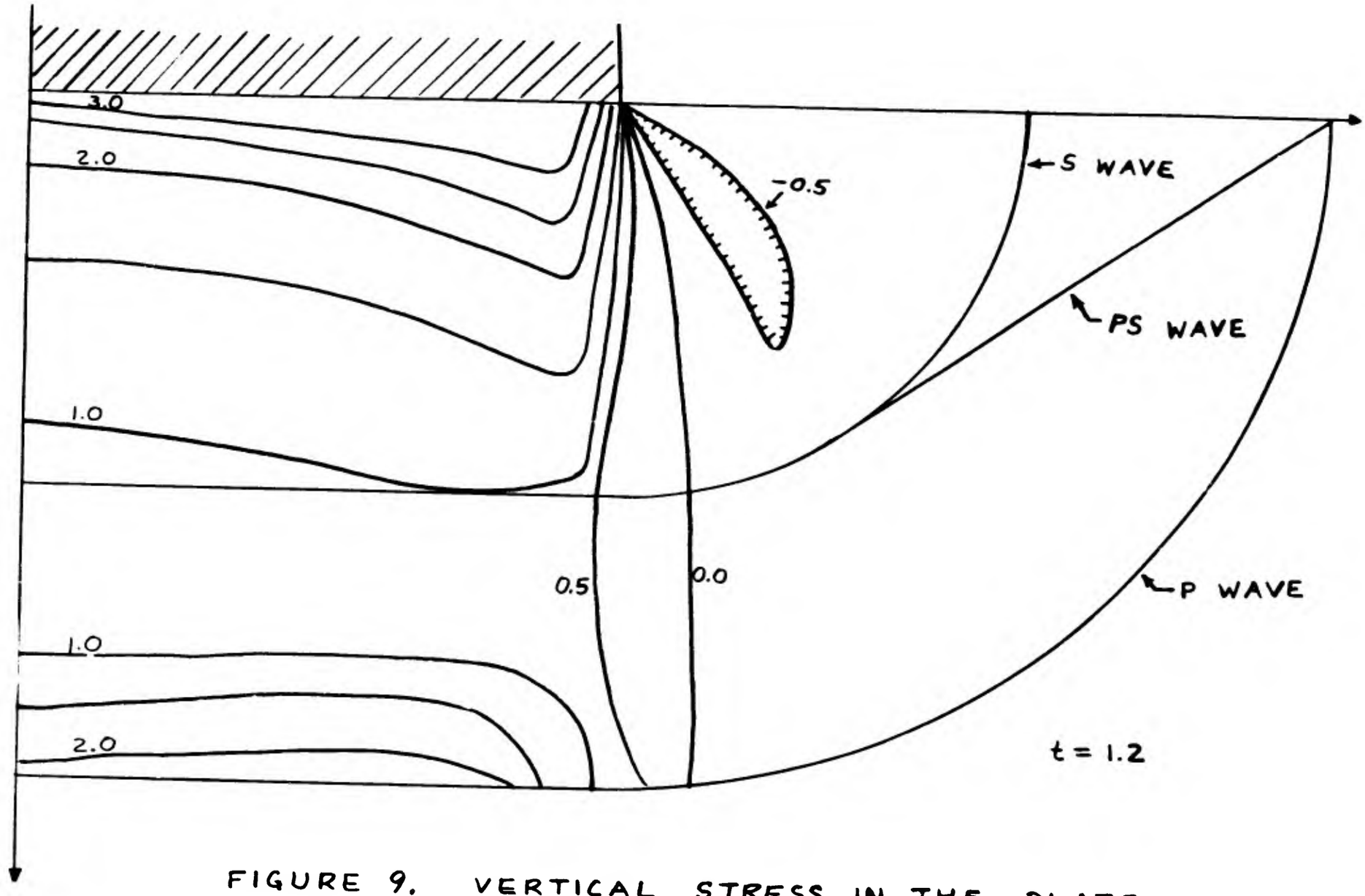

FIGURE 9. VERTICAL STRESS IN THE PLATE

CONTOURS OF $\frac{\sigma_z}{\pi P_0}$

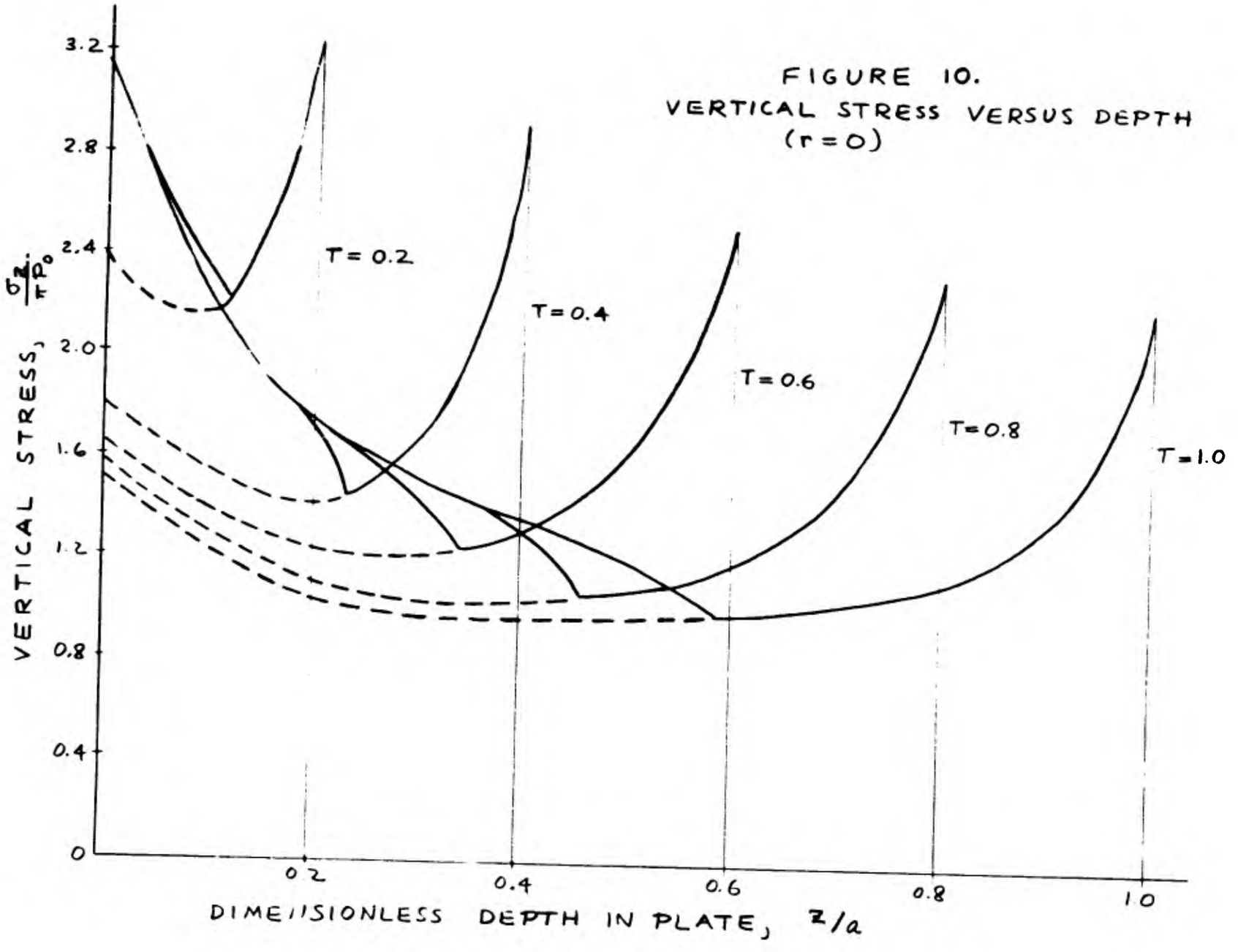

FIGURE 10.
VERTICAL STRESS VERSUS DEPTH
(r = 0)

FIGURE 11.
RADIAL AND VERTICAL STRESS ON THE AXIS OF SYMMETRY

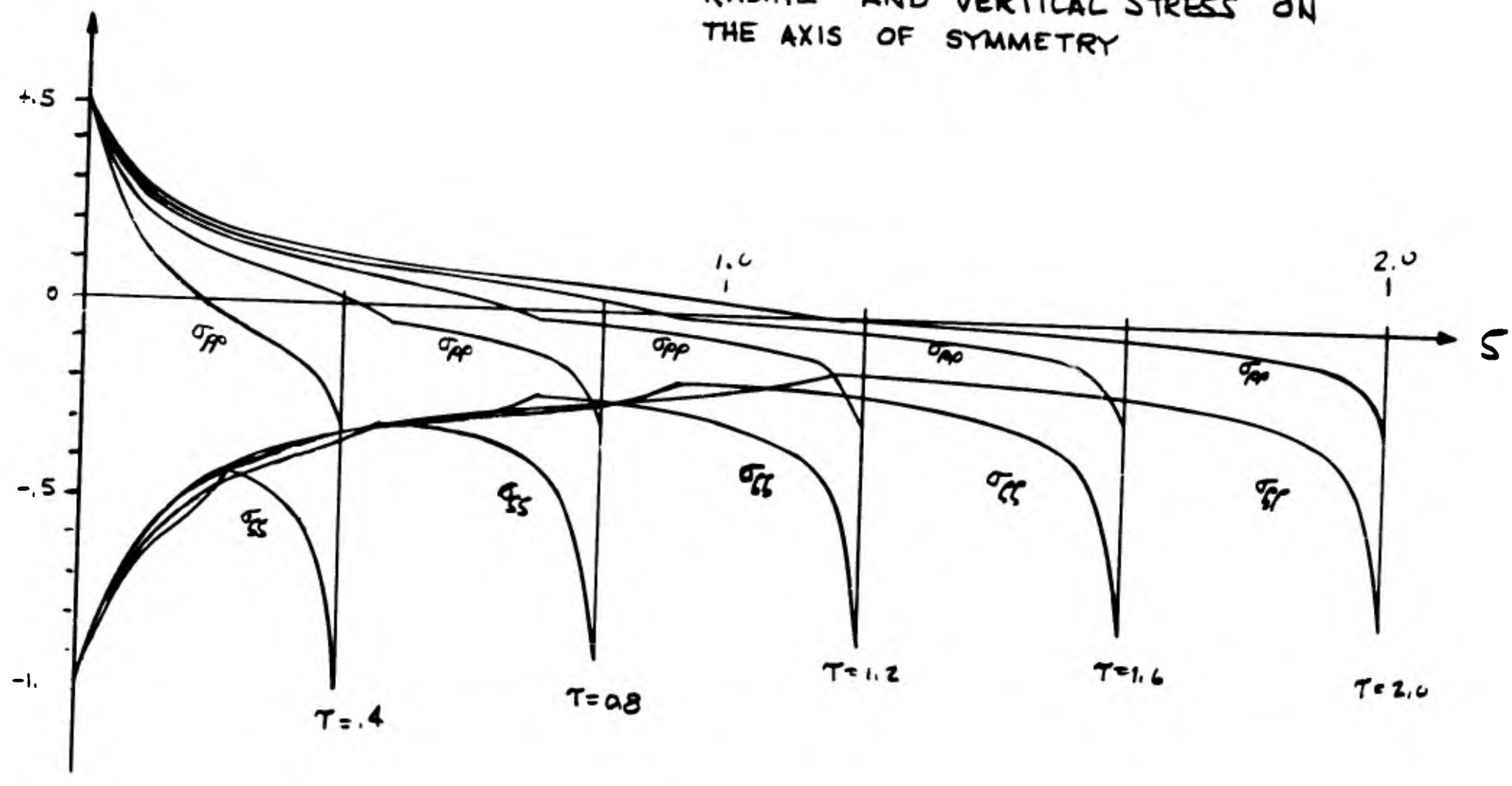

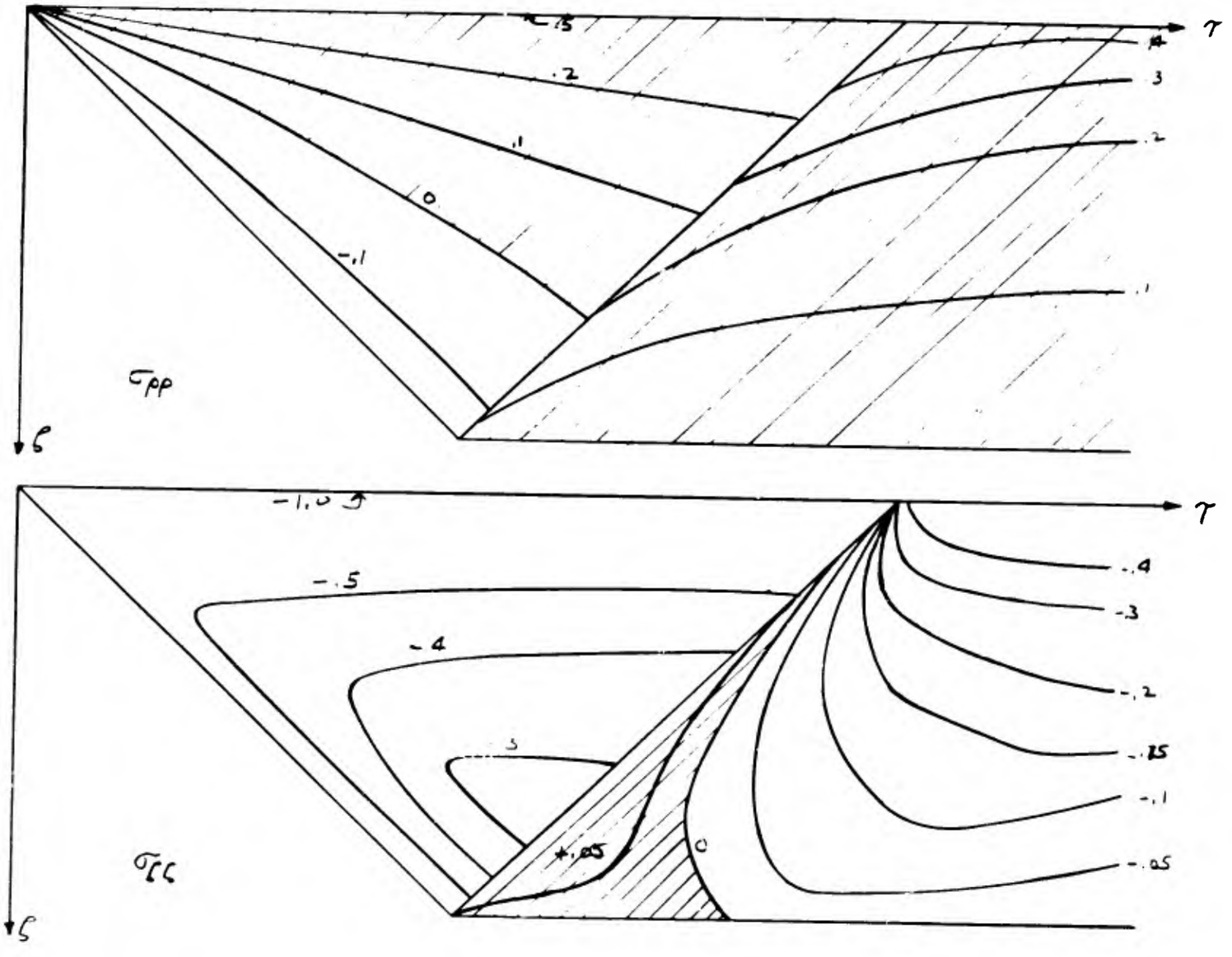

FIGURE 12. STRESS DISTRIBUTION IN Fe PLATE $(\frac{h}{\lambda}) = 0.8$

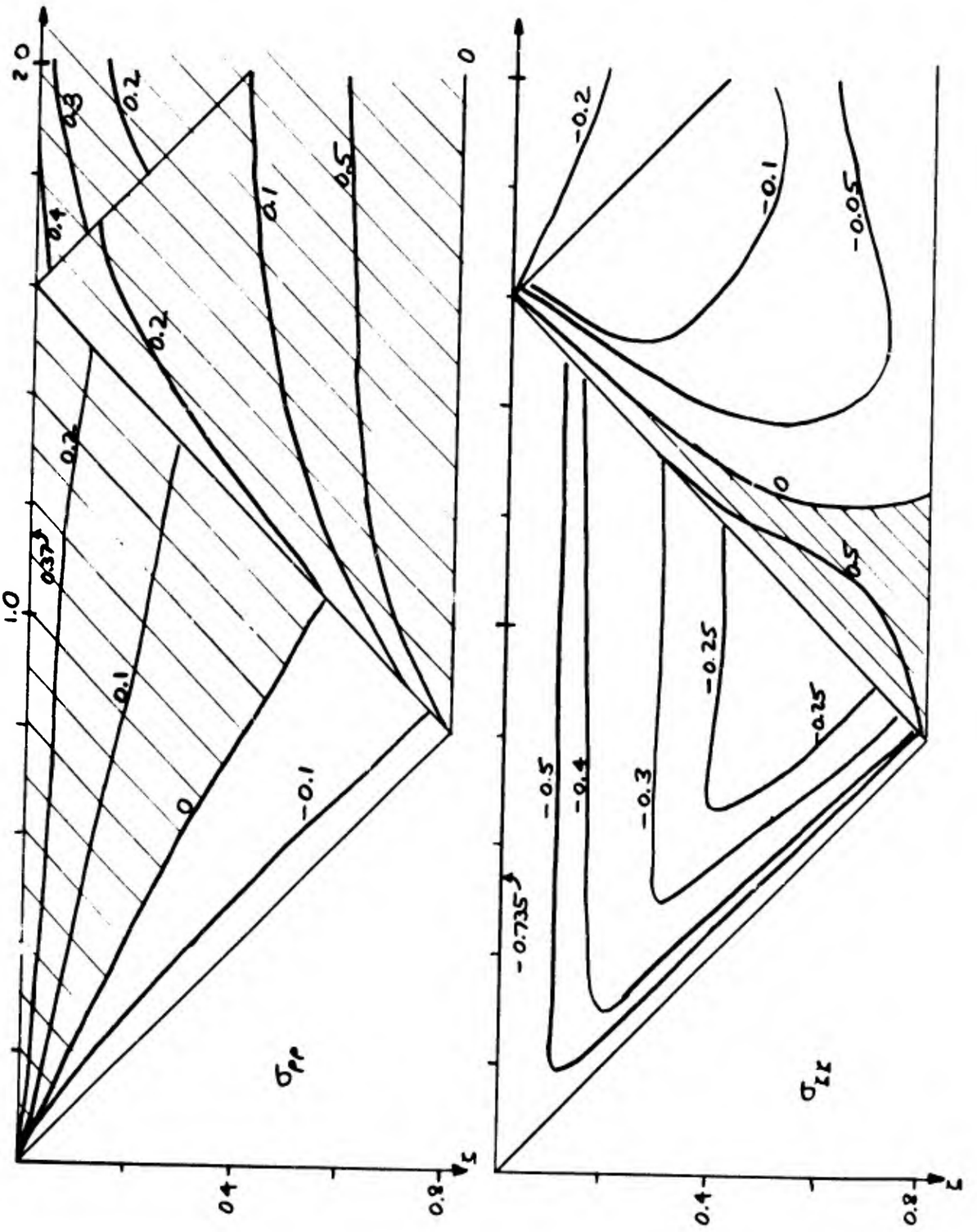

FIGURE 13. STRESS DISTRIBUTION IN Ti PLATE

Failure of the plate material could also occur in the first passage of the stress wave by the fact that the compressive stresses are large.

After the complete passage of the reflected wave has passed, the vertical stress in the plate is quite small.

3. Elastic Stress Waves in Laminated Plates: Using similar boundary conditions, the transient stress on the axis of symmetry was solved during the first two reflections for several interesting combinations of laminated plates.

The vertical and the radial stresses as a function of position and time (all on the axis of symmetry) are plotted in Figures 14 through 19 for the following cases. The two plate materials were steel and titanium. The total thickness in each case is the same ($\frac{h}{a} = 0.8$). The ratios of the thicknesses of the materials vary from 3:1 to 2:2 to 1:3. The titanium plate is first exposed as the upper surface (toward the bullet) and then the order is reversed.

The stress at the interface between plate and projectile will become reduced and the magnitude of the next reflected wave will be smaller.

During the time of the traverse of the first two waves, a force has been acting on the bullet. The net force is the impact stress times the area and it acts for a period equal to twice the transit time of a seismic wave. The bullet will be decelerated during the passage of the direct wave. (Figure 20)

It can be seen that for large bullets (small $\frac{h}{l}$) this reduction in velocity will not be large.

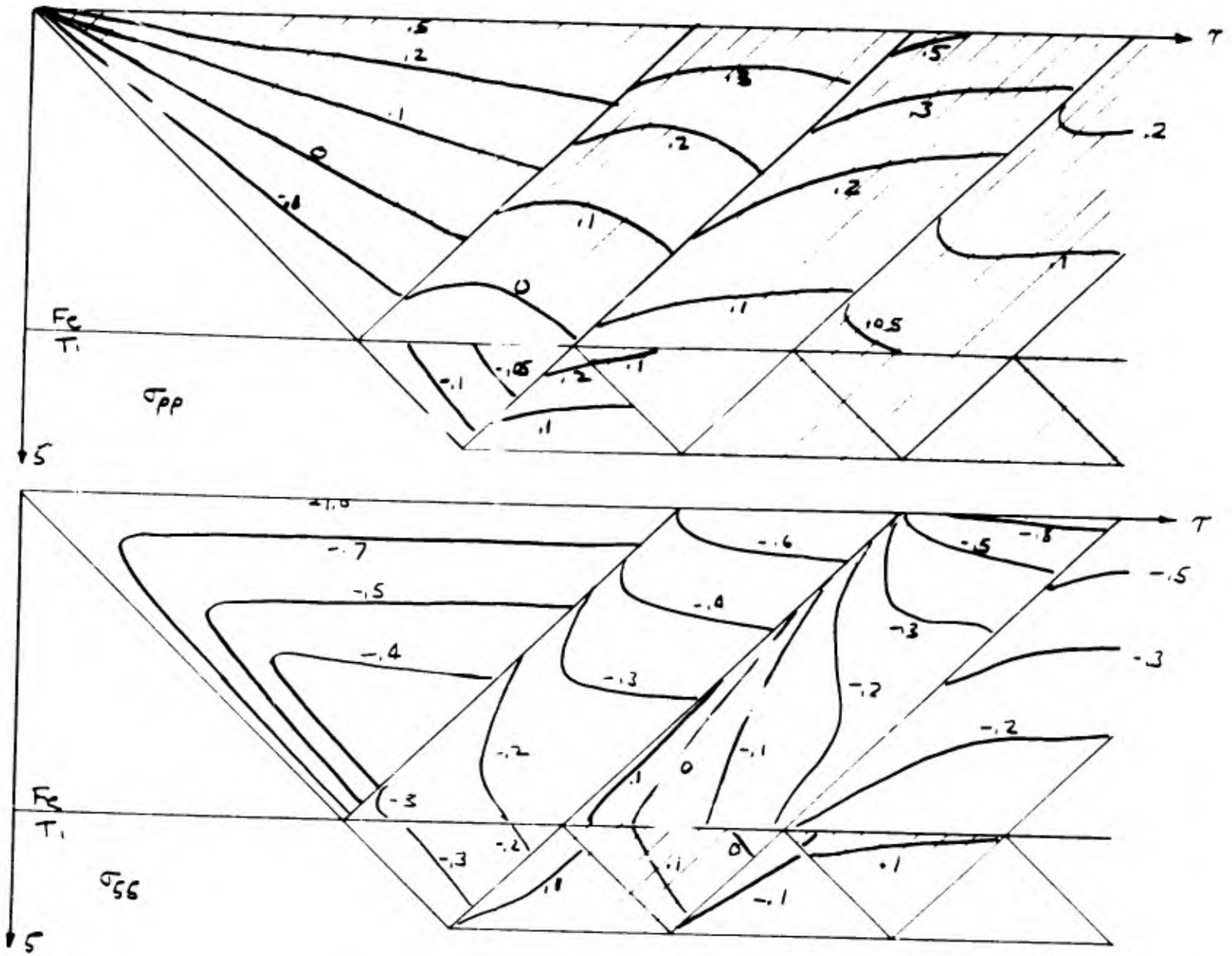

FIGURE 14. STRESSES IN A LAMINATED PLATE
{ .6 F_c ; .2 T_i }

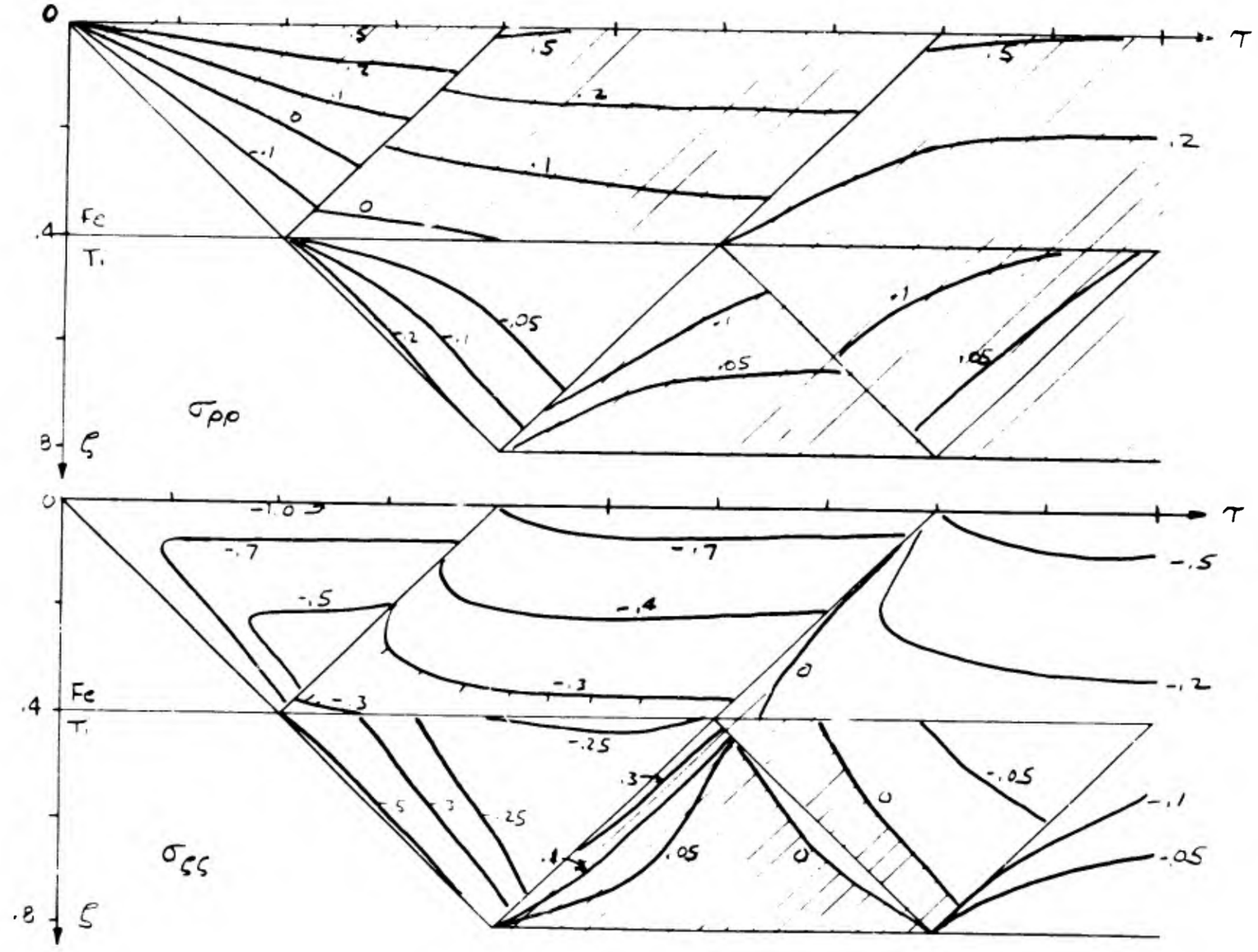

FIGURE 15. STRESSES IN A LAMINATED PLATE
{ 0.4 Fe ; 0.4 Ti }

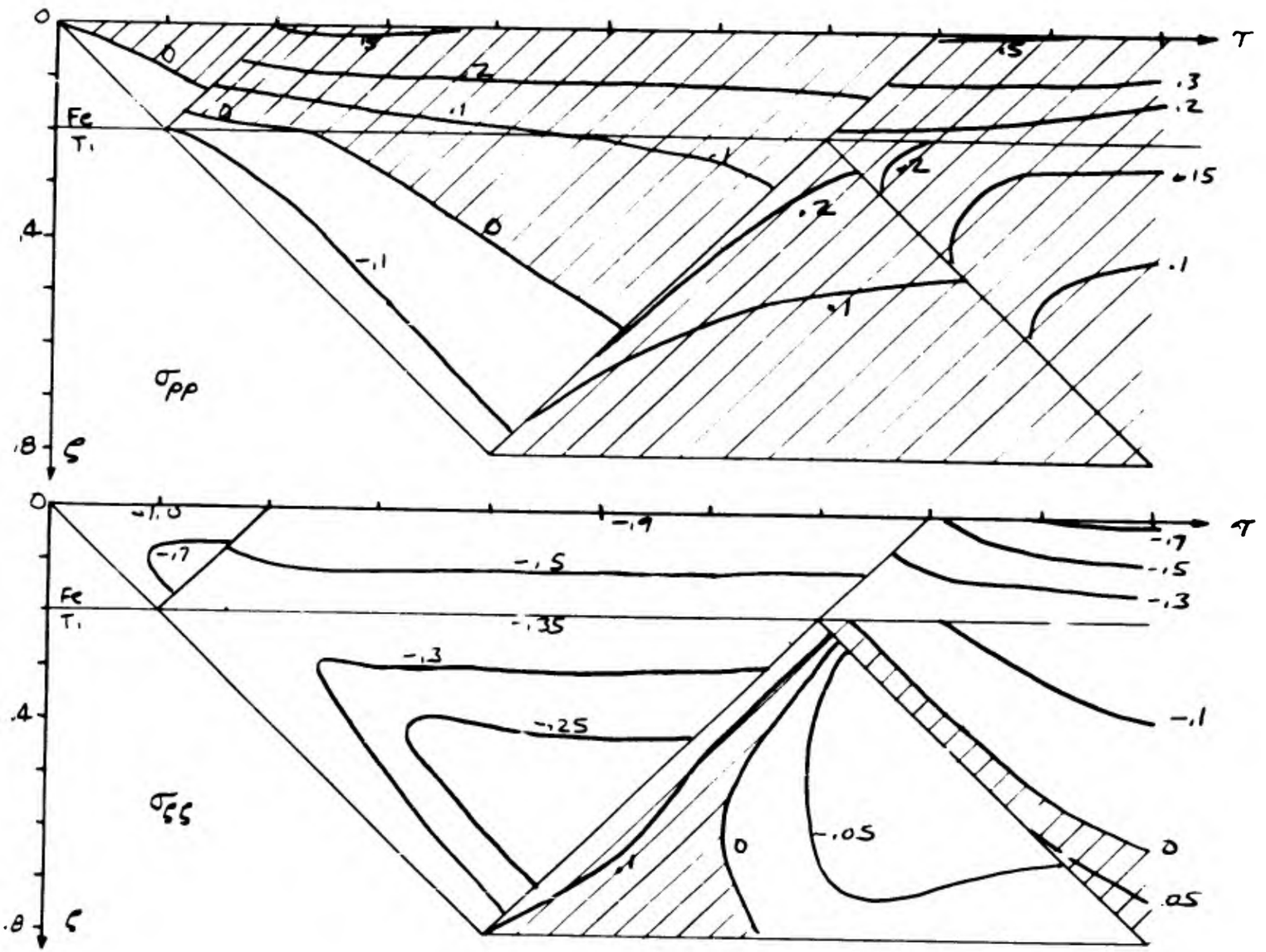

FIGURE 16. STRESSES IN A LAMINATED PLATE
{ 0.2 Fe ; 0.6 Ti }

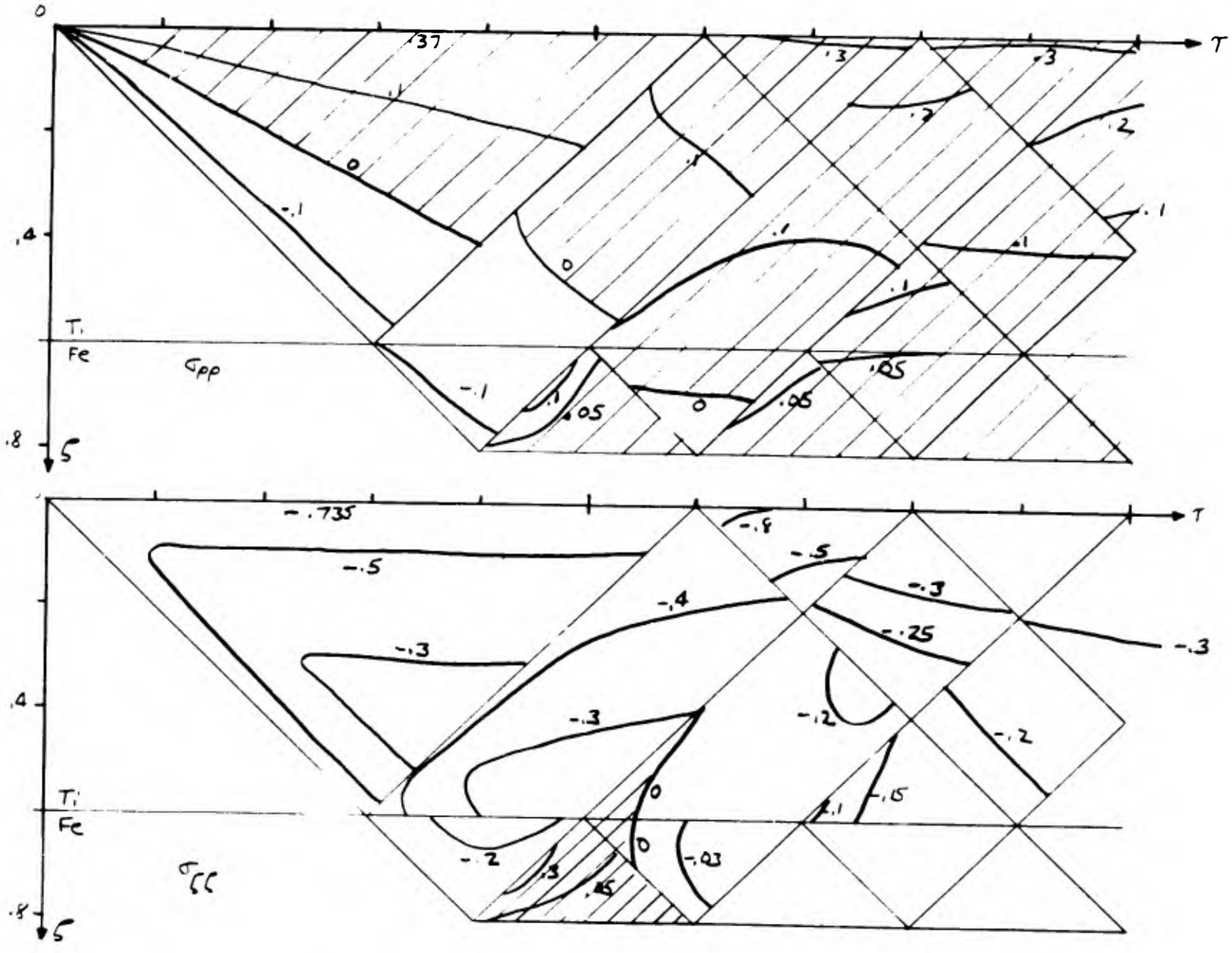

FIGURE 17. STRESSES IN LAMINATED PLATE
{ 0.6 Ti ; 0.2 Fe

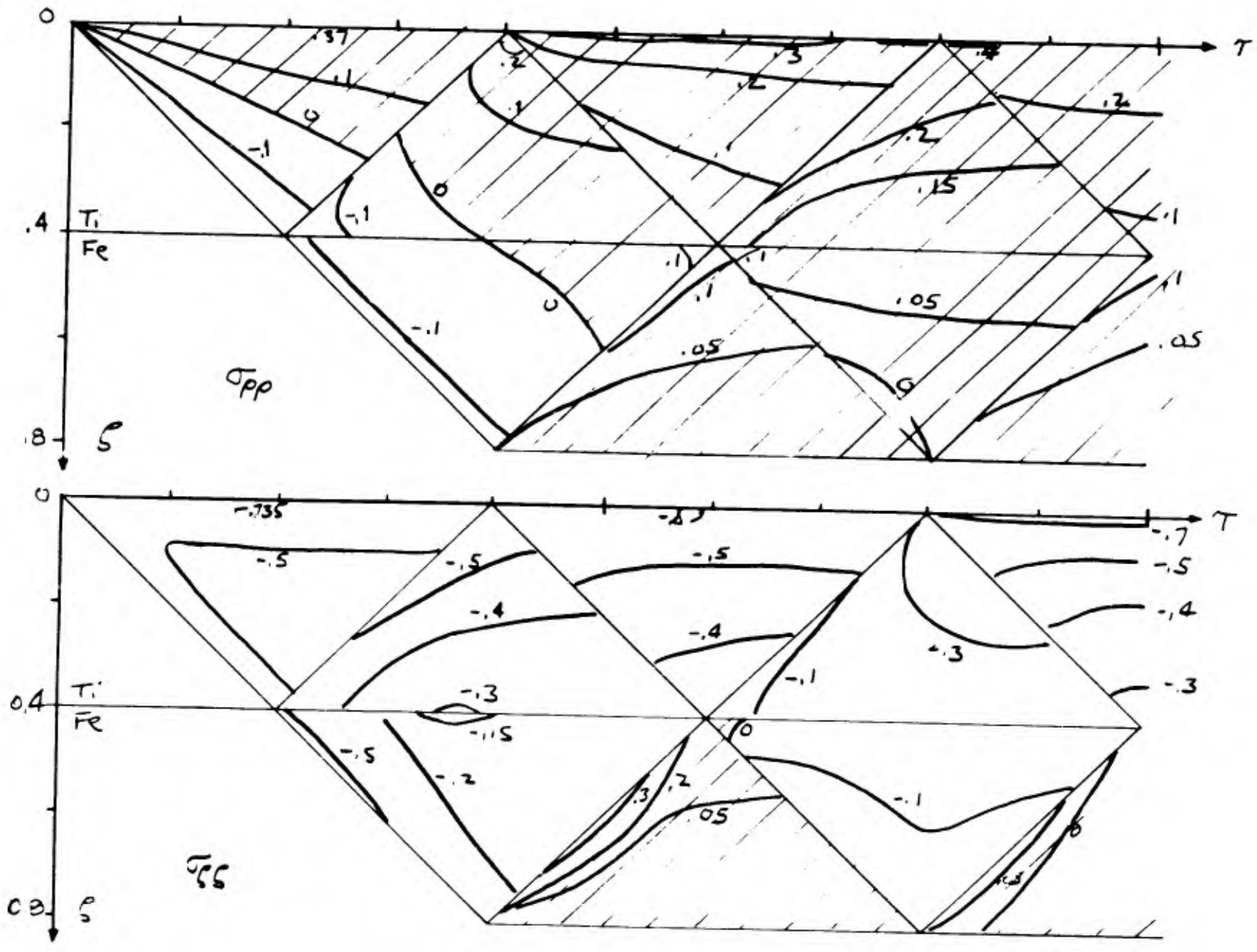

FIGURE 18. STRESSES IN A LAMINATED PLATE {0.4 Ti ; 0.4 Fe}

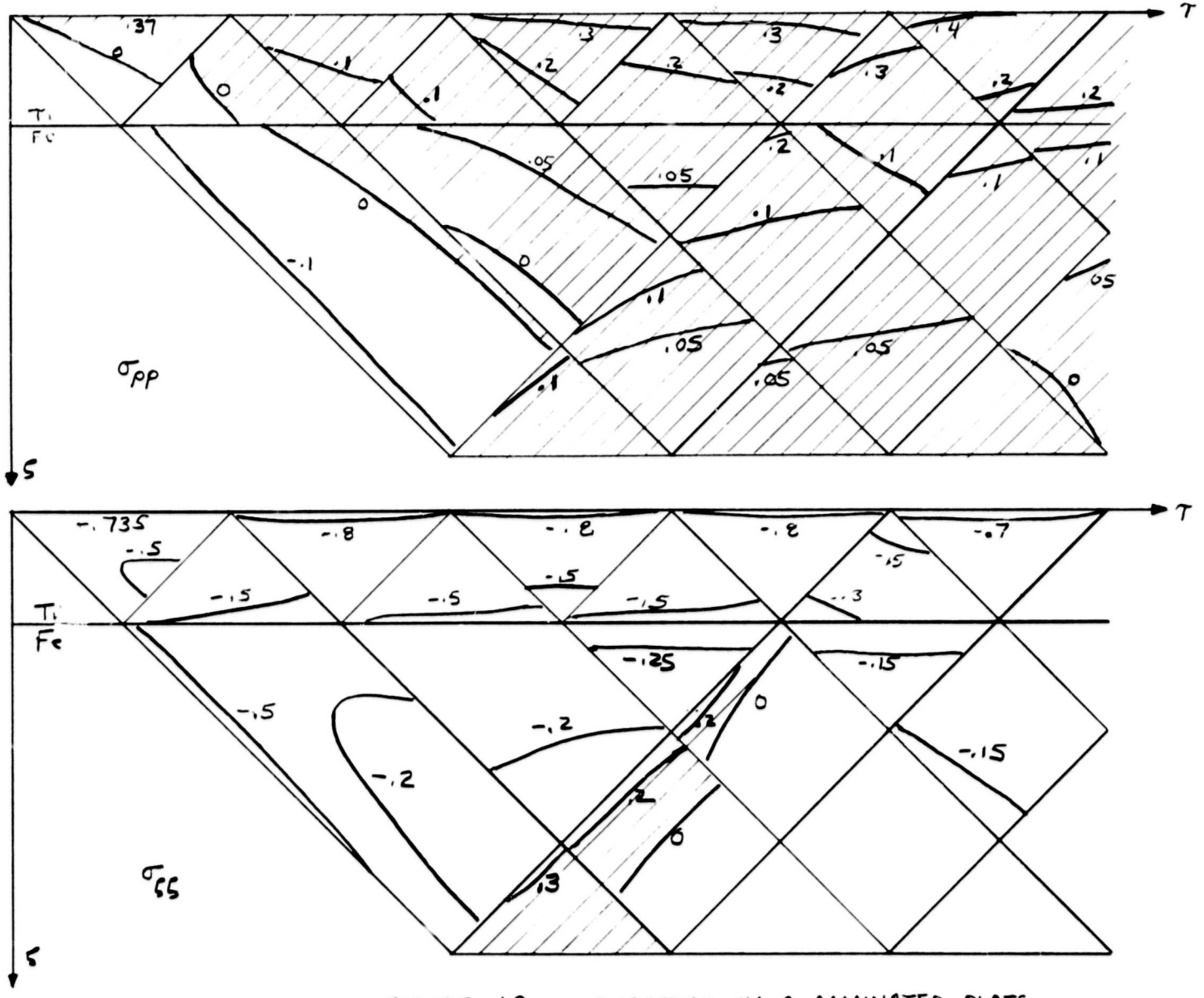

FIGURE 19. STRESSES IN A LAMINATED PLATE
{.2 Ti : .6 Fe}

$$V_f = V_s \left(1 - \frac{2\,\rho_1\,C_o}{\rho_1 C_1 + \rho_o C_o}\,\frac{h}{L}\right)$$

V_f = Final velocity

V_s = Striking velocity

$\rho_1 \rho_o$ = Densities of plate and bullet, respectively

$C_1 C_o$ = Sonic velocities of plate and bullet, respectively

h = Thickness of plate

L = Length of bullet

Figure 20. Average Reduction of Bullet Velocity During First Transit of Stress Wave

2.3 Inelastic Wave Propagation

The second problem in the dynamic stress wave propagation is that of the determination of the inelastic wave propagation. By inelastic wave propagation we mean propagation of stress whose magnitude is above that of the static yield stress. At the Fourth Hypervelocity Symposium, Hopkins and Kolsky[1] gave a breakdown of impact phenomena as a basic mechanism of deformation. The stress that is generated at the impact is proportional to the velocity of impact. For velocities larger than some transition velocity, the dominant stress in the plate in that impact process is in the plastic range. Hopkins and Kolsky computed the transition velocity from elastic to plastic behavior for aluminum-to-aluminum impact and found it to be in the neighborhood of 40 feet per second. The velocities in which we are interested for the ballistic impact studies for the U. S. Army Materiel Command lie above this limit. Therefore, some investigation into stress wave propagation where the stresses exceed the yield stress of the material is indicated.

Several years ago, the author made a study of plastic flow under dynamic and transient loading conditions which far exceeded the yield point. These studies were conducted for the Air Force[4] and for the Defense Atomic Support Agency.[5] Using the continuum theory of microscopic imperfections of intra-crystalline and inter-crystalline nature, a constitutive stress-strain strain-rate equation was developed. This constitutive equation well represented the actual material behavior for face centered and body centered metals. The basic strain-rate equation given by this theory is shown in

Figure 21. The form of this stress-strain strain-rate equation is equivalent to that of a visco-plastic body. The actual coefficients of the body however, are non-linear, as indicated by the theory for dislocation movement. Temperature effects are also included in the development theory.

To demonstrate that the dislocation model and its predictions indeed give reasonable stress-strain curves, we will show the stress-strain curves generated at constant strain rate under various boundary conditions. The stress system will be biaxial. In both problems that will be demonstrated, the longitudinal stress is plotted as a function of the longitudinal strain. The longitudinal strain is applied at constart rate which is indicated on the figure. (Fig. 22) In the first case, we have the deformation which corresponds to the standard tensile test, namely, that the lateral stress is zero and that the body is free to deform laterally. In this case we see that the stress starts off at zero, rises linearly until a yield limit is reached, at which time it bends over and continues almost flat. For other models of microscopic behavior a reduction in the stress reached at this point was obtained. (Fig. 23)

In the second case, we now look at the longitudinal stress vs longitudinal strain for confined case. In this case lateral strain is zero, the lateral stress being sufficient to confine it from lateral motion. In this case the initial stress varies with the strain at its constant strain rate, the modulus being equal to $\lambda + 2\mu$. When the yield conditions are met, the longitudinal stress does not flatten out but now proceeds as a function of the longitudinal strain, increasing at a rate equal to the bulk modulus

$$\frac{\partial \epsilon_{ij}}{\partial t} = \frac{\partial \sigma_{ij}}{\partial t} + \Phi_{ij}\,(\sigma_{ke})$$

Figure 21. Constitutive Equation by the Theory of Dislocation Motion

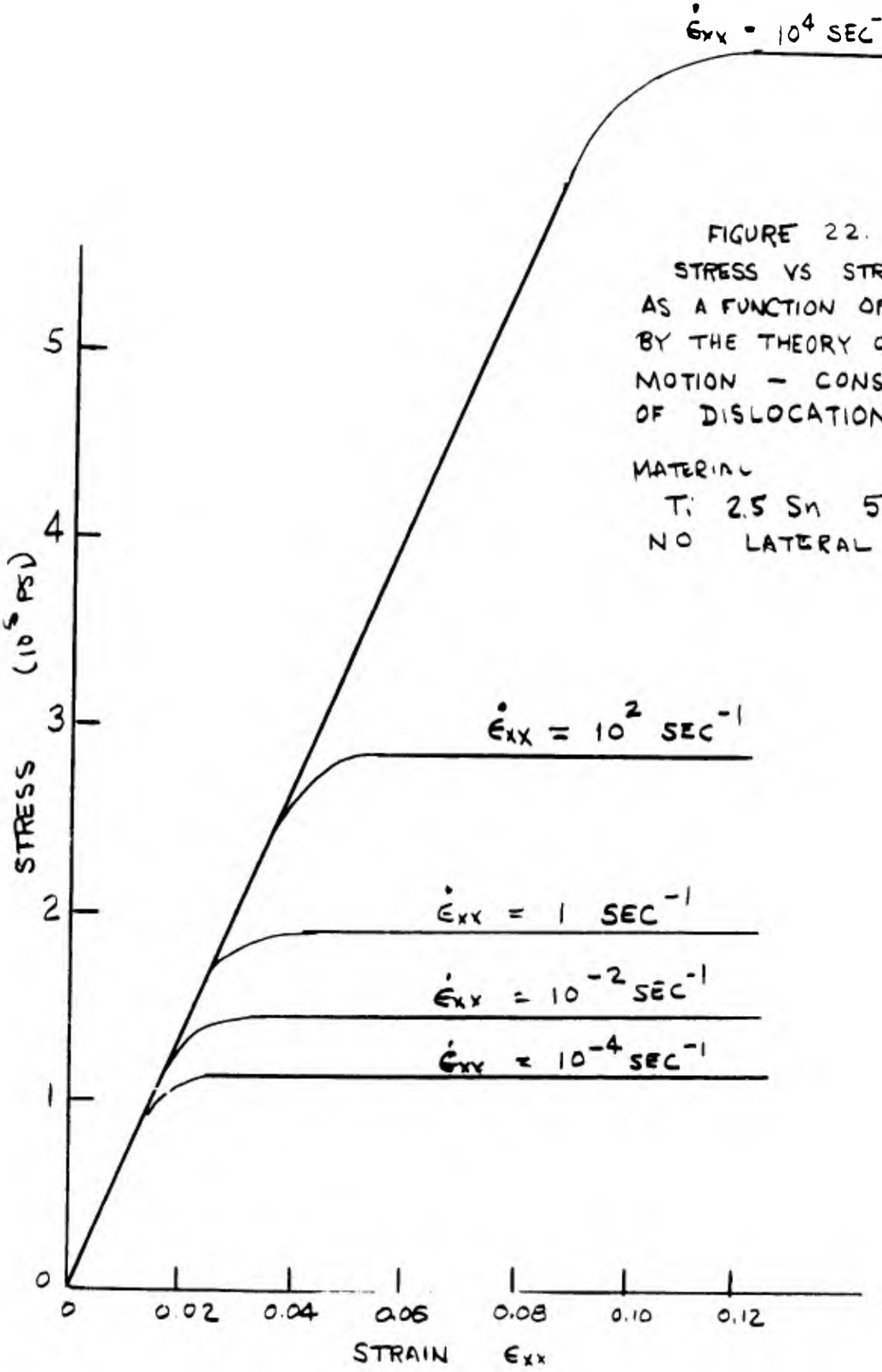

FIGURE 22.
STRESS VS STRAIN
AS A FUNCTION OF STRAIN RATE
BY THE THEORY OF DISLOCATION
MOTION – CONSTANT NUMBER
OF DISLOCATIONS

MATERIAL
Ti 2.5 Sn 5Al
NO LATERAL STRESS

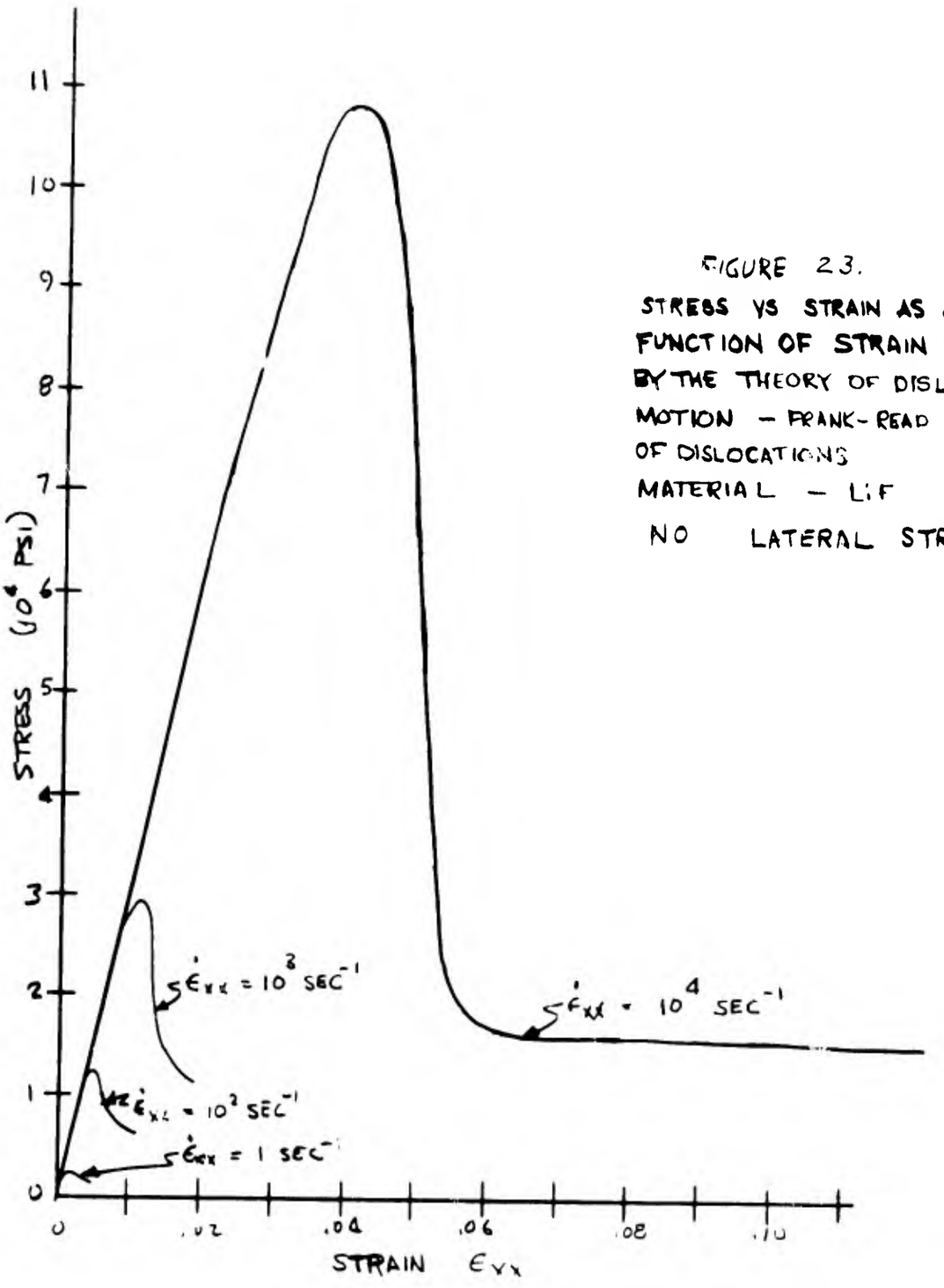

FIGURE 23.
STRESS VS STRAIN AS A FUNCTION OF STRAIN RATE BY THE THEORY OF DISLOCATION MOTION – FRANK-READ REGENERATION OF DISLOCATIONS
MATERIAL – LiF
NO LATERAL STRESS

of the material. The lateral stress increases at the same rate after yielding and has the same sign as the longitudinal stress. (Figure 24)

In these cases, the elastic portion of the deformation is linear. The various dislocation models were chosen to represent experimentally observed dislocation behavior in solids. In Figure 25, they show the behavior of the yield stress (defined as the limiting stress) for the unconfined stress-strain deformation at constant strain rate plotted vs the strain rate. The model here is that of titanium alloy yielding by dislocation movement given by the Frank-Read source. The experimental points are the measured values of Wentz and Catlin.[7] The agreement is fairly good.

In conjunction with the studies of the Defense Atomic Support Agency, the author solved a specific problem which contains one piece of information that is of interest to this particular study. The problem solved was the propagation of a spherical wave into a plastic-deforming medium. The stress applied at the boundary of a spherical cavity was above the yield stress. It was found that the stress at the wave front, which normally decays inversely with the distance from the cavity, decayed at a far greater rate. The bulk of the disturbance propagated out at a slower velocity and a large permanent deformation was found near the cavity itself.

2.4 Application of the Plastic Constitutive Equation to the Ballistic Impact Problem

The full solution of the equations of motion for impact involve the computation of both elastic and inelastic behavior in at least two dimensions in time. The linear elastic solution for the problem is already

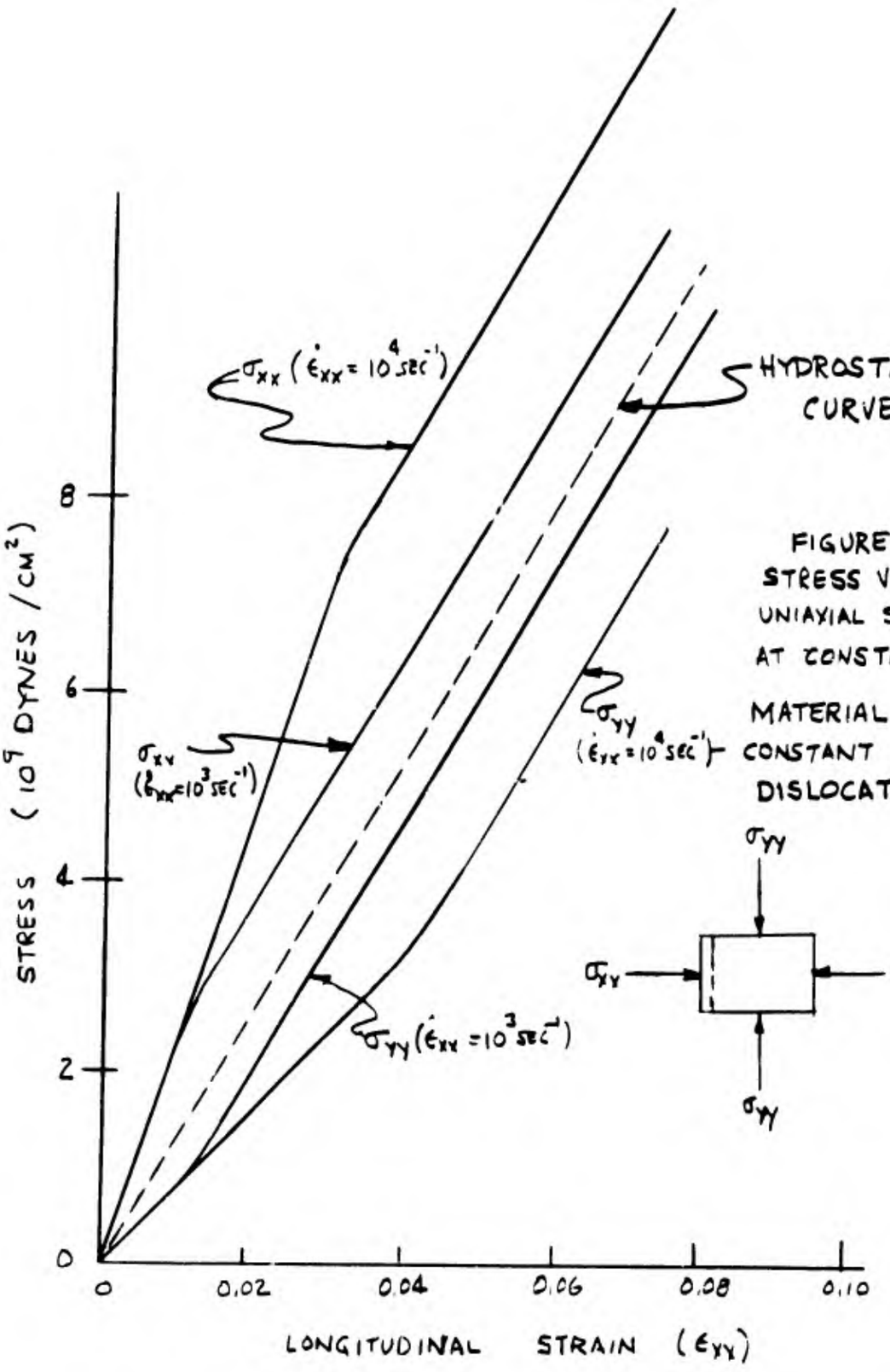

FIGURE 24.
STRESS VS STRAIN
UNIAXIAL STRAIN
AT CONSTANT STRAIN RATE

MATERIAL LiF
CONSTANT NUMBER OF
DISLOCATIONS -

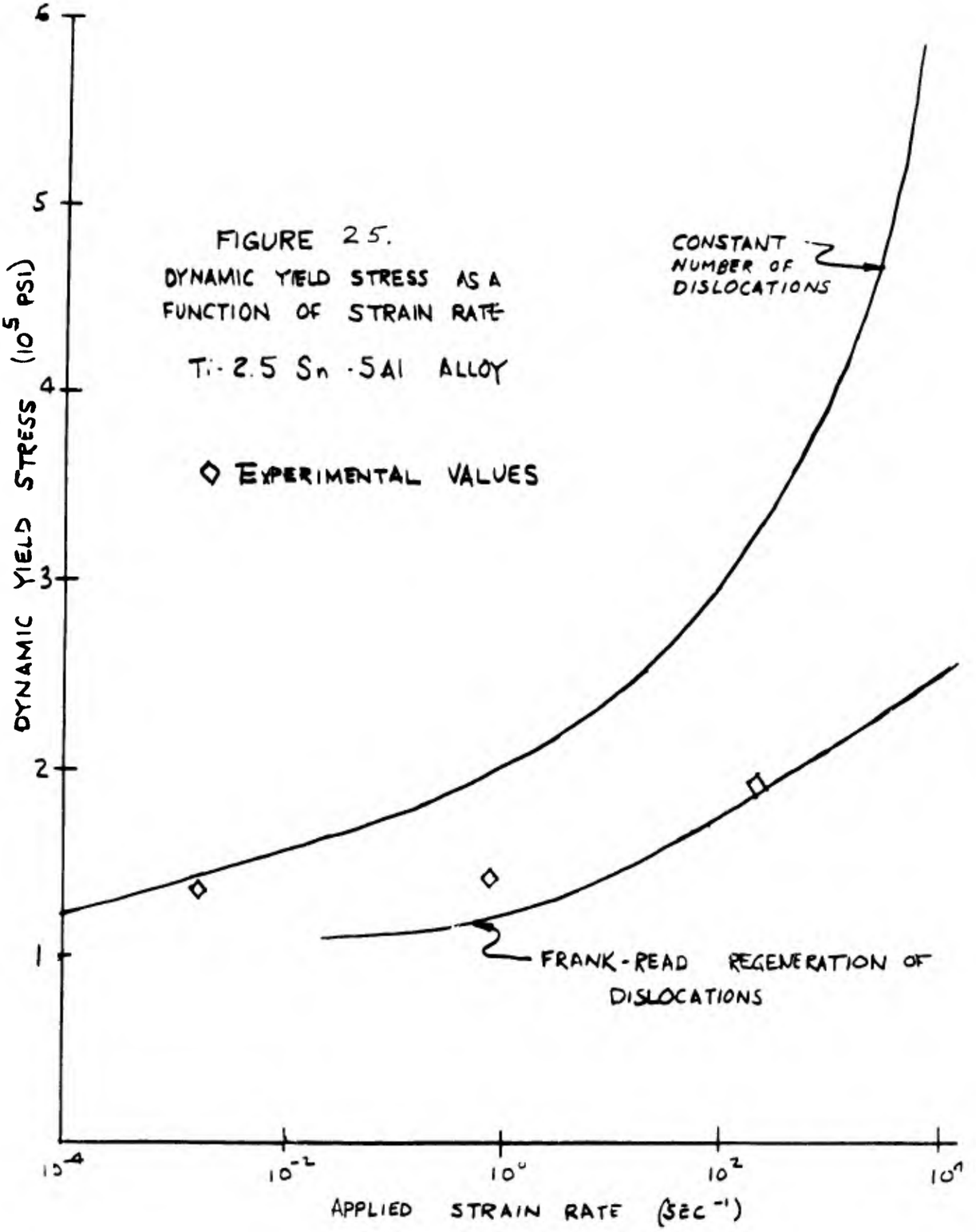
6
5
4
3
2
1
DYNAMIC YIELD STRESS (10^5 PSI)
FIGURE 25.
DYNAMIC YIELD STRESS AS A FUNCTION OF STRAIN RATE
Ti-2.5 Sn -5Al ALLOY
◇ EXPERIMENTAL VALUES
CONSTANT NUMBER OF DISLOCATIONS
FRANK-READ REGENERATION OF DISLOCATIONS
10^{-4}
10^{-2}
10^{0}
10^{2}
10^{4}
APPLIED STRAIN RATE (SEC^{-1})

complicated and yet it is the only model which will allow us to put in an analytic solution in this particular geometry. Since the stresses are above the static yield point for most of the deformation processes involved here, another approach is desired which will demonstrate the effects of the inelastic behavior on the ballistic resistance and on the properties of the perforation and penetration process in general.

Since we are normally dealing with very thin plates, we turn to a thin plate approximation and will reduce the geometrical problem to one less dimension and time-integrate the effects over the thickness. We note that after the stress wave has reflected at least once, the vertical variation of the stresses over the plate thickness is very small.

Proceeding along this line we then develop a mathematical model for a thin plate approximation involving plastic flow. Figure 26 shows the bullet plate configuration. The only variation of the displacement allowed was in the vertical direction, an approximation which is not very far from the truth. The only variation of the displacement, strains, and particle velocities allowed was in the radial direction. No variations in the vertical direction were allowed. We assume also that a circular plug directly underneath the cylindrical bullet is moving at a velocity equal to the bullet at time $t = 0$. This accounts for the first stress wave propagations and the momentum transfer during the first instant of impact. The resulting equations and boundary conditions are shown in Figure 27.

These equations of motion were solved numerically on MRD's IBM 1620 digital computer. A finite difference method for the solution of these

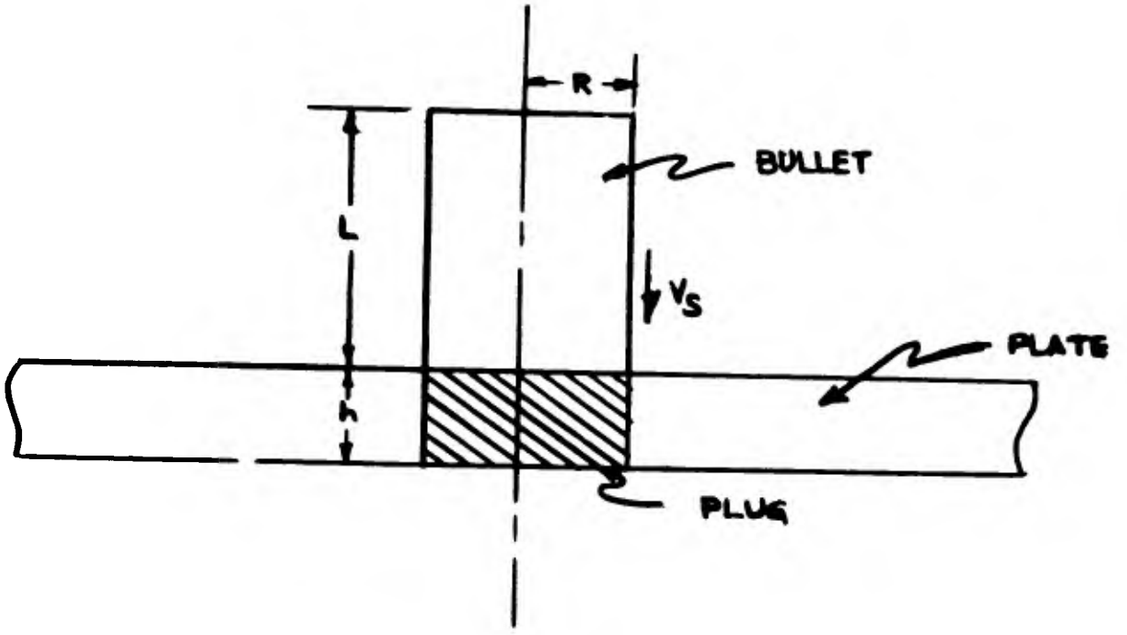

FIGURE 26.
CONFIGURATION OF BULLET AND PLATE
FOR SHEAR MODE CALCULATION

$$\mu \frac{\partial v}{\partial t} = \frac{\partial \tau}{\partial r} + \frac{\tau}{r}$$ Momentum equation

$$\frac{\partial \gamma}{\partial t} = \frac{1}{G} \frac{\partial \tau}{\partial t} + \phi(\tau)$$ Constitutive equation

μ = density of plate

τ = shear stress

γ = shear strain

u = vertical displacement

v = vertical velocity

$\phi(\tau)$ = plastic strain rate component

$\phi(\tau) = A\ e^{-\beta/\tau}$ form chosen to match experimental data

Initial conditions and Boundary conditions

$u = v = 0 \quad t = 0 \quad r \geq R$

$v = v_o \quad t = 0 \quad r \leq R$

$(M + m) \frac{\partial v}{\partial t} = \tau\ 2\pi Rh \quad r = R \quad t \leq 0$

M = mass of bullet

m = mass of plug

R = radius of bullet

h = thickness of plate

Figure 27. Equations for Shear Mode Deformation

partial differential equations was established, checked out and solved. Typical results for the stresses and the velocity as a function of radial position and time are shown in Figures 28 and 29. In this particular case we have chosen an initial velocity such that the initial shear stress is 12 times that of the yield stress. It is noted that the stress at the wave front decays more rapidly than the corresponding linear elastic solution to this problem. This factor is in harmony with the spherical wave solution generated before.

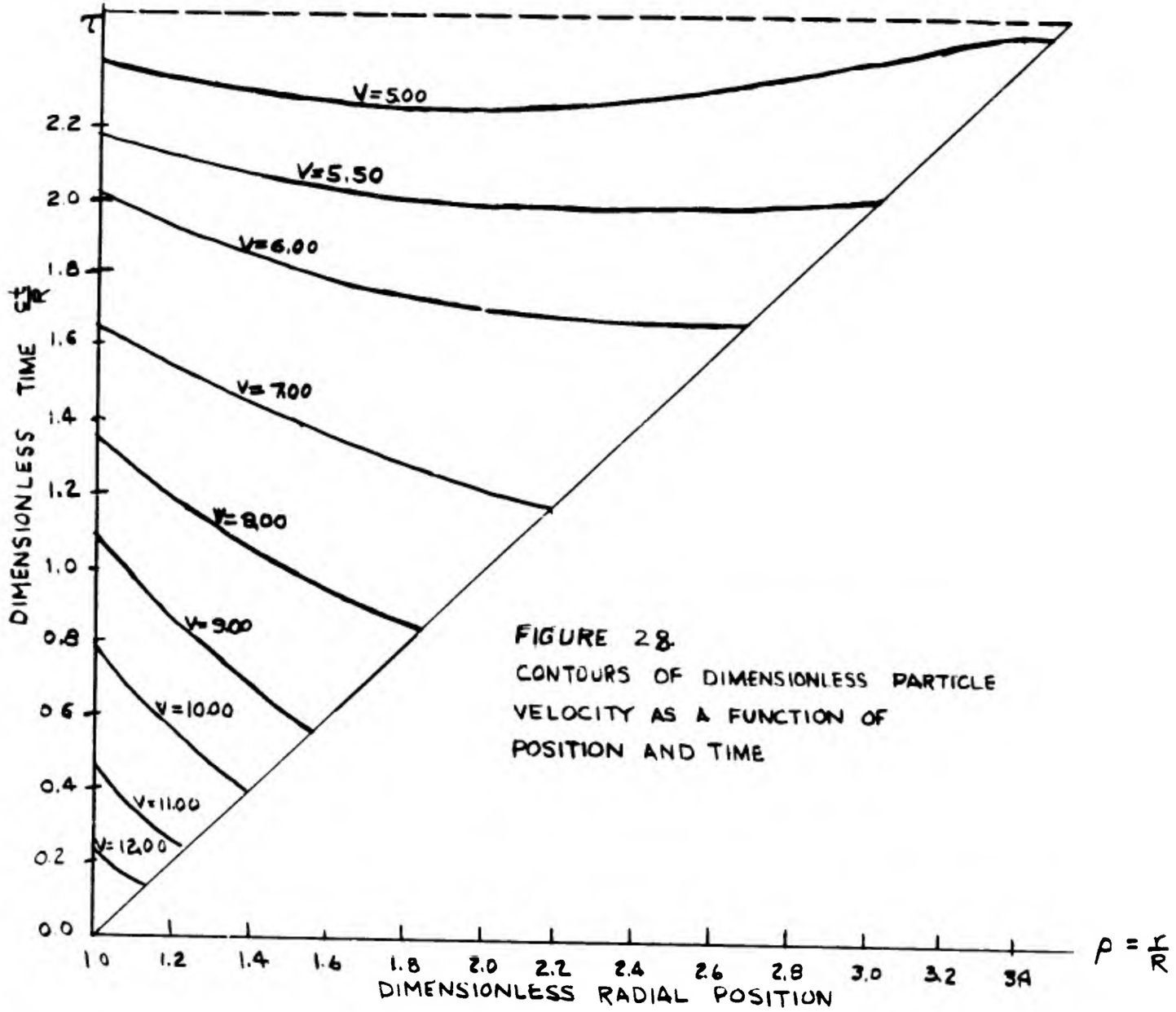

FIGURE 28.
CONTOURS OF DIMENSIONLESS PARTICLE VELOCITY AS A FUNCTION OF POSITION AND TIME

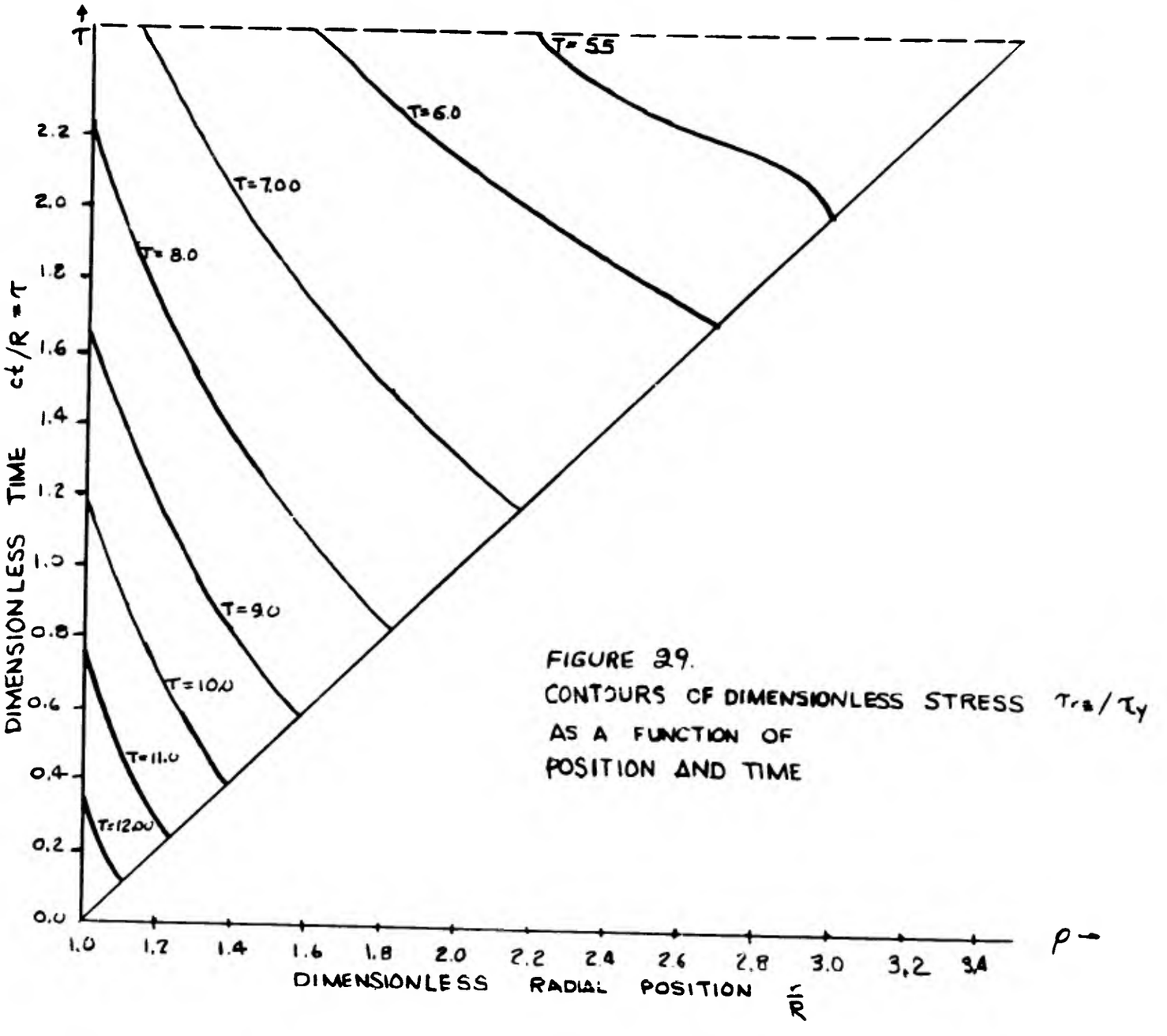

FIGURE 29.
CONTOURS OF DIMENSIONLESS STRESS $\tau_{r\theta}/\tau_y$
AS A FUNCTION OF
POSITION AND TIME

SECTION 3

APPLICATIONS

A large portion of the effort spent by MRD on this contract was in the evaluation of the stresses in the plate as a function of position and time. If the plate is to fail, it must fail in response to the stress. The experimental work of Zhurkov has indicated that, at least for constant stress rate, there is a relationship between the time to fracture and the level of stress.[8] The time to fracture is essentially the inverse of the plastic component of the strain rate corresponding to that stress as determined from the dislocation theory of plastic flow. The actual magnitudes of the time to fracture that were measured by Zhurkov are very, very short (in the order of 10^{-8} seconds) for very high stresses.

For a first approximation, the time to fracture at a stress above the static yield stress of the material is so short that it can be ignored, and the time to fracture below this yield stress is so long that the material will remain unbroken. As an approximation this turns out to be a very good description for the fracture and failure criteria that would follow the first wave across the plate.

Figure 30 shows an experimental time to fracture versus stress level obtained by Zhurkov in his studies on fracture.

In response to the stresses that are generated in the plate system during the impact, the plate may fail by several mechanisms. The mechanisms are:

1. Spall - the plate may fracture in response to high tensile stresses generated by the reflection of the first stress wave from the back surface.

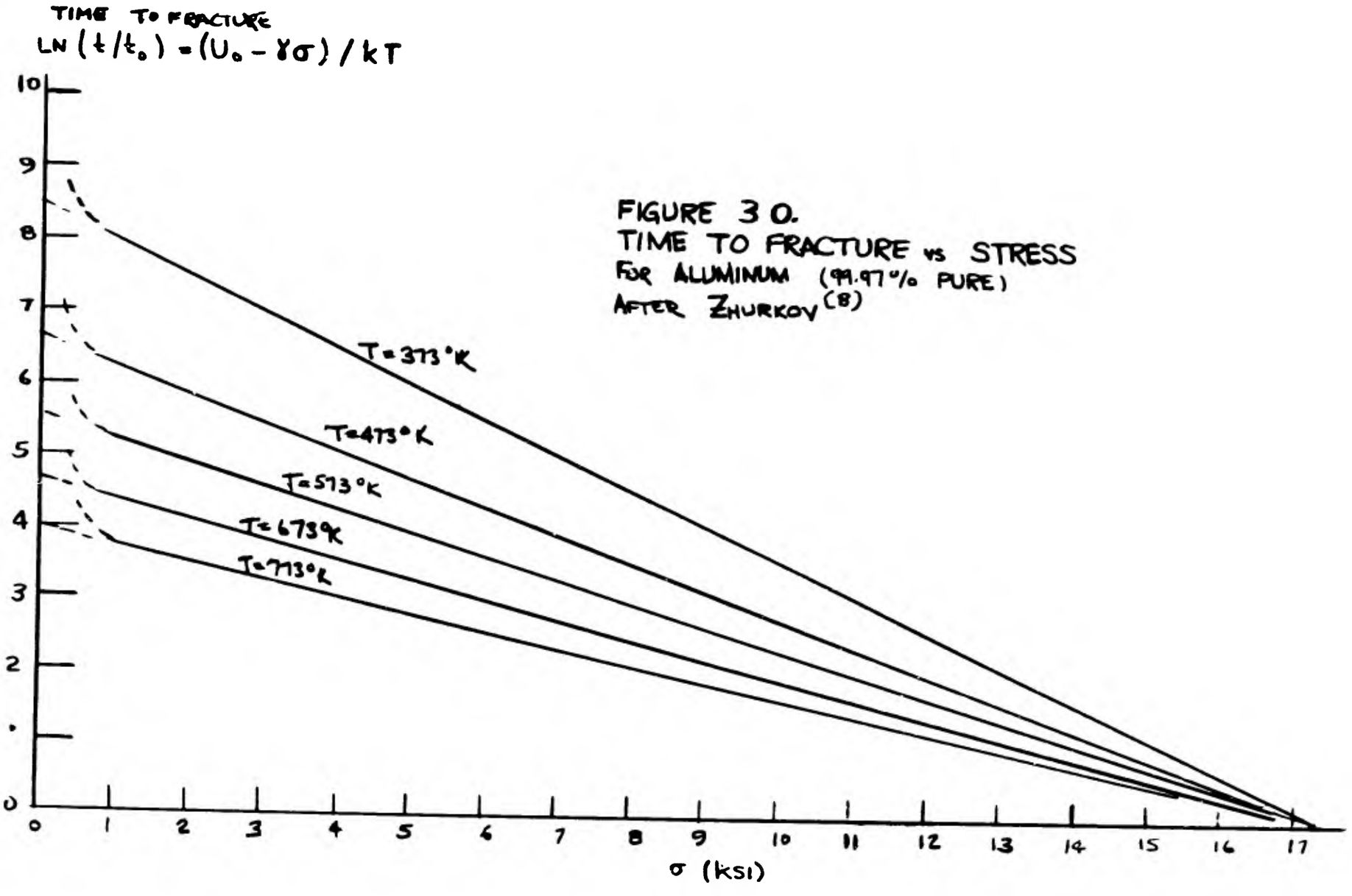

FIGURE 30.
TIME TO FRACTURE vs STRESS
FOR ALUMINUM (99.97% PURE)
AFTER ZHURKOV [8]

2. Cavitation - the plate may fracture behind the first primary wave or the first shear wave that goes across the plate.

3. Petalling - after the passage of the first stress wave, the plate may fracture in response to high radial and circumferential tensile stresses that are developed.

4. Plugging - after the passage of the first stress wave, the plate may fracture in response to the high shear stresses developed in the plate near the projectile.

5. Radial Fracture in Laminates - the plate may fracture in response to tensile radial stresses generated by reflection.

To generate a prediction for ballistic resistance of a plate to penetration, let us examine the method of failure in the direct wave. Then we will examine the delayed mechanism of the failure.

We shall consider the following mechanism as representative of the direct stress wave failure. Let us assume that the plate fails in compression. The stress at the wave front directly underneath the plate in the vertical direction is compressive. The two lateral stresses, namely the radial and the tangential stress on the axis of symmetry, are equal, and both are equal to a given fraction of the vertical stress.

Since the material test for failure in compression has low lateral confining pressure, we will make the following identification between the standard tensile failure test and failure here. We will state that the material failed if the maximum shear stresses developed are equal to the maximum. In this case, the difference between the vertical stress and

either the radial or tangential stress are equal, then, to the compressive yield strength of the material. (Figure 31.)

The vertical stress at the back side of the plate is the lowest value of this compressive stress in the direct wave. The compressive stress there is a function of the following three parameters:

1. impact pressure at the interface between the bullet and the projectile,

2. the geometrical attenuation in the elastic wave propagation across the plate,

3. the attenuation by plastic flow or other inelastic means. The impact pressure is proportional to the acoustic impedence of the plate projectile combination and to the impact velocity.

We may, therefore, compute a velocity such that the lowest stress in the back of the plate is exactly equal to the stress required for fracture. (Figure 32) We thus generate a critical velocity for perforation. This critical velocity is a function of the yield strength of the plate, the plate geometry (given through the ratio of h, the thickness of the plate, to the bullet radius a), and to the plate and projectile material properties such as the elastic constants and density. At zero plate thickness the critical velocity is finite and, at very large plate thicknesses, it approaches a linear increase. The residual bullet velocity versus striking velocity was calculated (Figure 33) and plotted (Figure 34).

This form of the equation for the critical perforation velocity given by the compressive failure of the material provides an upper bound for the

FIGURE 31.
FAILURE IN THE DIRECT STRESS WAVE MOHR'S CIRCLE DIAGRAM

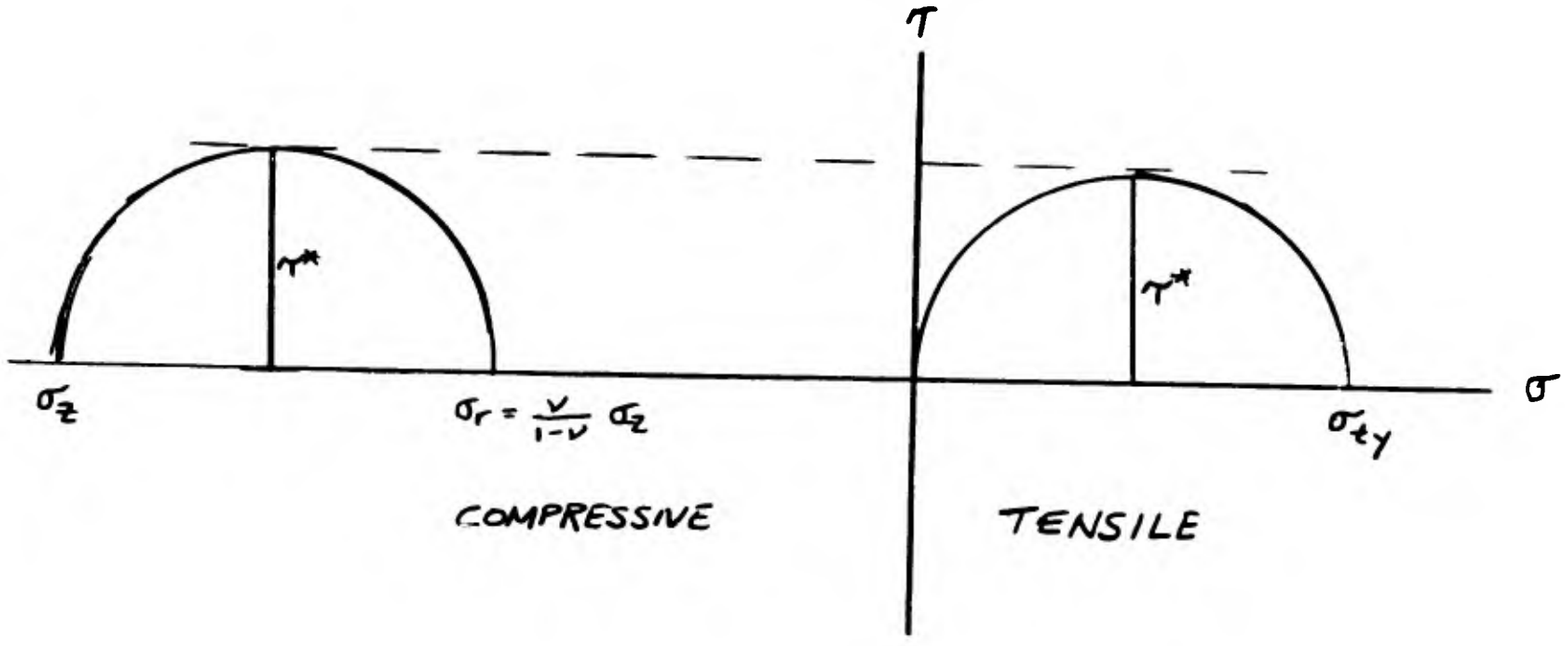

$$\sigma_z(o,h,\frac{h}{c}) = \sigma_z(o,o,o)\, f(\frac{h}{a}) = \frac{1-2\nu}{1-\nu}\ \sigma_{ty}$$

$$f(\frac{h}{a}) = (1 + (\frac{h}{a})^2)^{-\frac{1}{2}}$$

$$\sigma_z(o,o,o) = \frac{\rho_1 C_1\ \rho_2 C_2}{\rho_1 C_1 + \rho_2 C_2}\ V_s$$

$$\therefore \quad V_s = (\frac{1-\nu}{1-2\nu})\ \sigma_{ty}\ (\frac{\rho_1 C_1 + \rho_2 C_2}{\rho_1 C_1\ \rho_2 C_2}) \setminus (1 + (\frac{h}{a})^2)^{\frac{1}{2}}$$

Figure 32. Failure of Plate in Direct Wave, Critical Velocity

$$V_r = 0 \qquad V_s \leq V_{sc}$$

$$\frac{V_r}{V_s} = 1 - \frac{h}{L} \frac{\rho_2 C_1}{\rho_1 C_1 + \rho_2 C_2} \qquad V_s \geq V_{sc}$$

Figure 33. Residual Velocity for Direct Failure

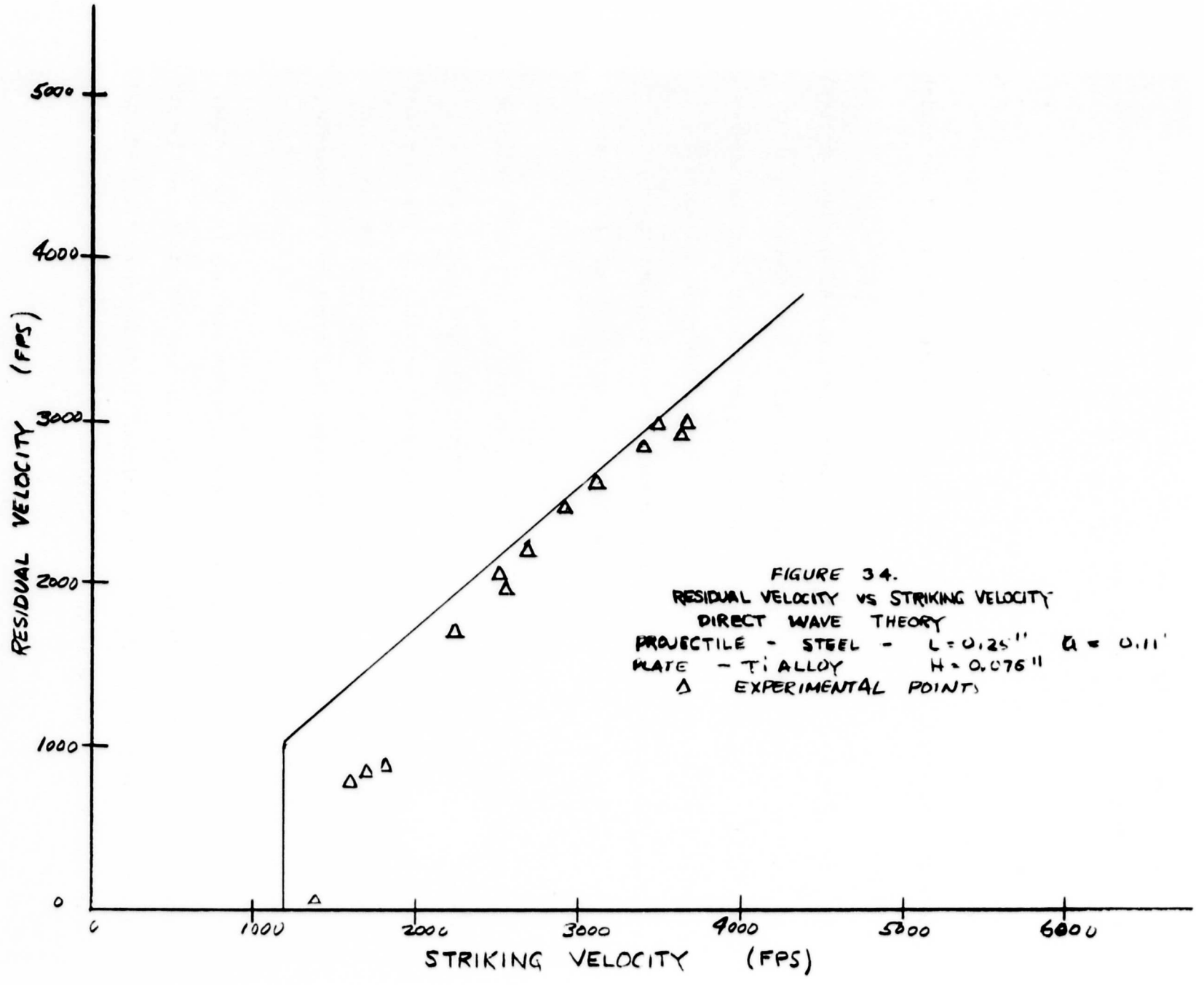

FIGURE 34.
RESIDUAL VELOCITY vs STRIKING VELOCITY
DIRECT WAVE THEORY
PROJECTILE - STEEL - L = 0.25" Ø = 0.11"
PLATE - Ti ALLOY H = 0.076"
Δ EXPERIMENTAL POINTS

failure of the plate by spall if we drop the terms containing Poisson's ratio. This expression tends to come very close to the exact solution for thicker plates.

The material and geometric parameters that govern the failure in both cavitation and spall mechanisms of failure of the plate are the thickness-to-radius ratio and the strength of the plate and the velocity of the bullet stress.

If, after the passage of the first wave, the plate has failed, we have obtained an answer. If the plate has not failed by this time, the bullet may still be coming on with a high velocity, particularly in those cases where the bullet length is very much longer than the plate thickness. In this case we now turn to the second mode of wave propagation, namely the inelastic wave propagation as given by the shear mode of failure as demonstrated above.

The failure of the plate occurs either in tension or in shear outside or very near the radius of the bullet. If the fracture conditions are assumed to happen instantly after the required conditions for fracture have been reached, we will then have the criteria for perforation velocity and the residual velocity-striking velocity curves that might be expected for the lower velocity modes of failure.

We computed this residual velocity vs striking velocity curve, using, however, not the instantaneous value for fracture but the stress vs time-to-fracture curve given by Zhurkov for aluminum. In these cases the predicted residual velocity curve as compared with the experimental curves were very

low and the predicted critical velocity was very much higher by about 50%. (Figure 35.)

If it is assumed that the time to fracture is instantaneous, a simpler version of this may be made. This model indeed has been computed in the literature a good many years ago by a Japanese scientist by the name of Nishiwaki[2], in 1951. In this case the bullet is treated as a rigid body moving in the plate with some critical velocity. It is acted upon with a resisting force by the plate consisting of a static part proportional to the membrane stress that was generated in plastic tension and a dynamic stress equal to the Bernoulli pressure. The motion of the projectile is taken until it passes through the plate without regard to the deformation of the plate. In this time of passage the forces are acting upon the bullet and the bullet slows down. (Figure 36.)

The residual velocity versus initial velocity curves are shown in Figure 37.

A typical residual velocity versus striking velocity curve is shown in Figure 37, where it is compared with the experimental data for a titanium alloy. It is noted that the residual velocity goes to zero at some finite value of the striking velocity. This is taken to be the critical velocity and is shown in the next figures. The critical velocity for perforation here is dependent on several factors:

1. the yield strength of the plate
2. the initial striking velocity
3. the plate thickness-to-bullet-length ratio.

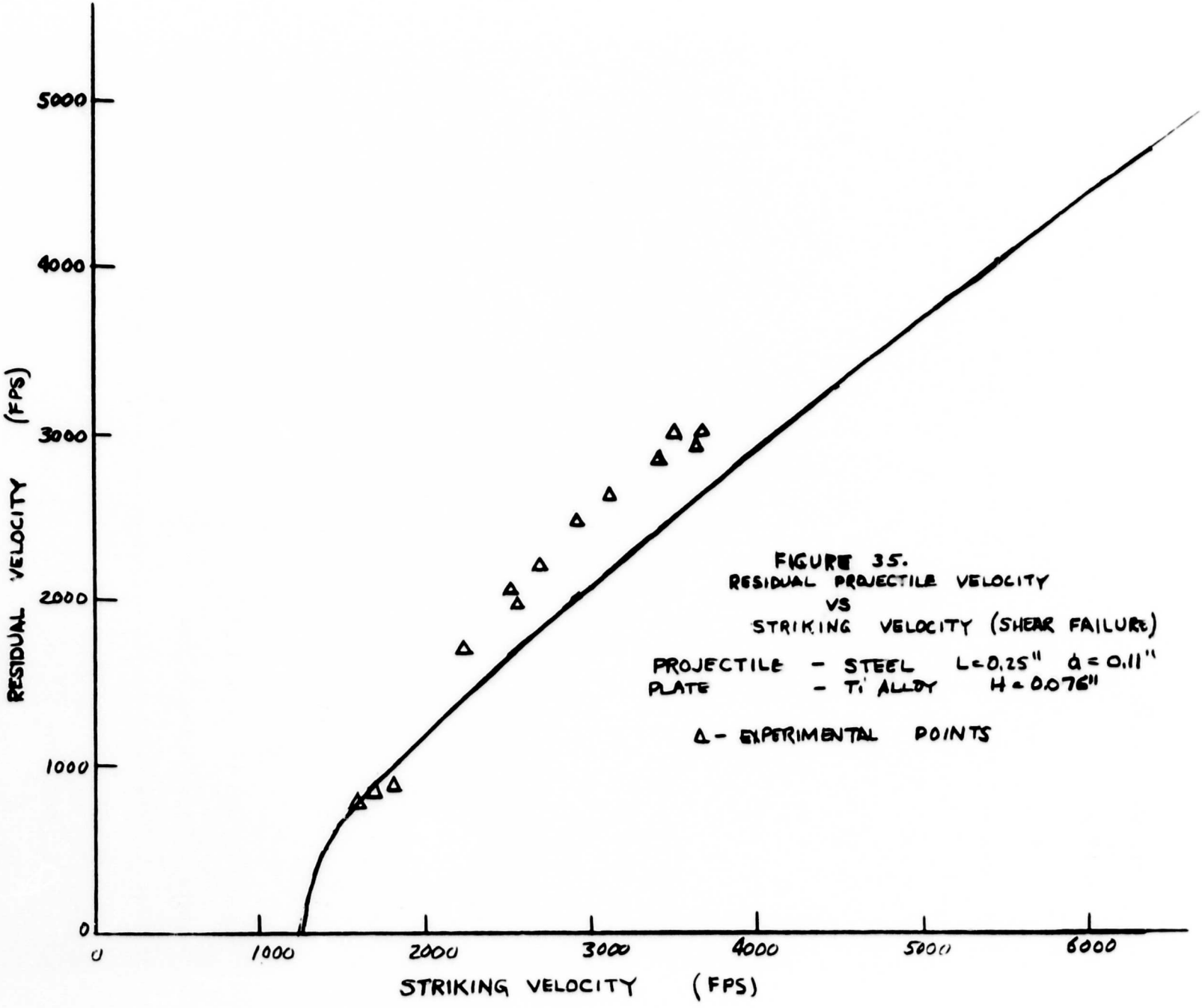

FIGURE 35.
RESIDUAL PROJECTILE VELOCITY
VS
STRIKING VELOCITY (SHEAR FAILURE)

$$V_r^2 = e^{-y}(V_s^2 - x) + x$$ **Residual Velocity**

$$x = \frac{\sigma_{ty}}{\rho_2}\frac{h}{a}$$

$$y = \frac{2\rho_2 h}{\rho_1 L}$$

$$V_{sc} = x^{1/2}\,(e^{-y} - 1)^{1/2}$$ **Critical Velocity**

Figure 36. Residual Projectile Velocity and Critical Perforation Velocity According to Nishiwaki

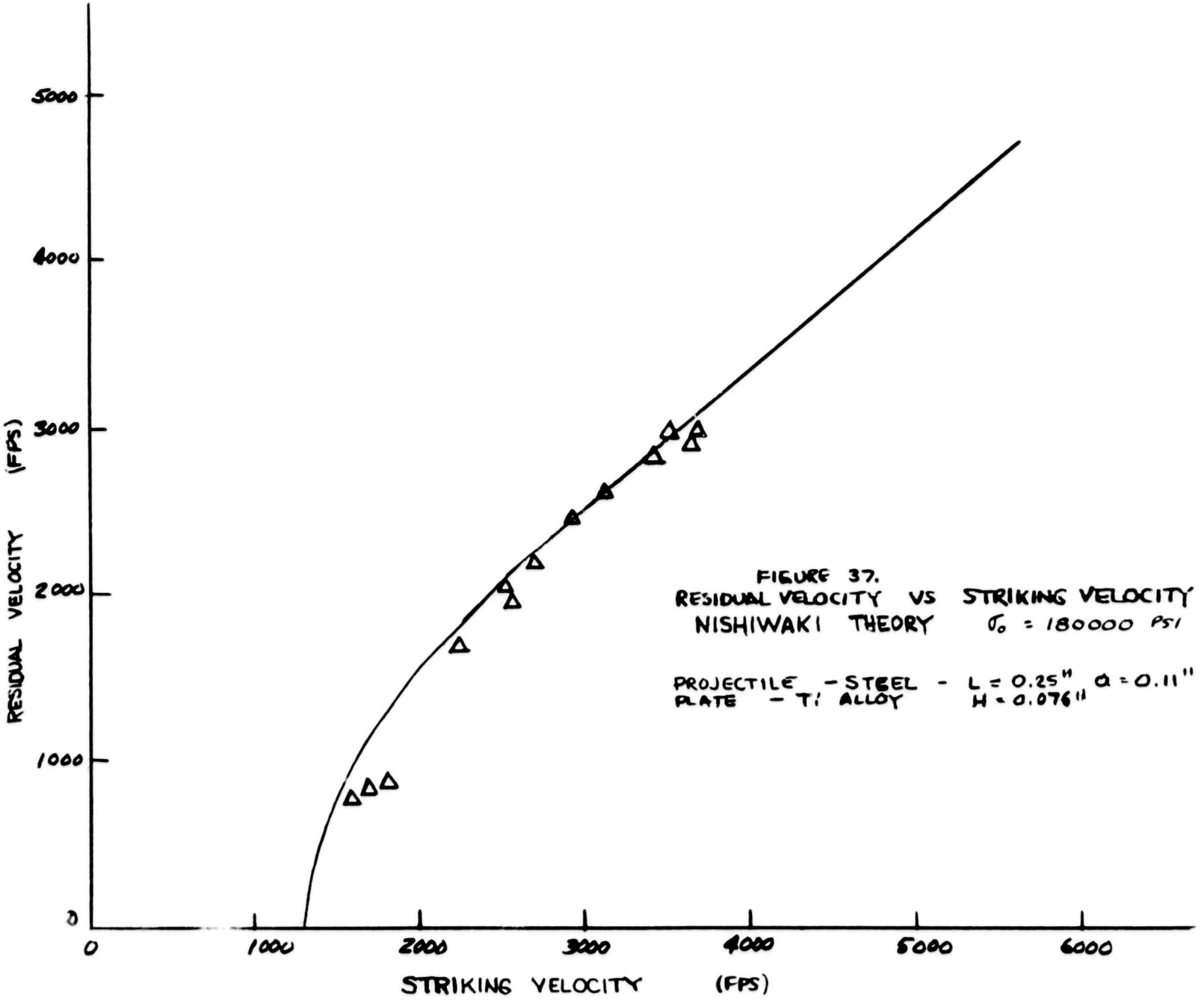

FIGURE 37.
RESIDUAL VELOCITY VS STRIKING VELOCITY
NISHIWAKI THEORY $\sigma_0 = 180000$ PSI

PROJECTILE - STEEL - L = 0.25" a = 0.11"
PLATE - Ti ALLOY H = 0.076"

The agreement of the Nishiwaki curve to experimental data in the very thin plate and low-to-moderate impact velocity regime is very excellent. It is only at the higher velocity and thicker plates that this theory tends to become less accurate.

Let us now examine the results of combining all the theoretical and experimental approaches. For a given plate material projectile combination we shall now examine the predicted critical velocity in light of the directly propagated stress wave failure and the slow time failure given by the Nishiwaki equation. The composite of all the predicted residual velocity curves for a typical titanium alloy is shown in Figure 38. The critical penetration velocity vs plate thickness is shown for a titanium alloy - steel projectile combination in Figure 39. It is seen that, for very thin plates, the critical velocity is given essentially by the thickness-to-length ratio whereas, for thicker plates, it is given by the thickness-to-bullet-radius ratio. In both cases the strength of the plate is a factor.

For general design purposes, then, both failure by the directly propagated stress wave given by impact and the long time failure in response to the membrane stresses as predicted by Nishiwaki theory must be calculated to evaluate the ballistic resistance of the plate.

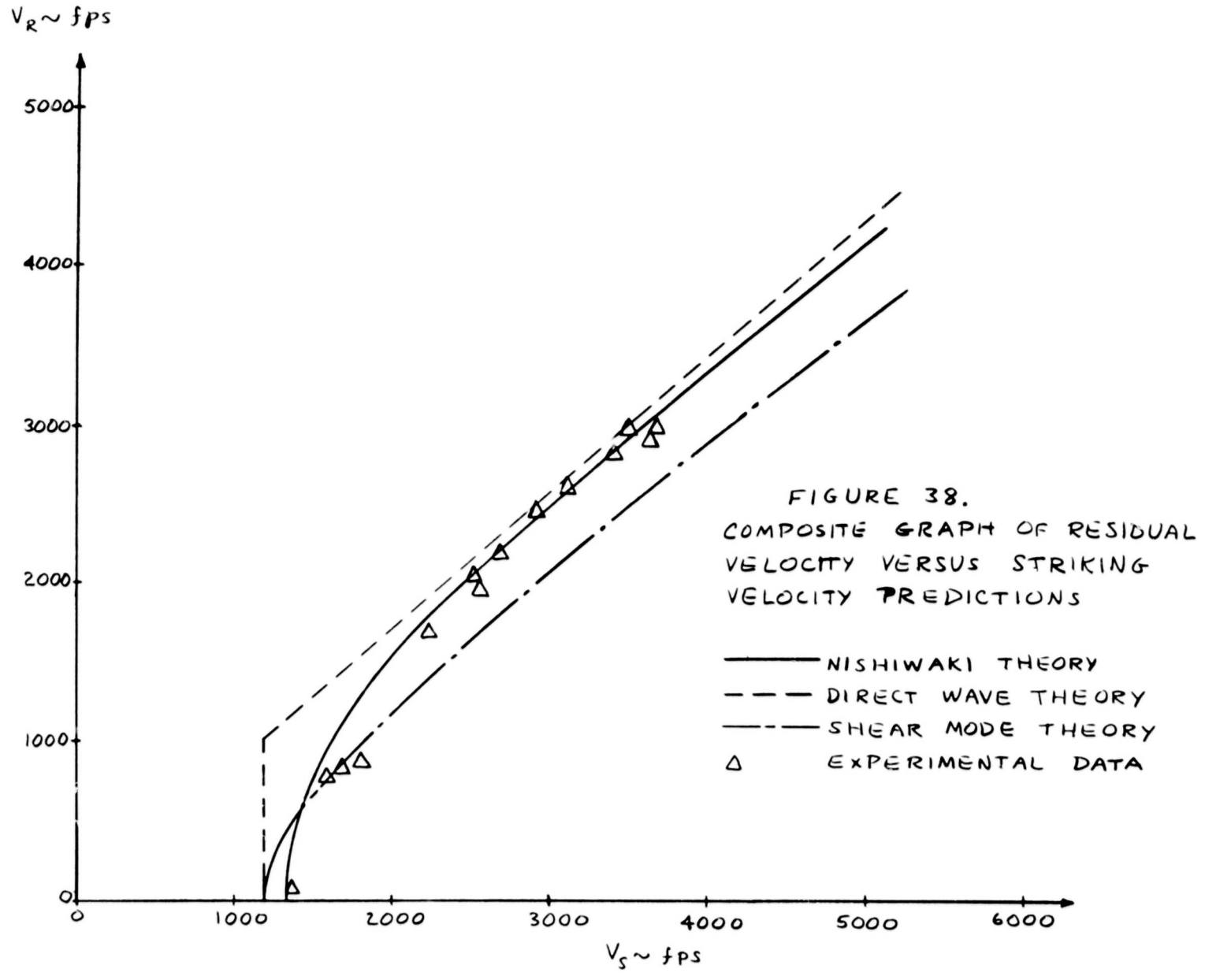

FIGURE 38.
COMPOSITE GRAPH OF RESIDUAL VELOCITY VERSUS STRIKING VELOCITY PREDICTIONS

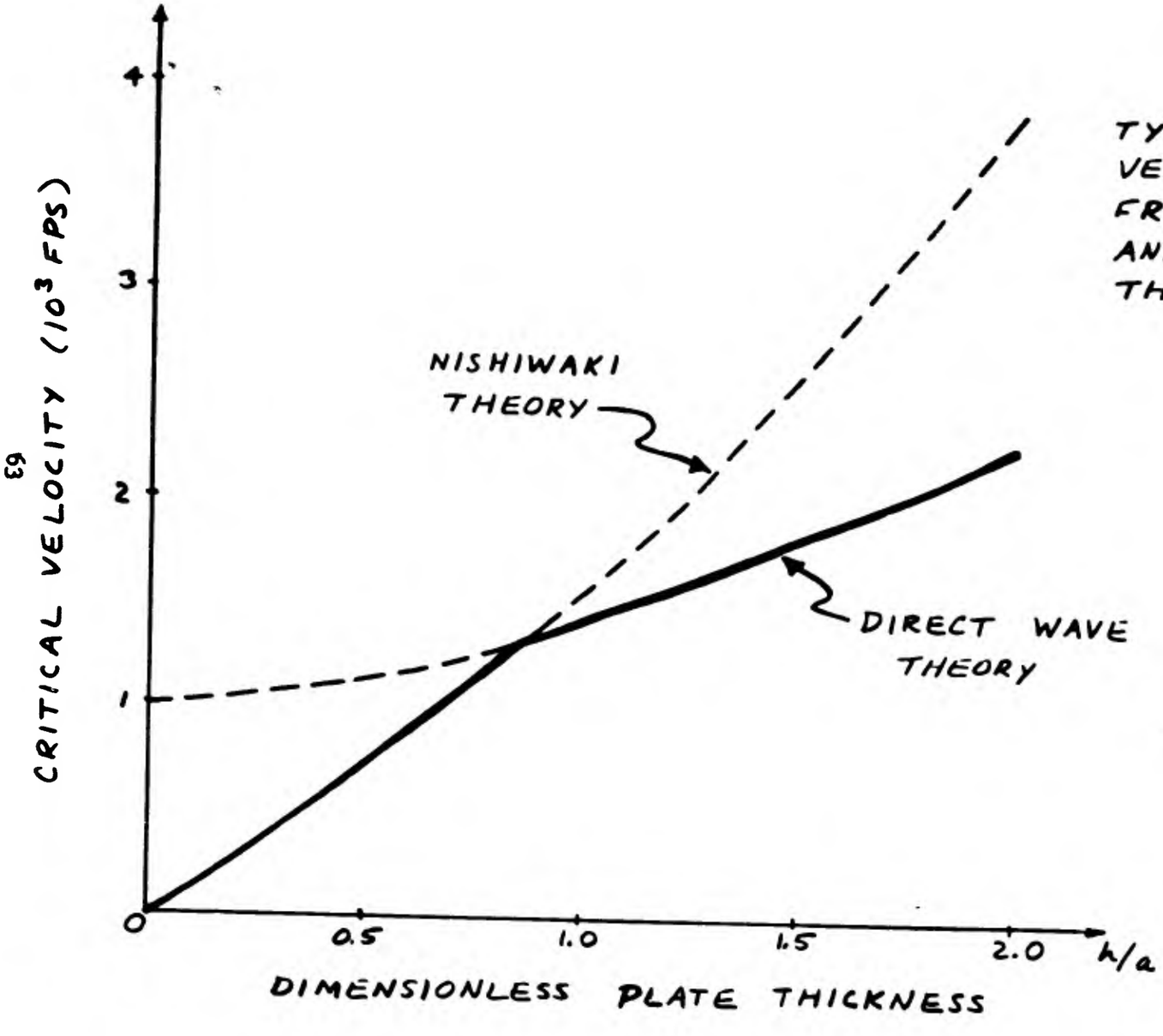

FIGURE 39.
TYPICAL CRITICAL VELOCITY PREDICTIONS FROM THE NISHIWAKI AND DIRECT WAVE THEORIES

PREDICTIONS FOR Ti ALLOY PLATES
σ_0 = 180,000 PSI
STEEL BULLET
L = 0.25 IN.
a = 0.11 IN.

SECTION 4

SUMMARY AND CONCLUSIONS

4.1 Summary

Two broad areas of analytical study on problems pertaining to the penetration and perforation of metallic plates and laminates by projectiles were conducted by MRD. These were (1) the determination of stress wave propagation, both elastic and plastic, in a plate induced by ballistic impact, (2) studies of material behavior at high strain rates.

The plate or laminate will fail in response to the stresses that are propagated through it. Specifically, the plate may fail by

(1) Spall

(2) Cavitation

(3) Plugging

(4) Petalling

(5) Radial fracture in laminates

The dominant modes of failure for design purposes are the cavitation mode and the tensile or petalling mode. Residual velocity and critical velocity calculations and predictions have been made. These agree quite favorably with the observed data.

Various material parameters and geometrical parameters enter into the determination of the critical velocity. These are

(1) Thickness of the plate

(2) Radius and length of the bullet

(3) Transverse and normal strengths of the plate material

(4) Acoustic impedences

4.2 Current Research at MRD

An experimental program to investigate and substantiate the theoretical division of the modes of failure and their influence on the residual velocity curves and ballistic resistance in general has just been initiated at MRD.

The goal of the contract is to isolate the modes of failure of the plate in response to the impact stresses and to delineate and characterize each mode of failure and determine its range of applicability.

REFERENCES

1. Hopkins, H.G. and Kolsky, H., Proc. 4th Hypervelocity Symposium (1961)

2. Nishiwaki, J., Journal Phys. Soc. of Japan, 6, 374-378 (1951)

3. Fugelso, L. E., Arentz, A. A. Jr., and Poczatek, J. J., Mechanics of Penetration, Vol. I, Final Technical Report Contract DA 19-129-QM-1542 (1961)

4. Fugelso, L. E., Davidson, D. A., and Arentz, A. A. Jr., Mechanics of Penetration, Vol. II, Final Technical Report Contract DA-19-129-QM-1542 (1961)

5. Fugelso, L. E., Analytic Study of Early Motion Caused by an Underground Detonation, Final Technical Report Contract DA-49-046-XZ-088 (1962)

6. Fugelso, L. E., Close-in Effect from a Surface Nuclear Burst, Final Technical Report, Contract AF 29(601)-5009 (in preparation)

7. Catlin, J.P. and Wentz, W. W., Effect of Strain Rate of the Mechanical Properties of Titanium Base Materials, WADD Technical Report 53-71 (1960)

8. Zhurkov, S. N. and Sanfirova, T.P., Soviet Physics Technical Physics, 2, 1586-1592 (1958)

A THEORETICAL STUDY OF LOW VELOCITY PENETRATION PHENOMENA

by

Dr. Emerson Cannon
Christopher R. Wylie

Utah Research and Development Company

TABLE OF CONTENTS

Table of Contents (Continued)

ABSTRACT

A new formulation of elasto-plastic rate-dependent material behavior is discussed. A numerical method and computer code (FORTRAN IV for IBM-7040) have been developed for the determination of two-dimensional displacement fields in large-deformation impact situations. Preliminary numerical results are presented for the collision of two identical aluminum bars.

1. INTRODUCTION

1.0 Introduction to the Over-all Problem

This report presents a review of the initial work on a much larger problem. The over-all investigation has three principal goals:

1. The construction of a theory and computational scheme for the quantitative prediction of low velocity impact phenomena (when the material properties and geometry are given).

2. The determination of the dynamic properties of various materials of interest from the theoretical interpretation of experimental data.

3. The design of materials and geometries for various types of protective armor.

The theoretical method for the quantitative prediction of impact phenomena must be sufficiently general to permit the solution of systems which are complicated enough to be of practical use. It demands that the following should be accounted for:

1. Large deformation gradients necessitating the use of nonlinear geometric theory.

2. General, nonlinear (but continuous), rate dependent, elasto-plastic stress-strain relations.

3. Boundary conditions of sliding and nonsliding surfaces in contact.

4. Various geometries: Impacts of projectiles having rather arbitrary cylindrical profiles impacting into multi-layered targets.

The theory of material phenomena is presently unsettled. There is much disagreement concerning the proper qualitative nature of the theory.

With the limitations of current mathematics, computations of practical interest are exceedingly difficult and subject to some considerable inaccuracies. One of the major goals of this project is to develop mathematical tools for the solution of more general mathematical models arising from various physical theories of material behavior. Clearly, this must be done before any physical theory is of practical utility.

1.1 Introduction to the Particular Problem of This Study

This study is in three parts, the first of which is now completed and is described in this report.

An outline of the particular goals of the project is given below. Parts II and III are included here to indicate the direction of future work.

Part I

1. Review of physical theory and construction of a simple physical model.

2. Mathematical formulation of the physical model.

3. Development of computational methods for solving mathematical models giving the time-dependent displacement and velocity fields within impacting materials.

Part II

1. Extension and refinement of the computational methods.

2. Verification of the computational techniques and mathematical model by comparing the theoretical calculations for a relatively simple model with classical results (where possible) and experimental data.

3. Extension of the mathematical model and computational scheme to the case of simultaneous elastic and plastic forces.

4. Theoretical calculations for several models that will be simulated experimentally.

5. Deduction of the proper form of the stress-strain relations of several materials by adjusting the numerical parameters in the mathematical model until the theoretical calculations coincide with the actual experiments.

Part III

1. Extension of the computational scheme to the more complicated geometries of practical interest.

2. Theoretical calculation of various impact configurations over time periods covering an entire impact or penetration (using the experimentally derived stress-strain relations from Phase II, step 5).

3. Interpretation of the results of step 4 to better understand the influence of various material properties and geometrical structures on impact and penetration phenomena.

1.2 Preliminary Results and Progress

The physical theory of materials has been reviewed and the effects we consider pertinent to the problem have been isolated.

We have expressed these effects in a novel but convenient mathematical form. The continuum form of the mathematics was converted to a discrete variable version for computational reasons.

Considerable work was necessary to develop a numerical method and computer code for solving the discrete variable model. The computer code is now performing properly in the calculation of the two-dimensional displacement and velocity fields for the impact of two prisms.* The computer code must now be refined and optimized for further studies.

The displacement and velocity fields in the two prisms correspond quite well with extrapolated classical theory. Our greatest interest at this time is the further improvement of the shock behavior and the running time of the computer code. Then the code will be extended to handle simultaneous elastic and plastic stresses and strains.

The work thus far shows the basic feasibility of our numerical method in handling nonlinear impact problems.

---

* The problem has been reduced from three spatial coordinates to only two by the use of symmetry relations. Nonsymmetrical problems in three dimensions pose no particular theoretical difficulties, but at present only the largest electronic computers could achieve a numerical solution.

2. CONTINUUM THEORY

2.0 The Important Mechanisms in Low-Velocity Impacts

All properties of a material may ultimately be traced to its atomic and molecular structure. Unfortunately, the currently limited understanding of the relation of molecular and macro physical theories does not yet permit the accurate derivation of macro properties from hypothesized molecular structure. Therefore, molecular theory can be used only as a qualitative guide in planning a program to describe and measure material properties on the macro level.

We have somewhat arbitrarily divided the principle effects in low velocity impacts into generic classes. These are listed approximately in order of their relevancy.

1. Elastic Deformation
2. Plastic Deformation
3. Fracture and Fragmentation
4. Spray Particles and Other Ejecta
5. Sliding Interface Friction
6. Shock Heating
7. Change of Crystal Structure
8. Change of Phase
9. Chemical Reaction
10. Optical Radiation

This report is limited to the first three (and mainly the first two) effects. The remaining topics are either of minor importance or are too complicated to be treated adequately at this time. Work on effects four and five is to be taken up later in the project.

2.1 Geometrical Description of Material Effects

Elasticity, plasticity, etc. will be described in terms of the deformation of an infinitesimal cube. It can be shown that this approach leads to an invariant formulation in the tensor sense.

In the initial undeformed state, the material points are referred to an orthonormal vector basis $\vec{I}_i$.* Every material point P is associated with a position vector $\vec{P} = z^i \vec{I}_i$.

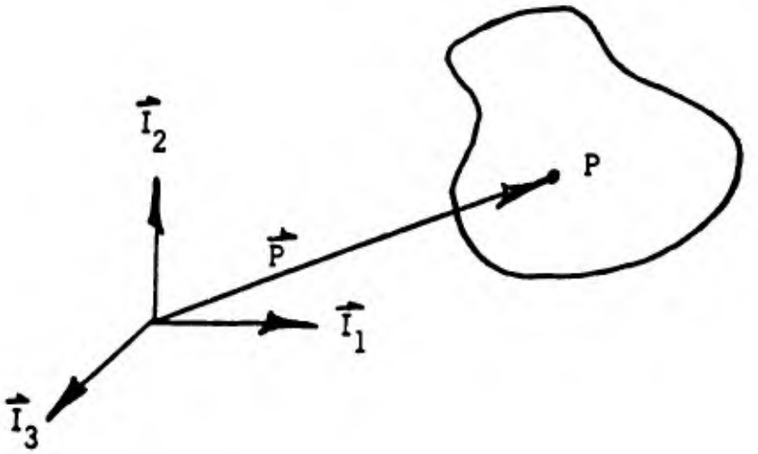

At each mass point P, a set of three infinitesimal orthogonal vectors $\vec{S}_i$ are chosen to represent the sides of an infinitesimal parallelepiped.

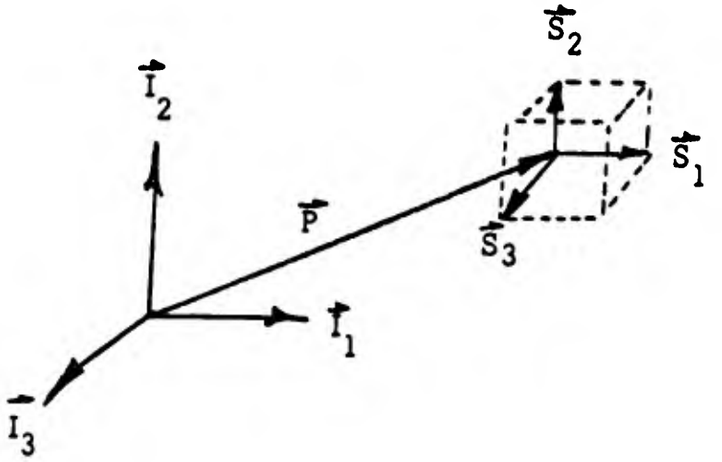

---

* See Appendix C for an explanation of the coordinate system conventions used in this report.

The infinitesimal side vectors are chosen parallel to the basis $\vec{I}_i$ so that $\vec{S}_i = dz^i \vec{I}_i$.

At later times the $\vec{S}_i$ are transformed in $\vec{s}_i$ which describe a deformed parallelepiped. The locally linear transformation connecting $\vec{S}_i$ and $\vec{s}_i$ is

$$\vec{s}_j = B_j{}^i \vec{S}_i$$

$$B_j{}^i = \frac{dY^i}{dY^j}$$

$\vec{S}_i$ basis

Y^i coordinates

y^i coordinates

$\vec{s}_j$ basis

The specification of the $\vec{s}_i$ basis (as a function of time) in terms of the $\vec{S}_j$ basis completely describes the geometrical deformation, and is therefore equivalent to the conventional strain tensor. The strain tensor is easily expressed in terms of $B_i{}^j$. However, the parallelepiped concept is much more intuitive.

Since the $\vec{S}_j$ are defined to be orthogonal and normalized, $B_i{}^j$ may be simply expressed as

$$B_i{}^j = \vec{s}_i \cdot \vec{S}_j \quad . \qquad B_i{}^j \text{ is not a tensor.}$$

The usefulness of $B_i{}^j$ arises from the fact that the stress vectors $\vec{M}_i$ in the $\vec{s}_i$ basis are

$$\vec{M}_i = a^{\underline{i}} \vec{s}_{\underline{i}} = a^{\underline{i}} B_{\underline{i}}{}^j \vec{S}_j$$

as a consequence of conservation of momentum applied to an infinitesimal parallelepiped. The $\vec{s}_i$ are called the image vectors. The a^i are scalar functions which determine the relation between deformation and stresses. The a^i presumably are functions of the image vectors, time derivatives and perhaps integrals. We chose not to make implicit use of the stress vectors in the stress-strain relation; i.e., the stress vectors are given explicitly in terms of functions of the image vectors. This suffers no real loss in generality and is more convenient computationally.

Graphically, the forces on an infinitesimal parallelepiped are always parallel to the adjacent sides and act through the center of each side.

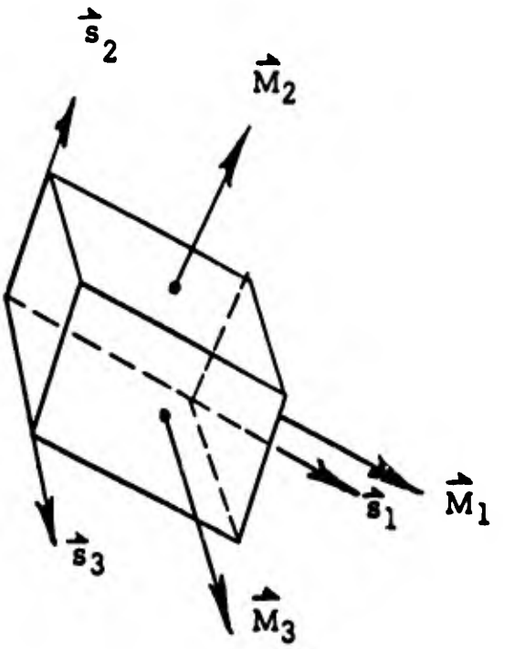

2.2 Isotropic Stress-Strain Relations

Any dynamic stress-strain relation must certainly reduce to the classical static form as the strains and time rates go to zero.

The volume of a deformed infinitesimal cube is (5,50)*

$$V^2 = \left| \hat{s}_i \cdot \hat{s}_j \right|$$

$$V = \sqrt{|s_{ij}|}$$

where s_{ij} is the metric derived from the basis $\hat{s}_i$.

The stress-strain law of a material is conveniently stated in terms of the volume and side length changes and their time rates. The various molecular theories of materials seem to indicate that these quantities are of fundamental importance. Therefore, material forces may be visualized as arising from volume effects and side extensions. In isotropic media, this argument leads to two scalar functions: one for the volume effect and one for the extension effect.

The obvious place to start building a stress-strain relation is with the static, linear results. As an infinitesimal cube is deformed, forces arise as a result of the stretching or extension of its sides. For small variances these forces are assumed to be linear with side length change and the proportionality constant is the classical Young's modulus. The "shear" forces arise from volume change effects. Volume change forces are also assumed (for the moment) to be linearly dependent on the volume change. Expressed mathematically,

$$a^i = \left(\frac{1}{L_i} k_1 \left[V - 1 \right] + k_2 \left[L_i - 1 \right] \right)$$

where the initial volume and initial lengths are unity and k_1 and k_2 are scalar parameters.

---

* This is the convention used in this report to indicate reference work. The first number is the reference number (found in Appendix F) and the second is the page number.

The extension modulus is not expected (predicted from molecular theory) to vary much with strain rate. Therefore, k_2 is reasonably assumed to be constant. The volume change effect is equivalent to the equation of state. This is somewhat dependent on the volume. The Los Alamos data will be used as an initial approximation for this relation. It has been experimentally observed that most materials are very nearly linear throughout their elastic range in extension, but not in compression.

So far, the theory has been elastic, i.e., no permanent deformations. Plastic (inelastic) effects are most naturally described in terms of strain and stress rates. It is believed that plastic phenomena arise largely from dislocation movement in the crystal structure. At normal temperatures most solids have an elastic region of strain and permanently deform when that range is exceeded. The transition point where the strain acquires a permanent component is called the yield point and is of great interest. At the yield point, the stress-strain law must be modified to account for plastic flow (permanent deformation).

The magnitudes of the side vectors $\vec{s}_i$ are

$$L_i = \overline{MAG} \circ \vec{s}_i = \sqrt{\vec{s}_i \cdot \vec{s}_i} = \sqrt{s_{\underline{ii}}}$$

If the absolute value of the difference in any pair of side vectors' magnitudes is greater than the yield level Y, the material is in a state of plastic flow. This is similar to the Tresca yield condition. The dependence of the stresses in plastic flow on the deformation rate can be formulated using the time rates of various measures of deformation.

A fundamental assumption in our work is that the a^i relating the stress tensor to the strain image tensor are given by functions of scalar tensor invariants. Some useful invariants are listed below.

$$\text{Volume} = V = \left| \vec{s}_i \cdot \vec{s}_j \right|^{1/2}$$

$$\text{Volume rate} = \frac{dV}{dt} \text{ (ordinary differentiation)}$$

$$\text{Side lengths} = L_i = (s_{ii})^{1/2} = (\vec{s}_i \cdot \vec{s}_i)^{1/2}$$

$$\text{Side length rates} = \frac{dL_i}{dt} \text{ (ordinary differentiation)}$$

$$\text{Average of side lengths} = A = \frac{L_1 + L_2 + L_3}{3}$$

$$\text{Side length imbalance} = B_i = (L_i - A)^2$$

This simplifies the mathematics considerably but retains the generality of more complicated formulations. Some of the e..pressions for a^i that we are now experimenting with are

$$a^i = \left[k_1 \left(\frac{1}{V} - 1\right) + k_2 \left(\frac{1}{L_i} - 1\right)\right] \frac{1}{L_i}$$

for the elastic range and

$$a^i = \left[k_1 \left(\frac{1}{V} - 1\right) + k_3 \frac{dB_i}{dt}\right] \frac{1}{L_i}$$

for the plastic range.

General, <u>simultaneous</u> elastic and plastic effects can only be described by the decomposition of the total strain into an elastic strain and a plastic strain. There are then two unknown strains, viz.,any two of the plastic, elastic, and total strains. This is a vastly more complicated problem and will be undertaken later in the project.

2.3 Equations of Motion

The law of motion in invariant form is

$$\vec{F} = m\vec{A}$$

where $\vec{F}$ is the net force vector acting on mass m, and $\vec{A}$ is the acceleration vector.

For the present we assume that the spatial coordinates X^i are rectangular and coincident with the underlying reference $z_i\vec{I}$. In this case the original undeformed material cubes are parallel to the coordinate lines. Curvilinear spatial coordinates will be considered in later work.

The law of motion is simply

$$\frac{d}{dX^i}(\vec{M}_1 + \vec{M}_2 + \vec{M}_3) = \rho\frac{d^2\vec{P}}{dt^2}$$

where ρ is the density and $\vec{P}$ is the position vector expressed in the X^i.

3. DISCRETE VARIABLE MODEL

3.0 Introduction to the Computational Approach

A simple problem was chosen to facilitate the construction of the initial version of the computer code. One prism, traveling at one kilometer per second, collides with an identical prism which is at rest. It is assumed that there is no slippage of the surfaces at the interface.

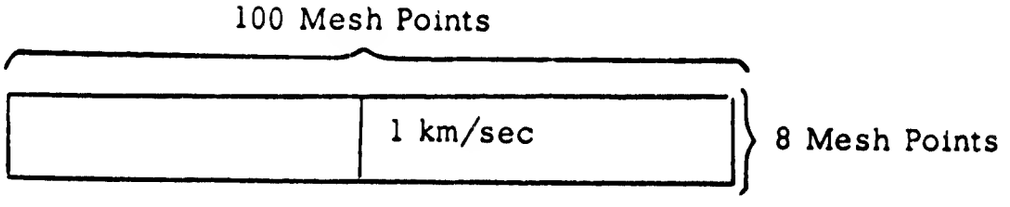

The discrete variable mesh is depicted below. The positions of the mass points are the mesh variables.

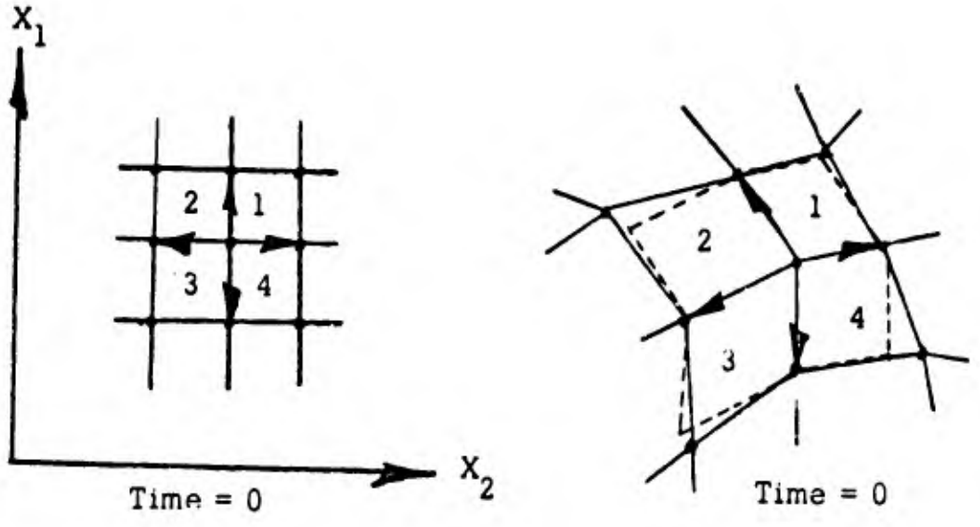

At each of the points there is a concentrated mass surrounded by four massless material squares. At time-zero each point P has four unit vectors attached to it. These vectors are defined to be the unit length, directed line segments connecting P with its four nearest neighbors. As the points move (the material deforms) the vectors change length and orientation. The two vectors defining each of the four quadrants around P can be considered as undergoing a linear transformation from their initial (undeformed) to the deformed states.

Since the original two vectors are orthonormal, the transformation is just a matrix whose rows are just the components of two vectors after deformation. It can easily be shown that if the transformation matrix is denoted by A^I_J, then the nonlinear strain tensor e_{ij} is simply

$$e_{ij} = A^I_i A^I_j - \delta_{ij}$$

The components of the two side vectors are the components of the strain image tensor and are easily obtained from the tabulated mesh variables by a few subtractions. This makes calculation of the conventional nonlinear strain tensor trivial.

A^I_J is numerically identical to the strain image tensor. With the strain image tensor easily available, the stress tensor can be calculated from whatever stress-strain relation is being used. The four different states of deformation of the four material squares around P give rise to four forces which add to produce a resultant force at point P. The strain image tensor and its time derivative are used to calculate the stress vectors acting on the faces of each of the four parallelepipeds around point P. The stress-strain relations are the ones mentioned in Section 3.1.

The acceleration of point P is a simple calculation in these coordinates. An error vector at every point P is defined to be

$$\vec{E} = \vec{F} - m\vec{A}$$

where $\vec{E}$ = error vector

$\vec{A}$ = acceleration vector

$\vec{F}$ = net force vector

m = mass of point P.

Clearly at any given time point, the convergence criterion is that the length of the error vector at any point in the mesh is under some acceptable level.

Starting from time zero, a predictor routine uses the past velocities and accelerations to predict the positions of the mass (mesh) points at the next time position. There will be some error in the prediction. The corrector proceeds to systematically eliminate the error (reduce the error vectors to zero).

It can be shown that if all of the mass points are displaced from their predicted positions by a correction vector which is calculated from the error vectors and their derivatives, all the errors will simultaneously

decrease. The points are moved, the error vectors calculated again, and the process repeated until the error is reduced sufficiently. Then the prediction of the mass point positions is made for the next point in time. The corrector process is again used to converge to proper mass point positions from this time point.

3.1 Stress-Strain Relation

The relations we are presently using give the force vector across each face of the deformed parallelepiped (only two-dimensional in this problem) in terms of its side vectors (components of its strain image tensor).

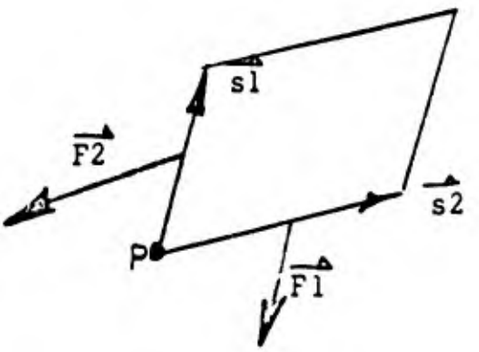

The side vectors $\vec{s1}$ and $\vec{s2}$ are shown in their positive directions and the force vectors are shown in their negative directions. $\vec{s1}$ and $\vec{s2}$ were originally orthonormal.

The force $\vec{F}$, acting on P as a result of the deformed material square shown, is

$$\vec{F} = \frac{\vec{F1} + \vec{F2}}{2}$$

In the computer code, the following simple stress-strain rule is being used in order to be able to compare the numerical results with known work.

$$\vec{F2} = a_2 * \frac{\vec{s2}}{|\vec{s2}|}$$

$$\vec{F1} = a_1 * \frac{\vec{s1}}{|\vec{s1}|}$$

V = volume of parallelepiped

where

$$a_1 = -k_1 * (|\vec{s1}| - 1) - k_2 * (V-1) + k_3 * \frac{d}{dt} |\vec{s1}|$$

$$a_2 = -k_1 * (|\vec{s2}| - 1) - k_2 * (V-1) + k_3 * \frac{d}{dt} |\vec{s2}|$$

k_1 and k_2 are the classical Lame's constants. k_3 is arbitrary at the present time. We have done some experimenting with different values of k_3 and have found that it affects the results dramatically.

Various nonlinear and rate dependent rules (extensions of Section 2.2) are being programmed for computer analysis, but we do not have the numerical results at this time.

3.2 Boundary Conditions

Because the forces from each material square are calculated independently of the others, the boundary conditions are trivial. A control number is recorded at each material square and indicates, among other things, the type of material in that square.

For example,

Symmetry Line

V	V	V	V	Al	Al	Al
V	V	V	V	Al	Al	Al
V	V	V	V	Al	Al	Al
V	V	V	V	Al	Al	Al
Fe	Fe	Fe	Fe	Fe	Fe	Fe
Fe	Fe	Fe	Fe	Fe	Fe	Fe
Gl	Gl	Gl	Gl	Gl	Gl	Gl

where V denotes vacuum
Al denotes aluminum
Fe denotes steel
Gl denotes glass

In this way the boundary conditions take care of themselves.

Curved boundaries may be approximated by jagged rectangular boundaries or by a more sophisticated scheme like interpolation, etc. If the number of mesh points is reasonably large, jagged rectangular boundaries may be reasonable approximations.

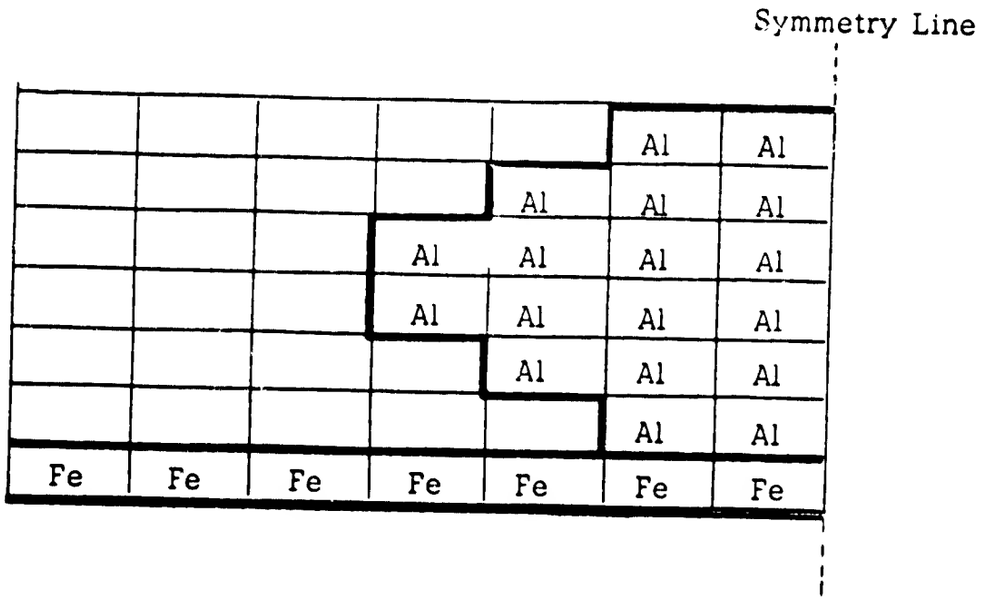

4. RESULTS AND CONCLUSIONS

4.0 Preliminary Numerical Results

The problem we have used in developing the computer code is the end-on impact of two identical prisms having a relative velocity of 1 km/sec. The material was aluminum and the standard values of the static elastic constants were used in a linear elastic relation. Rate dependence (as a sort of viscosity) was added and was varied from none to dependence on second time derivatives.

It should be emphasized that these results are preliminary and are presented as evidence of the feasibility of the general numerical method. Thus far, we have not critically compared these results with other work in the field. The detailed examination of the spectrum of likely stress-strain rules is also just beginning.

The graphical display in Figures 4.1-1 through 4.1-4 shows the mesh and samplings of the velocity field at times shortly after impact. The displacements are still small. These calculations took about ten minutes on an IBM-7040. Output was generated only every five time points.

The rate of propagation of the displacement wave is about 5 km/sec, which agrees with the measured speed of sound in aluminum (7,1863). As deduced from Riney's work, the shape of the velocity profile is about as it should be for a strongly rate-dependent stress-strain rule (8,32). The rule used in these computations was

$$\vec{F}_i = a^i \underline{\vec{s}}_i$$

$$a^i = \frac{1}{L_i}\left[k_1 (V - 1) + k_2 (L_i - 1) + k_3 \left(\frac{d^2 L_i}{dt^2}\right)\right]$$

where $\vec{F}_i$ is the stress vector through side i. See section 2.2 for notation and details.

The basic numerical method is applicable to more interesting models. In the next phase of our work we will consider, among other things, cylindrical geometries, nonlinear elastic rules and simultaneous elastic and plastic stresses.

As soon as we optimize the computer code and decide upon a stress-strain rule, we will make long-time runs to observe large plastic deformations.

INITIAL CONFIGURATION

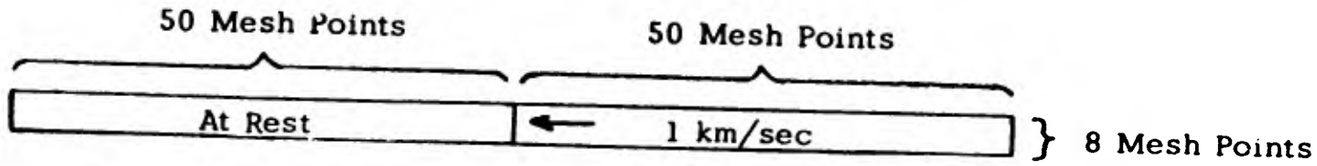

FIGURE 4.1-1

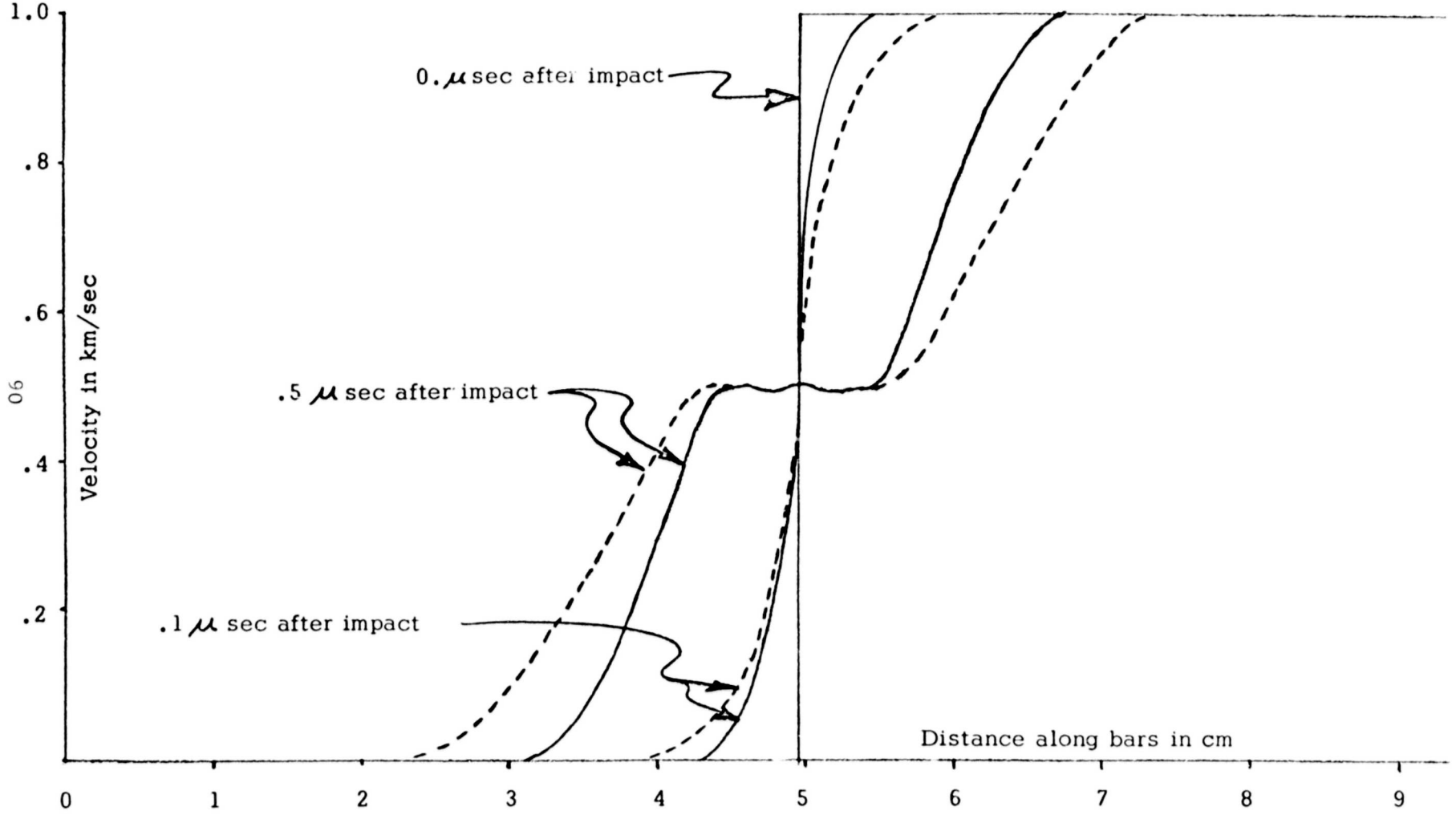

FIGURE 4.1-2

Longitudinal Component of the Velocity Profile along the Bars.
Dotted lines are profiles at the center.
Solid lines are profiles at the surface.

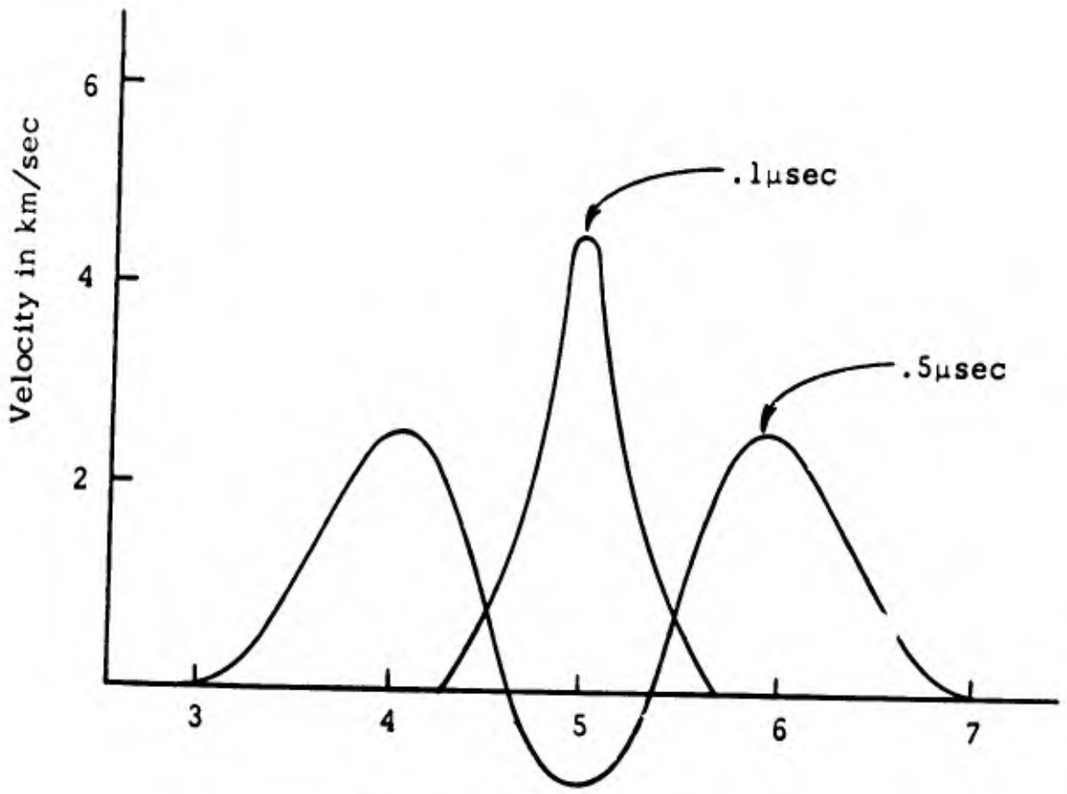

Profile of Transverse Component of Velocity at Surface of Bars

FIGURE 4.1-3

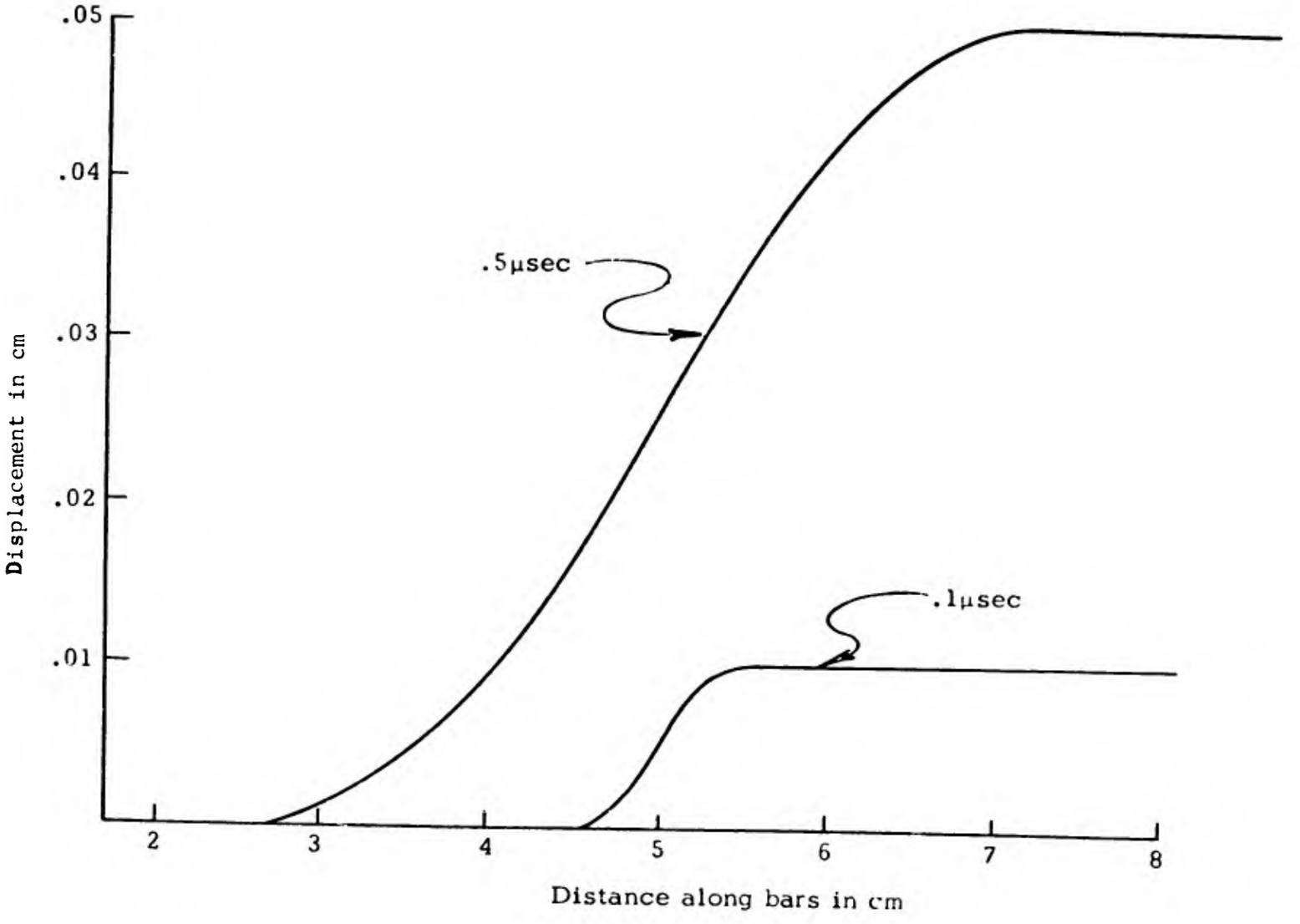

Longitudinal Displacement Profile Down the Center of the Bars

FIGURE 4.1-4

APPENDIX A: OUTLINE OF NOTATION

A.1 Variable Symbols

1. A variable may be represented by a simple variable symbol such as

   $$a, x, y, r, \alpha \quad \text{etc.}$$

   or a compound variable symbol such as

   $$\overline{X11C2}, \quad \overline{BAT}, \quad \overline{DOT}, \quad \overline{HEAT}$$

   A compound variable symbol must start with a letter and be tied together with a bar.

2. Indices which are not of tensor nature may be included in parentheses within a compound variable symbol.

   $$\overline{X1(I,J)}, \quad \overline{BAT(1,K)}, \quad \text{etc.}$$

3. When discussing transformations, variables beginning with upper case letters refer to the initial space and variables beginning with lower case letters refer to the space after transformation.

4. A variable symbol with subscript or superscript indices represents a set of quantities. An arrow over the variable symbol indicates that each of the elements is a tensor.

Example

Consider a vector (a first order tensor) in space.

$$\vec{V} = V^k \vec{e}_k$$

Note

$\vec{V}$ is a tensor

$\vec{e}_k$ is a set of 3 tensors which form a basis in which $\vec{V}$ can be expressed.

V^k are the components of the tensor referred to the basis $\vec{e}_k$

A.2 Rules for Indexed Variables

1. Indices appear as subscripts or superscripts or within the variable symbol.
2. When a variable is a tensor, the subscripts refer to covariant components and superscripts refer to contravariant components.
3. When discussing transformations, upper case indices usually are used to refer to initial coordinates and lower case indices to refer to the transformed coordinates.
4. When an index appears more than once in a product, that index is summed over its range.
5. A bar under an index suspends the summation convention on that index only for that variable.

6. A bar over an index means that the index is not a tensor index.

7. Parentheses around a tensor index mean that the index refers to the physical components of the tensor.

8. Exponents on a variable are always superscripts. Whenever there is a possibility of confusion, the exponent is put in brackets or parentheses.

Example

$$\overline{XX}^{I}_{J}\,[2X+1] \equiv (\overline{XX}^{I}_{J})^{2X+1}$$

A..3 Operation Symbols

1.	Summation	$\sum$
2.	Determinant	$\lvert\ \rvert$
3.	Scalar Multiplication of A and B	A*B or AB
4.	Addition	+
5.	Subtraction	-
6.	A divided by B	$\frac{A}{B}$ or A/B
7.	Absolute Value	$\lVert\ \rVert$ or $\overline{\text{ABS}}$.
8.	Integral	$\int$
9.	Operator "f" acting on argument "X"	f • X or f • (X)
10.	Ordering of operations uses parentheses and brackets	( ) [ ]

11. Inner or dot product of two vectors $\vec{A} \cdot \vec{B}$

12. Cross product of two vectors $\vec{A} \times \vec{B}$

13. Tensor product of two tensors $\vec{A} \otimes \vec{B}$

14. Magnitude or modulus of a vector $\overline{MAG}\bullet$ or $MOD\bullet$

A.4 Common Operators

1. The very commonly used functional operators such as trig functions, etc., are not required to have the operation symbol.

   Example

   $$\sin \Theta \equiv \overline{\sin} \bullet \Theta$$

2. $\frac{dX}{dY}$ is the partial of X with respect to Y.

3. A comma may be used to indicate ordinary partial differentiation.

   $$\frac{dY^i}{dX^j} = Y^i{}_{,j} \quad \text{and} \quad \frac{dY_i}{dX^j} = Y_{i,j}$$

4. A ∇ is used to indicate the covariant or absolute differential of a quantity.

   Example

   The absolute differential of a tensor $\vec{X}$ with respect to Y^j is

   $$\overrightarrow{\nabla X}_{,j} = \frac{\nabla \vec{X}}{dY^j}$$

5. A semicolon is used to indicate covariant or absolute differentiation of tensor components.

   Example

   $$Y^i{}_{;j} \text{ and } Y_{i;ji} \text{ etc.}$$

A.5 Special Symbols

1. The generalized Kroneker delta is defined as

$$\delta^{mn\ldots pq}_{ij\ldots kl} = \begin{cases} 0 \text{ when the indices are all numerically equal} \\ 1 \text{ otherwise} \end{cases}$$

2. The permutation symbol is defined as

$$E_{ij\ldots kl} = \begin{cases} 1 & \text{for even permutations of the indices} \\ -1 & \text{for odd permutations} \\ 0 & \text{otherwise} \end{cases}$$

APPENDIX B: SOME DEFINITIONS CONCERNING VECTOR AND TENSOR SPACES OVER THE FIELD OF REAL NUMBERS

B.1 Scalar Multiplication in a Vector Space

The vector $\vec{X}$ is an undefined abstract quantity. Multiplying a vector $\vec{X}$, by a real number, b, is written (5,1)

$$b*\vec{X} \text{ or simply } b\vec{X}$$

The asterisk is used when there may be confusion with other product and functional notations.

1. $1*\vec{X} = \vec{X}$
2. $a*\vec{X}+b*\vec{Y} = b*\vec{Y}+a*\vec{X}$
3. $a*(b*\vec{X}) = (a*b)*\vec{X}$
4. $(a+b)*\vec{X} = a*\vec{X}+b*\vec{X}$
5. $a*(\vec{X}+\vec{Y}) = a*\vec{X}+a*\vec{Y}$
6. $\vec{X}+\vec{Y}$ is undefined

B.2 Vector Spaces

Any n distinct vectors $\vec{X}_i$ may be used to generate a vector space. The space is the collection of all possible $a^i \vec{X}_i$ where the a^i are selected from the real numbers. The $a^i \vec{X}_i$ are also called vectors. Since there are n vectors used in the linear form, $a^i \vec{X}_i$, the space generated is said to be n-dimensional.

A general vector in the space may be symbolized $\vec{V} = a^i \vec{X}_i$. The $\vec{X}_i$ are called the basis or generator vectors (or just the basis) of the space because all the vectors in the space are linear combinations of $\vec{X}_i$. The a^i are called the components of the vector $\vec{V} = a^i \vec{X}_i$.

B.3 Vector Addition

Referred to a basis, the addition of two arbitrary vectors in the space has the following meaning. If $\vec{V} = a^i \vec{X}_i$ and $\vec{W} = b^i \vec{X}_i$, the rules defining scalar combinations of vectors may be used to express the otherwise undefined sum of two vectors.

$$\vec{V} + \vec{W} = a^i \vec{X}_i + b^i \vec{X}_i$$

$$\vec{V} + \vec{W} = (a^i + b^i) \vec{X}_i$$

B.4 Vector Products

The addition of two different basis vectors is undefined except in terms of components relative to some other basis. However, several products of basis vectors are defined in terms of their properties.

B.5 Dot Product

The dot product of a pair of vectors is a scalar.

$$\vec{V} \cdot \vec{W} = \vec{V} \cdot \vec{W} = \text{some scalar}$$

$$(a\vec{V}) \cdot \vec{W} = a\,(\vec{V} \cdot \vec{W}) = \vec{V} \cdot (a\vec{W})$$

$$a(\vec{V} + \vec{W}) = a\vec{V} + a\vec{W}$$

The array of all the possible dot products of the basis vectors is

$$g_{ij} = \vec{X}_i \cdot \vec{X}_j = \text{array of scalars}$$

$$g_{ij} = g_{ji}$$

The symmetric array g_{ij} defines the numerical values of the dot products of the basis vectors and therefore all the vectors in the space.

$$\left(a^i \vec{X}_i\right) \cdot \left(b^j \vec{X}_j\right) = a^i b^j \left(\vec{X}_i \cdot \vec{X}_j\right) = a^i b^j g_{ij}$$

B.6 Tensor Products

The tensor product of two vectors is indicated

$$\vec{V} \otimes \vec{W}$$

and is in itself an undefined object. It is a tensor of rank two, being constructed from two tensors of rank one, namely vectors. Any number of vectors may form a tensor product. The tensor product of n vectors is a tensor of order n. All tensors are labeled with arrows over their symbol.

$$\vec{A} = \vec{B} \otimes \vec{C} \otimes \vec{D} \otimes \vec{E}$$

A is a fourth order tensor. Usually A has indices indicating its order, but in the instances where it does not, a number that indicates the order may be put over the arrow to avoid confusion.

$$\overset{4}{\vec{A}} = \vec{B} \otimes \vec{C} \otimes \vec{D} \otimes \vec{E}$$

The rules defining the tensor product are

1. $\vec{A} \otimes \vec{B} \neq \vec{B} \otimes \vec{A}$, in general
2. $\vec{A} \otimes (\vec{B} + \vec{C}) = \vec{A} \otimes \vec{B} + \vec{A} \otimes \vec{C}$

   $(\vec{B} + \vec{C}) \otimes \vec{A} = \vec{B} \otimes \vec{A} + \vec{C} \otimes \vec{A}$
3. $a * (\vec{B} \otimes \vec{C}) = (a * \vec{B}) \otimes \vec{C} = \vec{B} \otimes (a * \vec{C})$

As every vector is referred to a basis, likewise all second order tensors may be referred to a tensor basis of the form

$$\vec{X}_{ij} = \vec{X}_i \otimes \vec{X}_j$$

where $\vec{X}_i$ is a vector basis.

In general,

$$\vec{X}_{ijk \ldots z} = \vec{X}_i \otimes \vec{X}_j \otimes \vec{X}_j \otimes \ldots \otimes \vec{X}_z$$

B.7 Relation of the Dot and Tensor Products

$$\vec{V} \cdot (\vec{X} \otimes \vec{Y}) = (\vec{V} \cdot \vec{X}) * \vec{Y}$$

$$(\vec{X} \otimes \vec{Y}) \cdot \vec{V} = \vec{X} * (\vec{Y} \cdot \vec{V})$$

$$\vec{V} \cdot (\vec{X} \otimes \vec{Y} + \vec{Z} \otimes \vec{W}) = \vec{V} \cdot (\vec{X} \otimes \vec{Y}) + \vec{V} \cdot (\vec{Z} \otimes \vec{W})$$

In general,

$$\vec{V} \cdot (\vec{X} \otimes \vec{Y}) \neq \vec{X} * (\vec{V} \cdot \vec{Y})$$

B.8 Covariant and Contravariant Bases

The set of vectors $\vec{e}_i$ is a basis for an n-dimensional vector space. The subscript i indicates that they were arbitrarily chosen to be called a covariant basis. Vectors referred to a covariant basis have contravariant components, x^i. The index being in the superscript position indicates contravariant character.

For every covariant basis $\vec{e}_i$ there is a reciprocal contravariant basis $\vec{e}^i$ defined by

$$\vec{e}_i \cdot \vec{e}^j = \delta_i^{\ j}$$

This relation implicitly defines the reciprocal basis. Given a basis $\vec{e}_i$ it is a routine calculation to find the transformation, connecting $\vec{e}_i$ with $\vec{e}^i$.

$$\vec{e}^i = g^{ij}\,\vec{e}_j$$

The inverse transformation is g_{ij}. The g_{ij} and g^{ij} are the metrics of the $\vec{e}_i$ and $\vec{e}^j$ bases respectively.

B.9 Products of Covariant and Contravariant Vectors

The dot product rules are summarized below.

$$\vec{e}^i \cdot \vec{e}_j = \delta^i_{\ j}$$

$$\vec{e}^i \cdot \vec{e}^j = g^{ij}$$

$$\vec{e}_i \cdot \vec{e}_j = g_{ij}$$

Tensor products of covariant and contravariant vectors are called mixed tensors. For example,

$$\vec{e}_i \otimes \vec{e}^j \otimes \vec{e}_k = \vec{e}_i{}^j{}_k$$

The component representations of tensors in this basis are written

$$\vec{T} = t^i{}_j{}^k \vec{e}_i{}^j{}_k$$

B.10 Contracted Tensor Products

There are three possible dot products of the two tensors $(\vec{A} \otimes \vec{B} \otimes \vec{C})$ and $\vec{D}$.

$$(\vec{A} \cdot \vec{D}) * \vec{B} \otimes \vec{C}$$

$$(\vec{B} \cdot \vec{D}) * \vec{A} \otimes \vec{C}$$

$$(\vec{C} \cdot \vec{D}) * \vec{A} \otimes \vec{B}$$

These products are tensors of one lower order. In general, they are not identical, so that a particular product must be specified. The tensor $\vec{A} \otimes \vec{B} \otimes \vec{C} \otimes \vec{D}$ can be contracted by replacing one or more of the tensor products by dot products. For example,

$$(\vec{A} \cdot \vec{B}) * \vec{C} \otimes \vec{D}$$

$$(\vec{A} \cdot \vec{B}) * (\vec{C} \cdot \vec{D})$$

$$(\vec{A} \otimes \vec{D}) * (\vec{B} \cdot \vec{C})$$

Usually the factors of the products will have indices. When indicating the dot product of two tensor bases, the following convention is useful.

$$\vec{A}_i{}^j{}_k \equiv \vec{g}_i \otimes \vec{g}^j \otimes \vec{G}_k$$

$$\vec{B}_{nm} \equiv \vec{G}_n \otimes \vec{g}_m$$

$$(\vec{A}_i{}^j{}_k) \cdot (\underline{\underline{\vec{B}_{ik}}}) \equiv (\vec{g}_i \cdot \vec{G}_n) * \vec{g}^j * (\vec{G}_k \cdot \vec{g}_m)$$

B.11 Permutation Symbol

The permutation symbol is used in building determinants.

It is defined as (6, 85)

$$E^{ijk} = 1 \text{ for even permutation of } (i,j,k)$$
$$= -1 \text{ for odd permutation of } (i,j,k)$$
$$= 0 \text{ otherwise}$$

This definition is extended to more or fewer indices.

B.12 Volume Tensor

In some preferred basis $\vec{e}_i$ (usually, but not necessarily, one for which $\vec{e}_i \cdot \vec{e}_j = \delta_{ij}$), the volume tensor is defined as

$$\vec{V} = E^{ijkn} \vec{e}_i \otimes \vec{e}_j \otimes \vec{e}_k \otimes \vec{e}_n$$

Where E^{ijkn} is the permutation symbol.
Now the components in all other bases are defined by the rules of tensor transformation. In other than the preferred basis, the volume tensor components are written V^{ijkn} to avoid confusion with the permutation symbol E^{ijkn} (which are not the components of a tensor).

APPENDIX C: COORDINATE SYSTEMS

In discussing deformation, it is very important to accurately define the various coordinate systems used and their interrelationships.

C.1 General Coordinates in Terms of an Underlying Vector Space

All coordinate systems are defined in terms of an underlying real Euclidean vector space generated by an orthonormal basis $\vec{I}_i$. The points in some derived coordinate manifold X^i, may be associated (usually) in a one-to-one correspondence with the points described by the general position vector $\vec{P}$, in the underlying Euclidean vector space. If the position vector is $\vec{P} = z^i \vec{I}_i$, the correspondence may be symbolized

$$X^i \longleftrightarrow \vec{P} \equiv z^j \vec{I}_j$$

or, in terms of components of P

$$X^i = f^i \circ (z^j)$$

and inversely

$$z^i = F^i \circ (X^j)$$

The metric of the underlying vector space is δ_{ij}, i.e. $\vec{I}_i \cdot \vec{I}_j = \delta_{ij}$. The local metric of the X^i coordinates may be defined by the relation to the underlying space. A local vector space with basis $\vec{G}_j$ may be attached to every point X^i in the derived coordinates, by the following definition:

$$\vec{G}_j = \frac{dz^i}{dX^j} \vec{I}_i$$

From this, the local metric at X^i is defined as

$$G_{ij} = \vec{G}_i \cdot \vec{G}_j = \frac{dz^k}{dX^i} \frac{dz^m}{dX^j} \vec{I}_k \cdot \vec{I}_m$$

$$G_{ij} = \frac{dz^k}{dX^i} \frac{dz^k}{dX^j}$$

C.2 Coordinates Used in Deformation Theory

A geometrical point described by the tip of the position vector $\vec{P}$ of the underlying space may be specified by giving the components of $\vec{P}$. The components of $\vec{P}$ relative to the orthonormal basis $\vec{I}_i$ are z^i and can be thought of as coordinates. Other derived coordinates are ultimately defined relative to the z^i.

The two most important derived coordinate systems are the material coordinates and the spatial coordinates. The material coordinates are used to label the material points and usually do not change with time. The spatial coordinates are used to describe the position of each material point and usually do not change with time either. The exact geometrical state of deformation of a material body is described by the functional relation of each of its material points to spatial points. This defines the spatial positions of the material points of all items. In this report, the spatial coordinates are symbolized X^i, and the material coordinates are x^i.

For convenience in notation, time will be included with the spatial coordinates to make a four dimensional manifold. Time in the underlying space is represented by $z^4 \vec{I}_4$. The material and spatial coordinates are chosen at time zero and usually are not changed thereafter. The spatial coordinates may be defined by

$$\left.\begin{aligned} z^i &= S^i \circ (X^j) \\ \text{and inversely} \quad X^i &= s^i \circ (z^j) \end{aligned}\right\} \quad \text{for i and j} = 1 \rightarrow 3$$

$$\text{and} \quad X^4 = z^4$$

The material coordinates may be defined by

$$\left.\begin{aligned} z^i &= M^i \circ (x^j) \\ \text{and inversely} \quad x^i &= m^i \circ (z^j) \end{aligned}\right\} \quad \text{for i and j} = 1 \rightarrow 3$$

$$\text{and} \quad x^4 = z^4$$

These definitions are usually made so that at time = $z^4 = 0$ the $x^i = X^i$ numerically..

The deformation of a material is described by the relation of the x^i to the X^i at later times.

$$\left.\begin{aligned} X^i &= F^i \bullet (x^j) \\ \text{and inversely} \quad x^i &= f^i \circ (X^j) \end{aligned}\right\} \begin{cases} j = 1 \quad 4 \\ i = 1 \quad 3 \end{cases}$$

$$\text{and} \quad X^4 = x^4 = z^4$$

APPENDIX D: COVARIANT DIFFERENTIATION

We shall define covariant or absolute differentiation of a tensor with respect to some path S as the ordinary differentiation of the tensor along the path when both (tensor and path) are expressed in the underlying coordinate space $z^i \vec{I}_i$. Absolute differentiation is indicated in vector form independent of coordinates. For example, the derivative of the second order tensor $\vec{T}$ with respect to the displacement vector $\vec{dP}$ is written $\vec{dT}/\vec{dP}$. Since the tensor and path are usually described in some other coordinates, formulae must be derived for covariant differentiation with respect to arbitrary metrics.

To properly derive these formulae, the tensor product of two vector spaces should be reviewed (5,29). The tensor basis $\vec{G}_{IK}$ derived from an arbitrary vector basis $\vec{G}_I$ is $\vec{G}_{IK} = \vec{G}_I \otimes \vec{G}_K$ where $\otimes$ indicates the tensor product.* Just as all vectors in the vector space may be referred to $\vec{G}_K$, all second order tensors in the vector space may be referred to $\vec{G}_{IK}$. The covariant derivative is a tensor of one higher order than $\vec{T}$.

In general curvilinear coordinates given by

$$z^I = z^I (x^k)$$

or

$$x^k = x^k (z^I)$$

---

* The properties of the tensor product are almost the same as the dot product. $\vec{X} \otimes (\vec{Y} + \vec{Z}) = \vec{X} \otimes \vec{Y} + \vec{X} \otimes \vec{Z}$ and $b\vec{X} \otimes \vec{Y} = \vec{X} \otimes b\vec{Y} = b(\vec{X} \otimes \vec{Y})$ and $\vec{X} \otimes (\vec{Y} \otimes \vec{Z}) = (\vec{X} \otimes \vec{Y}) \otimes \vec{Z}$. However, in general $\vec{X} \otimes \vec{Y} \neq \vec{Y} \otimes \vec{X}$

The second order tensor $\vec{\vec{T}}$ has the representation

$$\vec{\vec{T}} = t^{ij} \vec{g}_{ij}$$

and $\vec{dP}$ becomes $dx^i \vec{g}_i$

where $\vec{g}_{ij}$ is the new local tensor basis.

Covariant differentiation with respect to particular coordinates is indicated by a semicolon. Covariant differentiation not referred to a particular basis is indicated by .

$$\vec{\nabla} \vec{\vec{T}} = \frac{d\vec{\vec{T}}}{d\vec{P}} = \frac{d}{d\vec{P}} \left[t^{ij} \vec{g}_{ij} \right]$$

$$\vec{\nabla} \vec{\vec{T}} = \frac{d}{dx^i} \left[t^{ij} \vec{g}_{ij} \right] \otimes \vec{g}_k = t^{ij}{}_{;k} \vec{g}_{ijk}$$

where $\vec{g}_{ijk} = \vec{g}_i \otimes \vec{g}_j \otimes \vec{g}_k$

The $\vec{g}_{ij}$ are now functions of the coordinates and must be differentiated along with the tensor components.

$$\frac{d}{dx^k} \left[t^{ij} g_{ij} \right] \otimes \vec{g}_k = \left[\frac{dt^{ij}}{dx^k} + \frac{d\vec{g}_{ij}}{dx^k} \right] \otimes g_k$$

$$\frac{d}{dx^k} \left[t^{ij} g_{ij} \right] \otimes \vec{g}_k = \left[\frac{dt^{ij}}{dx^k} \vec{g}_{ij} + t^{ij} \frac{d\vec{g}_{ij}}{dx^k} \right] \otimes \vec{g}_k$$

where

$$\frac{d\vec{g}_{ij}}{dx^k} = \frac{d}{dx^k} \left[\vec{g}_i \otimes \vec{g}_j \right]$$

$$\frac{d\vec{g}_{ij}}{dx^k} = \frac{d\vec{g}_i}{dx^k} \otimes \vec{g}_j + \vec{g}_i \otimes \frac{dg_j}{dx^k}$$

Now $\frac{d\vec{g}_i}{dx^k}$ must be found.

$$\vec{g}_i = \frac{dz^I}{dx^i}\,\vec{I}_I \equiv z^I{}_{,i}\,\vec{I}_I$$

and

$$\vec{I}_I = \frac{dx^i}{dz^I}\,\vec{g}_i \equiv x^n{}_{,I}\,\vec{g}_n$$

Therefore

$$\frac{d\vec{g}_i}{dx^k} = \frac{d^2 z^I}{dx^k\,dx^i}\,\vec{I}_I$$

$$\frac{d\vec{g}_i}{dx^k} = \left(\frac{d^2 z^I}{dx^k\,dx^i}\right)\frac{dx^n}{dz^I}\,g_n \equiv \begin{Bmatrix} n \\ k\ \ i \end{Bmatrix}\vec{g}_n$$

The Christoffel symbols of the second kind are defined and symbolized as follows:

$$\begin{Bmatrix} n \\ k\ \ i \end{Bmatrix} = \left(\frac{d^2 z^I}{dx^k\,dx^i}\right)\frac{dx^n}{dz^I}$$

Using this notation, the covariant differentiation becomes much more compact.

$$\frac{d\vec{g}_{ij}}{dx^k} = \begin{Bmatrix} n \\ k\ \ i \end{Bmatrix}\vec{g}_n \otimes \vec{g}_j + \begin{Bmatrix} n \\ k\ \ j \end{Bmatrix}\vec{g}_i \otimes \vec{g}_n$$

Substituting we obtain

$$\frac{d}{dx^k}\left[t^{ij}\,\vec{g}_{ij}\right] \otimes \vec{g}_k = \left[t^{ij}{}_{,k}\,\vec{g}_{ij} + t^{ij}\begin{Bmatrix} n \\ k\ \ i \end{Bmatrix}\vec{g}_{nj} + t^{ij}\begin{Bmatrix} n \\ k\ \ j \end{Bmatrix}\vec{g}_{in}\right] \otimes \vec{g}_k$$

$$\overrightarrow{\nabla T} = t^{ij}{}_{,k}\,\vec{g}_{ijk} = t^{ij}{}_{;k}\,\vec{g}_{ijk} + \left\{ {i \atop k\ n} \right\} t^{nj}\,\vec{g}_{ijk} + \left\{ {j \atop k\ n} \right\} t^{in}\,\vec{g}_{ijk}$$

and finally, $$\overrightarrow{\nabla T} = \left(t^{ij}{}_{,k} + \left\{ {i \atop k\ n} \right\} t^{nj} + \left\{ {j \atop k\ n} \right\} t^{in} \right) \vec{g}_{ijk}$$

APPENDIX E: A NUMERICAL METHOD FOR THE SOLUTION OF SOME PARTIAL DIFFERENTIAL EQUATIONS

E.1 Introduction

The purpose of this section is to present a numerical procedure for solving finite difference approximations of some systems of nonlinear partial differential equations.

To illustrate the scheme, we shall discuss an example involving a two-dimensional, rectangular, finite difference mesh. Several variables are tabulated at each of the mesh points. At every mesh point there is defined one difference equation for each dependent variable (at that mesh point).

The exact form of the difference equations will depend on the original differential equations, the boundary conditions, and the type of difference approximations used.

This method requires that the system of difference equations have an exact solution with some specific properties. This poses no difficulty in most physically oriented problems.

A special scalar parameter k, is introduced in the differential, and hence the difference equations. The difference equations are then written in homogeneous form $f_m = 0$, so that a point residual R_m may be defined as the sum of the squares of the difference functions at the point. The index m enumerates all of the mesh points. A system residual S is defined as the sum of all the equation residuals. Since the system residual is necessarily positive, the solution of the system may be reached by minimizing S as a function of all the dependent variables throughout the mesh. Because the difference equations are loosely connected, minimization using a variation of Newton's method in many variables is computationally feasible. Stability is not a problem with this technique, but in complicated, highly nonlinear problems, computational time and memory requirements may become excessive.

We have developed a computer code (IBM-7040/FORTRAN IV) for the solution of a formidable set of equations describing a two-dimensional high velocity impact of elasto-plastic materials. Our numerical experience with this problem will be discussed later.

E.2 Notation and Paramenterization of the Equations

The original system of differential equations and boundary conditions must be rewritten to include a special scalar parameter, k. At some value of the parameter, the equations must be identical with the original equations. At another value of the parameter, the equations must degenerate to a form with a known solution. Also, at every intermediate value of the parameter, say k = c, the corresponding solution W_c and the solutions W_k for neighboring values of k must be such that

$$\lim_{k \to c} (W_k) = W_c$$

As a very simple example, consider Poisson's equation in two independent variables, x and y.

$$\nabla^2 \circ V = g \circ (x, y)$$

and

$$V = h \circ \left[x \circ (s), y \circ (s) \right] = h \circ (s) \text{ over the boundary } s.$$

Possible choices for the parameterized equations are

$$\nabla^2 \circ V = K * g \circ (x,y)$$

and

$$V = k * h \circ (s)$$

Clearly there is a known solution for k = 0, viz. V = 0, and the desired equations are duplicated when k = 1. From physical considerations it is plausible that solutions exist for all $0 \leqslant k \leqslant 1$. When the differential equations are converted to the difference approximations, k will appear in a similar role in the difference equations.

$\nabla^2 \circ V = k * g \circ (x,y)$ might be approximated at internal mesh points by

$$0 = -k * g \circ (X_{i,j}\, y_{i,j}) + \frac{V_{i+1,j} - 2 * V_{i,j} + V_{i-1,j}}{X^2} + \frac{V_{i,j+1} - 2 * V_{i,j} + V_{i,j-1}}{Y^2}$$

and $V = k * h \circ (s)$ at boundary points (for simplicity we are not considering curved boundaries) would simply become

$$0 = V - k * h \circ \left[x(s),\ y(s)\right]$$

At each of m times n mesh points, there are two associated independent variables (coordinates x and y of the mesh point), and the dependent variable V. For bookkeeping purposes, a control number is also listed at each mesh point. For example, within the region covered by the mesh, there may be boundary points, internal or external points, and changes in the governing equations. Therefore, in general, the difference equations will not be identical at all the mesh points.

Further discussion requires some notational definitions. Often there is more than one dependent variable and necessarily the same number of difference equations at each mesh point. The equations associated with mesh point $P_{i,j}$ are symbolized $f^p{}_{i,j} = 0$. The dependent variables tabulated at $P_{i,j}$ are written $V_{i,j,p}$. The indices i and j refer to the mesh point. The index p lists the equations and corresponding dependent variables at $P_{i,j}$. The independent variables are written as $W_{i,j}$.

The equations at $P_{i,j}$ usually will contain variables listed at $P_{i,j}$ and only a few neighboring points. Therefore, $f^p{}_{i,j} = 0$ is a loosely connected system of equations.

The set of all the $V_{i,j,p}$ and $W_{i,j}$ will be relabeled Z_m and X_r respectively. The homogeneous difference equations may now be written

$$f^p{}_{i,j} \circ (k, Z_m, X_r) = 0$$

to show the functional dependence. Note that each $f^p{}_{i,j}$ usually depends on only a few of the Z_m and X_r. If the numerical values of the Z_m are chosen

properly, they will simultaneously satisfy all the $f^p_{i,j} = 0$. This is an exact solution to the system for the parameter value k, and will be written $\bar{Z}_m(k)$. A set of Z_m which is not an exact solution is a trial solution, and will simply be written $Z_m(k)$.

E.3 The Convergence Process

Let a known solution $\bar{Z}_m(k)$ for $k = A$ be tabulated throughout the mesh. The solution for $k = B$ is desired. The range of k is divided into q equal (for simplicity) parts, generating a sequence of $q + 1$ values of k over the interval A to B. Denote this sequence by k_q. In a time dependent problem the parameter enters naturally as time, so that k = time.

The convergence process uses the solution $\bar{Z}_m(k_q)$ to proceed toward the solution $\bar{Z}_m(k_{q+1})$. Starting with $k = A$, the process is repeated (as $k \longrightarrow B$) so that it converges to the final solution $\bar{Z}_m$, for $k = B$.

At this time the equation, point, and system residuals (or errors) need to be defined. The equation residual $E^p_{i,j}$ for equation $f^p_{i,j}(k, Z_m) = 0$ is simply

$$E^p_{i,j}(k, Z_m) = f^p_{i,j}(k, Z_m)$$

The point residual is the sum of the squares of the equation residuals at the point.

$$R_{i,j}(k, Z_m) = \sum_p (E^p_{i,j})^2$$

The system residual is the sum of all the point residuals.

$$S(k, Z_m) = \sum_{i,j} R_{i,j}$$

For a given k, the system residual $S(k, Z_m)$ may be interpreted as a surface above an m dimensional hyperplane. A point on the hyperplane represents a possible choice of values of the set of independent mesh

variables Z_m. The height of the surface above a point in the plane is the system residual for the mesh variable configuration represented by that point. A point Z_m, where S = 0 is clearly a solution to the system.

E.4 Algorithm

The algorithm for getting from the solution $\bar{Z}_m(k_n)$ for k_n to the solution $\bar{Z}_m(k_{n+1})$ for k_{n+1} is now described. Since the solution for k_{n-1} is available (except at $k_n = A$), a likely prediction $\bar{Z}_m(k_{n+1})$ for the solution $\bar{Z}_m(k_{n+1})$ is

$$\bar{Z}_m(k_{n+1}) \equiv Z_m(k_{n+1}) \equiv \frac{Z_m(k_n) - Z_m(k_{n-1})}{k_n - k_{n-1}} * (k_{n+1} - k_n) + Z_m(k_n)$$

Usually the increment in k is uniform so that the prediction is simply

$$\bar{Z}_m(k_{n+1}) \equiv 2\,\bar{Z}_m(k_n) - \bar{Z}_m(k_{n-1})$$

More elaborate predictors may be built using more of the earlier solutions or some other means peculiar to the particular problem.

The prediction generally will be in error to an extent requiring corrections at many mesh points. The corrector process starts by evaluating the derivatives of each point error $R_{i,j}(k_{n+1})$ with respect to the dependent variables $V_{i,j,p}$ tabulated at point $P_{i,j}$. The result is an array of partial derivatives $D_{i,j,p}$

$$D_{i,j,p} = \frac{d\,R_{i,j}}{d\,V_{i,j,p}}$$

The first correction is written $C_{i,j,p}$ and is added to the guess or prediction. The corrected trial solution is then

$$\bar{Z}_m(k_{n+1}) = Z_m(k_{n+1}) + C_{i,j,p}$$

or in other notation

$$V^{*}_{i,j,p} = V_{i,j,p} + C_{i,j,p}$$

The correction array $C_{i,j,p}$ is given by

$$C_{i,j,p} = -L * \frac{D_{i,j,p} * R_{i,j}(k_{n+1})}{\sum_{p} (D_{i,j,p})^2}$$

where

$$0 < L \leqslant 1$$

Essentially, the p partials at a point determine a "gradient" direction in which the error changes the fastest. This calculation assumes that the interaction with the surrounding points is less than the influence of the point on its own error.

The correction at each point is made in the negative of the "gradient" direction. The magnitude of the point correction is the point error divided by the rate of change of the point error. Even though the errors at surrounding points are affected as each point is moved, this correction method does indeed converge for many systems.

L is introduced to prevent overshoot and to avoid making the errors bigger, leading to instability. This is important at the start of the correction cycle when the errors are relatively large. In a nonlinear problem, generally L should start around 0.1 and go to 1.0 as the errors diminish. See Figure 1.

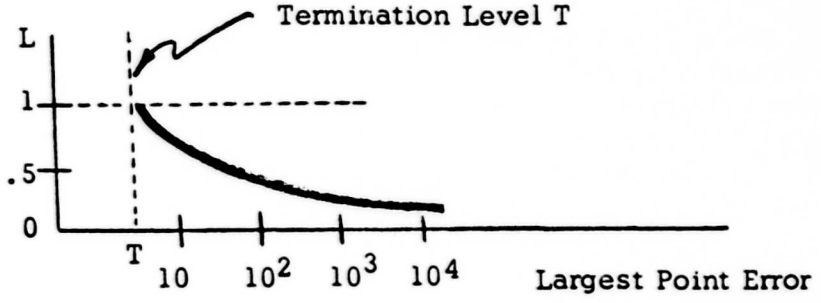

FIGURE 1

The value of L as a function of the largest point residual is determined mostly by experience with a given problem.

A corrector termination level, T, is set so that when the largest point error is less than T, the trial solution is considered sufficiently accurate and the computations for the next value of k are started.

The procedure is repeated until the solution Z_m for k = B is reached.

During the corrector procedure, many artificial devices can be used to vastly speed the convergence in particular problems. A great deal depends on the investigator's ingenuity and his intuitive feel for the behavior of the solution.

E.5 Computational Aspects

In implementing the algorithm on a digital machine, several aspects deserve attention.

The point errors will usually be reduced in some parts of the mesh faster than others and therefore will reach an acceptable value well before other parts. Much time can be saved if zeros are placed in the correction array wherever the point error is less than the cutoff level. They are called zero points for the moment. Then in the next corrector cycle no calculations are performed at zero points for which the neighbor points they depend on are also zero.

The elimination of calculations at zero points also avoids the round-off noise that soon arises and becomes evident at points requiring little correction.

For simple systems of equations, the derivatives may be evaluated by an analytic formula derived from the difference equations. In more complicated cases, it is usually easier and just as fast to take a finite difference. For one thing, this allows the alteration of the system equations without having to rederive the derivative formulas. We found this convenient in our program for elasto-plastic dynamics where the governing equations are exceedingly complicated.

In many physical problems, especially those in fields, stress analysis, etc., a reasonably good initial prediction can be made. For

example, Frocht's method of "Linear Rosettes" in linear static stress analysis is a fast computation and can provide a good start for a nonlinear system.

E.6 Convergence Theory

For simplicity, consider a one-dimensional mesh in which the point residual involves only the point and its two neighbors. The argument is easily generalized. The point residual at mesh point P_i is R_i and the dependent variable is U_i. The solution for $k = k_n$ is $\bar{Z}_m(k_n)$. Start with $\bar{Z}_m(k_n)$ as an approximation to the solution $\bar{Z}_m(k_{n+1})$. The assumed continuity of Z_m with respect to k implies that for sufficiently small $\Delta k = k_{n+1} - k_n$ the largest point error can be held to any desired level.

The correction to be applied at each point P_i is

$$C_i = \frac{-L * R_i}{\frac{dR_i}{dU_i}}$$

The change in the residual at point P_i for infinitesimal L is

$$\Delta R_i = C_{i-1} * \frac{dR_i}{dU_{i-1}} + C_i * \frac{dR_i}{dU_i} + C_{i+1} * \frac{dR_i}{dU_{i+1}}$$

$$\frac{\Delta R_i}{\Delta L} = -\left[R_{i-1} \frac{\frac{dR_i}{dU_{i-1}}}{\frac{dR_{i-1}}{dU_{i-1}}} + R_i + R_{i+1} \frac{\frac{dR_i}{dU_{i+1}}}{\frac{dR_{i+1}}{dU_{i+1}}} \right]$$

Clearly $\Delta R_i/\Delta L$ should be much less than zero for rapid convergence.

In general, $\Delta R_i/\Delta L$ can be written as a well behaved function of several variables. It is hoped that in the region of interest $\Delta R_i/\Delta L \ll 0$. For a particular set of equations, the determination of the region where $\Delta R_i/\Delta L$ is negative may be very complicated. Usually physical intuition

is sufficient to assess the probable convergence or divergence of the method. The iterations will probably converge if the equations are such that the point residual depends more strongly on the variables at that point than it does on the variables at the neighbor points. If a given system is of the variable space, etc. can be used to investigate the regions where $\Delta R_i/\Delta L$ is negative.

APPENDIX F: REFERENCES

1. Eringen, A. Cemal, "Nonlinear Theory of Continuous Media," McGraw-Hill Book Company, Inc., New York (1962).

2. Sokolnikoff, I. S., "Tensor Analysis," New York (1951).

3. Sokolnikoff, I. S., "Mathematical Theory of Elasticity," McGraw-Hill Book Company, Inc., New York (1956).

4. Houwink, R., "Elasticity, Plasticity and Structure of Matter," Dover Publications, Inc., New York (1958).

5. Lichnerowicz, A., "Elements of Tensor Calculus," John Wiley & Sons, Inc., New York (1963).

6. Wrede, Robert C., "Vector and Tensor Analysis," John Wiley & Sons, Inc., New York (1963).

7. Hodgman, Charles D., "Handbook of Chemistry and Physics," Chemical Rubber Publishing Co., Cleveland, Ohio (1940).

8. Riney, T. D., "Theoretical Hypervelocity Impact Calculations Using the Picwick Code," Air Proving Ground Center, Eglin Air Force Base, Florida (1963).

9. Wylie, C. R. Jr., "Advanced Engineering Mathematics," McGraw-Hill, Book Company, Inc., New York (1960).

10. Ralston, Anthony and Herbert S. Wilf, "Mathematical Methods for Digital Computers," John Wiley & Sons, Inc., New York (1962).

11. Coulson, C. A., "Waves," Interscience Publishers, Inc., New York (1962).

12. Thomas, Tracy Y., "Plastic Flow and Fracture in Solids," Academic Press, New York (1961).

13. Grinter, L. E., "Numerical Methods of Analysis in Engineering," MacMillan Company, New York (1949).

14. Hildebrand, F. B., "Introduction to Numerical Analysis," McGraw-Hill Book Company, Inc. (1956).

15. Webster, A. G., "Partial Differential Equations of Mathematical Physics," Dover Publications, Inc. (1955).

16. Thomas, Tracy Y., "Tensor Analysis and Differential Geometry," Academic Press, New York (1961).

17. Lapidus, Leon, "Digital Computation for Chemical Engineers," McGraw-Hill Book Company, Inc., New York (1962).

18. Freudenstein, Ferdinand and Bernard Roth, "Numerical Solution of Systems of Nonlinear Equations," Journal of the Association for Computing Machinery, Assoc. for Computing Machinery, (1963).

19. Brode, H. L. and R. L. Bjork, "Cratering From a Megaton Surface Burst," Proceedings of the Geophysical Laboratory, Lawrence Radiation Laboratory Cratering Symposium, Livermore, Calif. (1961).

20. Rajnak, S. and F. Hauser, "Plastic Wave Propagation in Rods," Symposium on Dynamic Behavior of Materials, ASTM Special Technical Publication No. 336, American Soc. for Testing and Materials, Philadelphia, Pa. (1962).

21. Harlow, Francis H., "Two-Dimensional Hydrodynamic Calculations," Los Alamos Scientific Laboratory, N.Mex. (1959).

22. Wilkins, Mark L. and Richard Giroux, "The Calculation of Stress Waves in Solids," Proceedings of the Sixth Symposium on Hypervelocity Impact (1963).

23. Kolsky, H., "Stress Waves in Solids," Dover Publications, Inc., New York (1963).

24. Daly, Bart J., "The Bounding of Instabilities of the PIC Difference Equations, Los Alamos Scientific Laboratory, N.Mex. (1962).

BALLISTIC PENETRATION OF ORGANIC FIBRE FELTS

by

Thomas W. Ipson and Rodney F. Recht

Denver Research Institute of the University of Denver

BLANK PAGE

CONTENTS

ABSTRACT

Organic, non-woven, felt materials offer a lightweight means for stopping blunt fragments. Providing the felt is not backed up and is permitted to bulge freely, it acts somewhat like an elastic-plastic bowstring, in reverse. The projectile is decelerated over a relatively long distance and, consequently, stresses are relatively low. Impulse is transmitted radially to the felt by shear waves, and the rate of change of momentum of the felt in the direction of projectile motion is equal, but opposite in sign, to that of the projectile. It is desired to quantitatively understand the force interaction between a projectile and a felt so as to establish equations of motion in terms of the pertinent static and dynamic properties of felt materials. As a background, this paper explains the development of analytical equations which describe the dynamics during penetration of ductile and brittle rigid targets, by sharp and blunt projectiles. Comparisons are drawn to illustrate the basic differences in the reaction of rigid and non-rigid target materials during ballistic perforation. An experimental program is described which has the objective of revealing the behavior of organic, non-woven, needled, fibre felts subjected to ballistic impact. Analytical models will identify the important material parameters and their roles in the penetration process. An approach to the analytical development is presented.

INTRODUCTION

Weight is an important consideration for all items which must be carried or moved from place to place. For this reason, armor for the protection of personnel or vehicle components is often evaluated on the basis of protection per unit weight. A projectile is stopped by applying to it an impulse, $\int F dt$, equal and opposite to its impact momentum. Expressed in other terms, a projectile is stopped when the work, $\int F dx$, done on and by the projectile, is equal to its initial kinetic energy. High strength, rigid, ductile armors, such as steel, produce high decelerating forces which defeat the projectile quickly through a relatively short distance. Low strength, non-rigid, ductile armors, such as organic fibre felts, produce much lower decelerating forces. However, these forces, acting through longer periods of time and greater distances, can induce the decelerating impulse and work necessary to defeat the projectile. In some lightweight armor applications, many felt materials offer excellent resistance to penetration by certain projectile types. These applications must include provision for allowing the felt to freely deform during projectile deceleration.

A full understanding of the force interaction between the felt and the projectile is desired so that felts can be designed to give maximum ballistic protection per unit weight. The resistance offered by the felt is a function of its properties. Influential properties must be identified and the way in which each of these properties influences the interaction force must be defined before the penetration process can be understood. The objective of this study is the development of analytical equations of motion which incorporate important material properties. The analytical model used to develop the equations of motion must be accurate. Consequently, experiment must alternate with theory during the development to confirm the validity of the model, or to provide the information and insight required to modify the model. Finally, a number of experiments are performed to confirm the range of validity of the equations developed using the model.

This type of approach has been successfully applied during studies of ballistic penetration involving rigid projectiles and rigid targets. Resulting analytical equations contain the important material parameters and, more important, show how each material property influences the force which resists penetration. What are the significant differences during penetration of rigid and non-rigid targets? This question can be answered best by first reviewing the mechanics of penetration related to rigid targets and then comparing the two problems.

This paper will consider, briefly, the ballistic penetration of rigid targets as a background against which to compare the penetration of non-rigid targets. Basic differences in the penetration processes will be discussed and the influence of wave mechanics will be emphasized. Experimental data which define the dynamics of projectile deceleration and the force interaction will be presented.

PENETRATION OF THICK, RIGID TARGETS BY SHARP, NON-DEFORMING PROJECTILES

The problem of penetration of thick, rigid targets was studied during the performance of a research contract for the Army Tank Automotive Center at Detroit Arsenal.[1*] Three major components of the force which resists motion of the projectile have been identified.

The plastic deformation of a ductile target material, which is displaced laterally, requires work by the projectile. Plastic deformation is a constant volume process which extends to a radius given closely by:

$$r_m = r\left[\frac{E}{\sigma_y}\sqrt{\frac{1}{1+\frac{2E}{\sigma_y}}}\right] = r\,Z_m \qquad (1)$$

where r_m is the radius enclosing plastically deformed target material

r is the radius of the hole left by the projectile

E is Young's Modulus

σ_y is tensile yield strength

Z_m is a symbol used to denote the function in brackets

Integrating the plastic deformation equation from r to r_m yields the following expression for the plastic work done while the projectile travels through a distance, dx:

$$\frac{dW}{dx} = 2\pi\tau_s\left(r_m\sqrt{r_m^2+r^2} - r_m^2 + r^2\,\ell n\,\frac{r_m+\sqrt{r_m^2+r^2}}{r}\right) \qquad (2)$$

where τ_s is dynamic shear strength

But, the plastic shear work, per unit distance traveled by the projectile, is the shear force component opposing motion. Further, for the materials under consideration, the first two terms in the parentheses nearly cancel and the shear force can be written in terms of Z_m as:

$$F_\tau = 2\pi\tau_s r^2\,\ell n\left(Z_m+\sqrt{Z_m^2+1}\right) \qquad (3)$$

* Superscripts refer to references in the Bibliography.

Thus, the force component due to plastic deformation has been defined in terms of the dynamic shear strength, Young's modulus, and the static tensile yield. It is independent of projectile shape. Its derivation is based upon the assumption that the material will yield plastically without brittle cracking.

Acceleration of mass produces another force component which acts upon the projectile. This force would be present even if the material had no shear strength. Its magnitude depends upon the mass which is being accelerated. Consider a frictionless, non-viscous, compressible fluid. The mass being accelerated depends, not only upon the density of the material, but also upon the volume being accelerated. The volume of accelerating mass is a function of compressibility. A highly compressible fluid will compress to accommodate the volume of the intruding projectile readily while a rigid material will not. Hence, compressive waves usually travel much slower in a compressible material than in a less compressible material of the same density. The pressure associated with the velocity at which the projectile surface moves against the fluid is given by:[2,3]

$$p = \rho C V = V\sqrt{K\rho} \qquad (4)$$

where p is pressure

ρ is mass density

C is wave velocity

V is velocity normal to the interface

K is bulk modulus

Thus, for a conical, rigid projectile moving through a frictionless, non-viscous fluid, the force opposing motion is given by:

$$F_i = \pi r^2 \sqrt{K\rho} \quad V \sin \phi \qquad (5)$$

Equation (5) represents the inertial force opposing motion of a conical projectile having a half-angle, ϕ, and is, therefore, the inertial force component acting during penetration of such a projectile into a thick, ductile target.

Finally, the third identified component results from frictional resistance at the sliding interface between the projectile and target material. Pressures arising from the shear and inertial components act on the surface of the cone. The friction force is related to the

normal pressure by the coefficient of sliding friction. This coefficient is variable depending upon pressure, sliding velocity, and temperature. Under the conditions prevailing during ballistic penetration, values of the coefficient are probably typified by 0.2.[4] Taking into account the conical geometry leads to an expression for the frictional component in terms of the inertial and shear components.

$$F_f = \frac{f}{\tan \phi} \quad (F_i + F_s) \tag{6}$$

Direct summation of all three components leads to an expression for the total force-resisting motion of the projectile.

Figure 1 shows velocity-penetration curves for several materials which were computed using the equation of motion derived by setting the total resisting force equal to the mass of the projectile times the deceleration. The projectile was given the same weight and caliber as the standard 0.50 caliber armor-piercing projectile (APM-2). The conical half-angle was chosen based upon considerations of the ogive dimensions of the standard round.[1] The penetration into steel checks quite reasonably when compared to Army Ballistic Limit data for the armor-piercing round.[5]

Note that the glasses appear to be nearly as good as steel. This occurs due to the assumption of ductile behavior. Cracks form in brittle materials in much the same manner as they form in ice under attack by an ice pick. These cracks may proceed at velocities approaching the shear wave velocity in the materials. The result of crack formation in glass is illustrated in Figure 2. A 4-inch, cubical glass block has been impacted normal to one surface at the center. Penetration proceeds as if the material were ductile until cracks grow to significant size. The material on either side of a crack is then just pushed aside by the projectile and shear deformation stops. Finally cracks grow faster than the projectile can fill them and the projectile enjoys free flight at a residual of about 830 feet per second.

Crack growth rate depends upon the type and magnitude of waves reflected from lateral boundaries. By confining a glass block in steel, the ballistic performance can be improved significantly. Figure 3 compares the ballistic resistance offered by unconfined and laterally confined glass blocks. Specific information concerning the projectile and block geometry is classified Confidential.

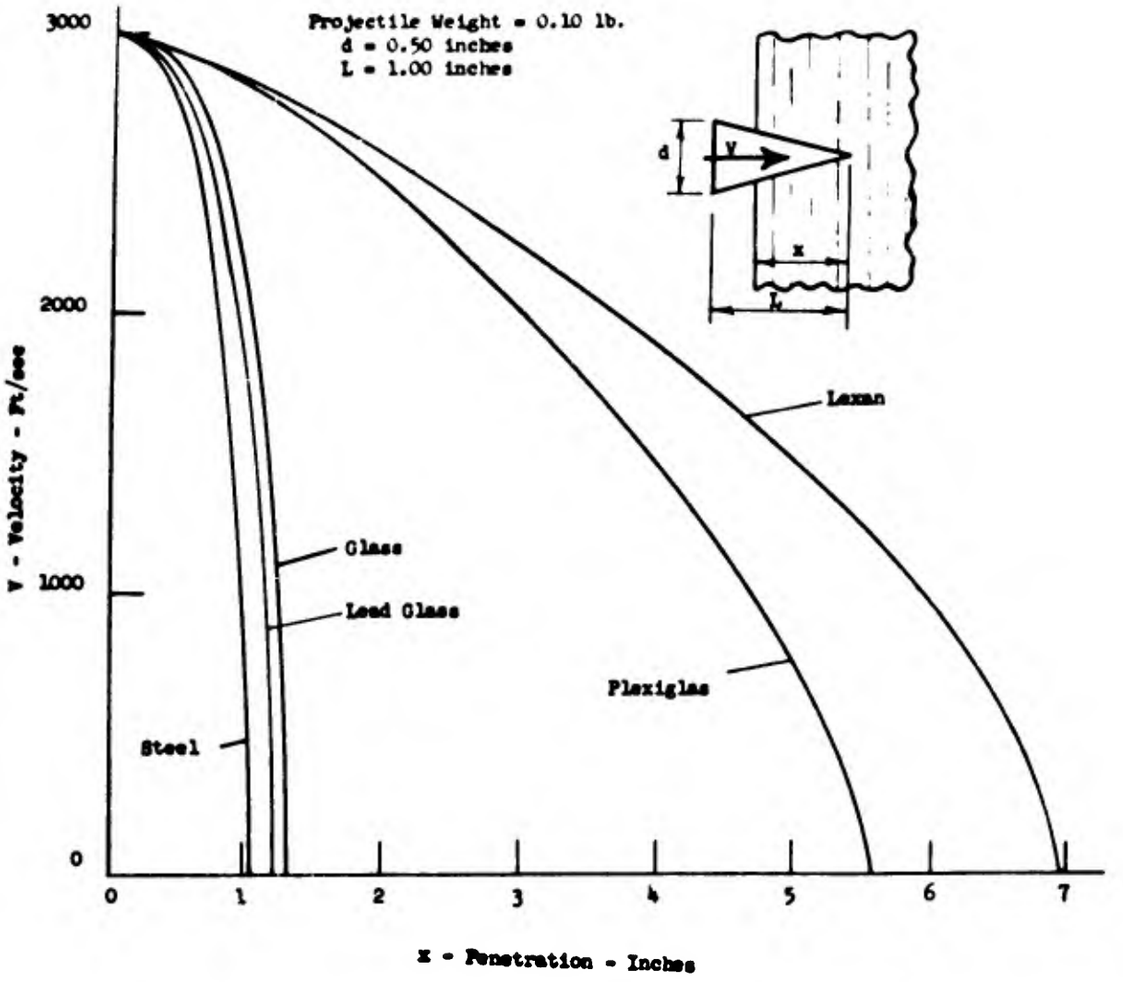

Figure 1. Computed Velocity-Penetration Curves for a Conical Projectile Assuming Ductile Behavior of Target Materials.

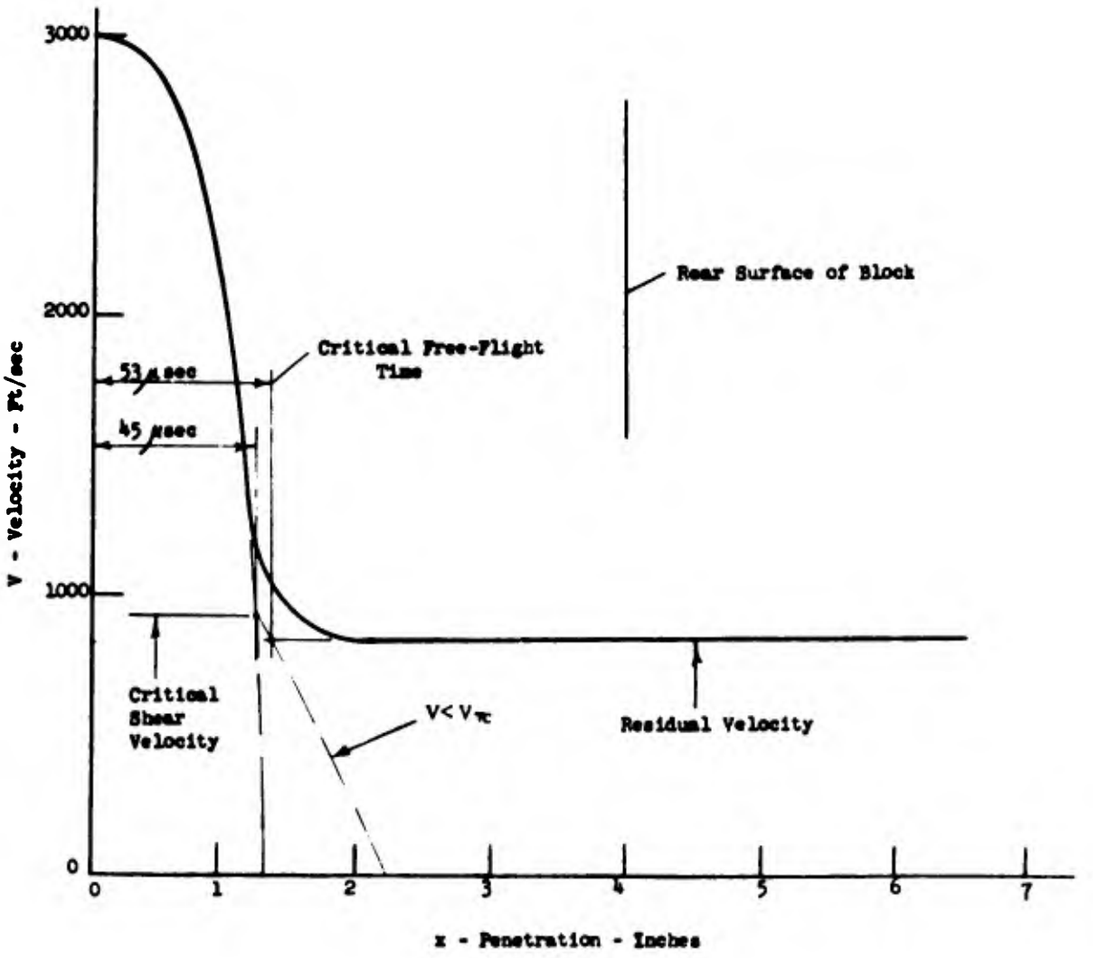

Figure 2. Effects of Brittle Radial Cracking on the Velocity-Penetration Curve for Glass.

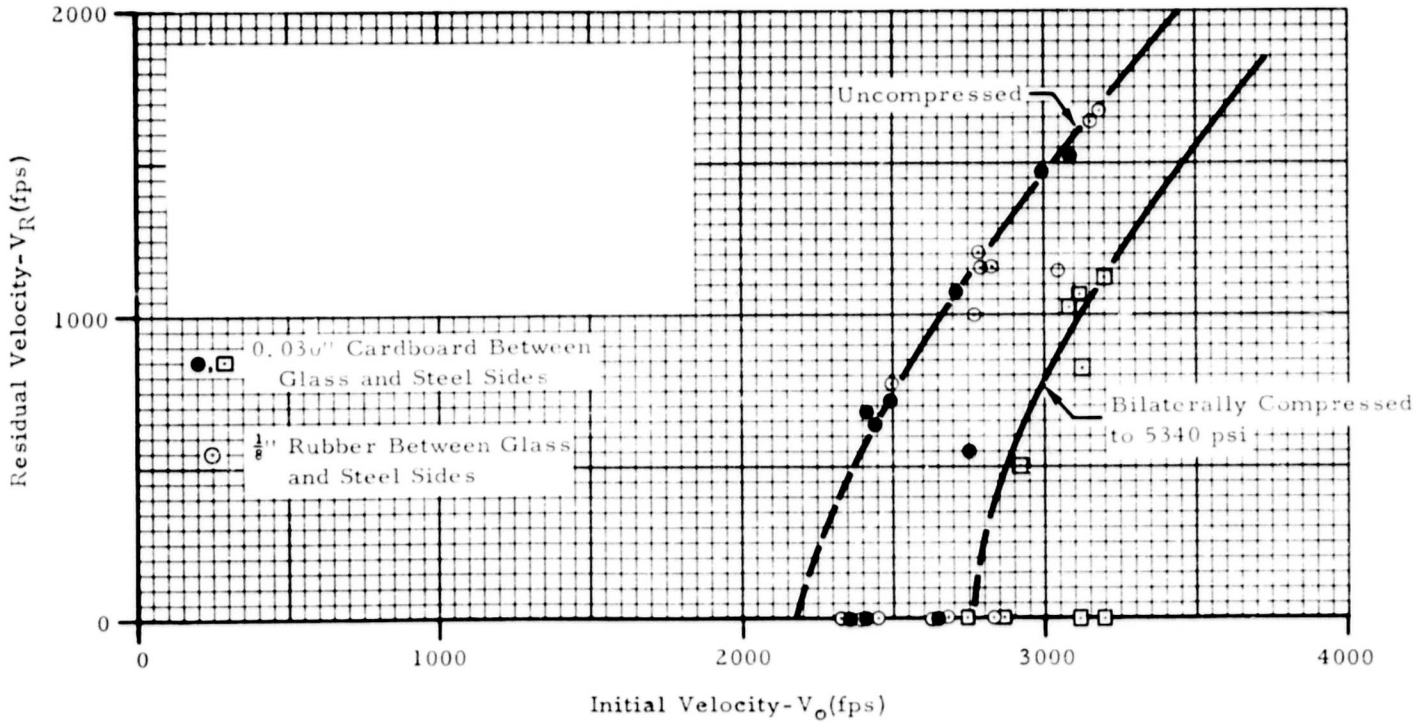

Figure 3. Ballistic Resistance Comparison of Glass Blocks With and Without Lateral Confinement.

PERFORATION OF RIGID, DUCTILE TARGETS BY HARD, BLUNT PROJECTILES

Post-impact remnants were used to mock-up the perforation shown in section on Figure 4. The rigid, ductile plate of homogeneous steel armor was impacted by a cylindrical steel fragment (Watertown Arsenal Laboratory 825-grain simulator). During initial impact, pressures approach Hugoniot pressures computed from equation (4) where V is one-half the impact velocity. For a steel-steel impact at 2, 000 feet per second, the pressure is about 2, 000, 000 p. s. i. Elastic and plastic waves travel each way from the interface, accelerating the plate plug and decelerating the projectile. The perforation is diagrammed in Figure 5. Simple wave mechanics will show that this acceleration-deceleration process takes place while the impact interface moves no more than $\frac{V}{C}$ T where V, C, and T are impact velocity, wave velocity, and plate thickness. Consequently, this process is completed very early during perforations at nominal impact velocities. Shear stresses set up at the impact interface periphery may exceed dynamic shear strength. If the sliding velocity between the plug and the plate, external to the shear area, reaches about 25 feet per second, an "adiabatic" shear zone will appear and the plug will shear out deforming the plate very little.[6,7] This second stage of perforation involves the work done in shear at the plug periphery. If the plate is thick (i. e., the thickness considerably exceeds half the length or diameter of the projectile), the shear stresses initially set up at the periphery may not be sufficient to overcome shear strength. Material will then be extruded laterally so as to form a crater. In a thick aluminum target, as the crater deepens the peripheral shear area decreases and an adiabatic shear zone may be created. In such a case, cratering ceases and a plug, thinner than the plate thickness, is ejected.

To compare this type of penetration with that accomplished by a sharp projectile, it will be helpful to identify equivalent force components. The inertial or wave component is associated with the acceleration of the plug material. This component produces severe pressures at the impact interface which, subsequently, create plastic flow of the projectile and target materials so as to render the impact highly inelastic. This component would be present even if the plate plug was completely detached from the plate prior to impact. The shear force acting to decelerate the projectile-plate plug mass, after the initial acceleration of the plug, causes increased pressure at the impact interface as well. Thus, the plastic shear work accomplished by this component

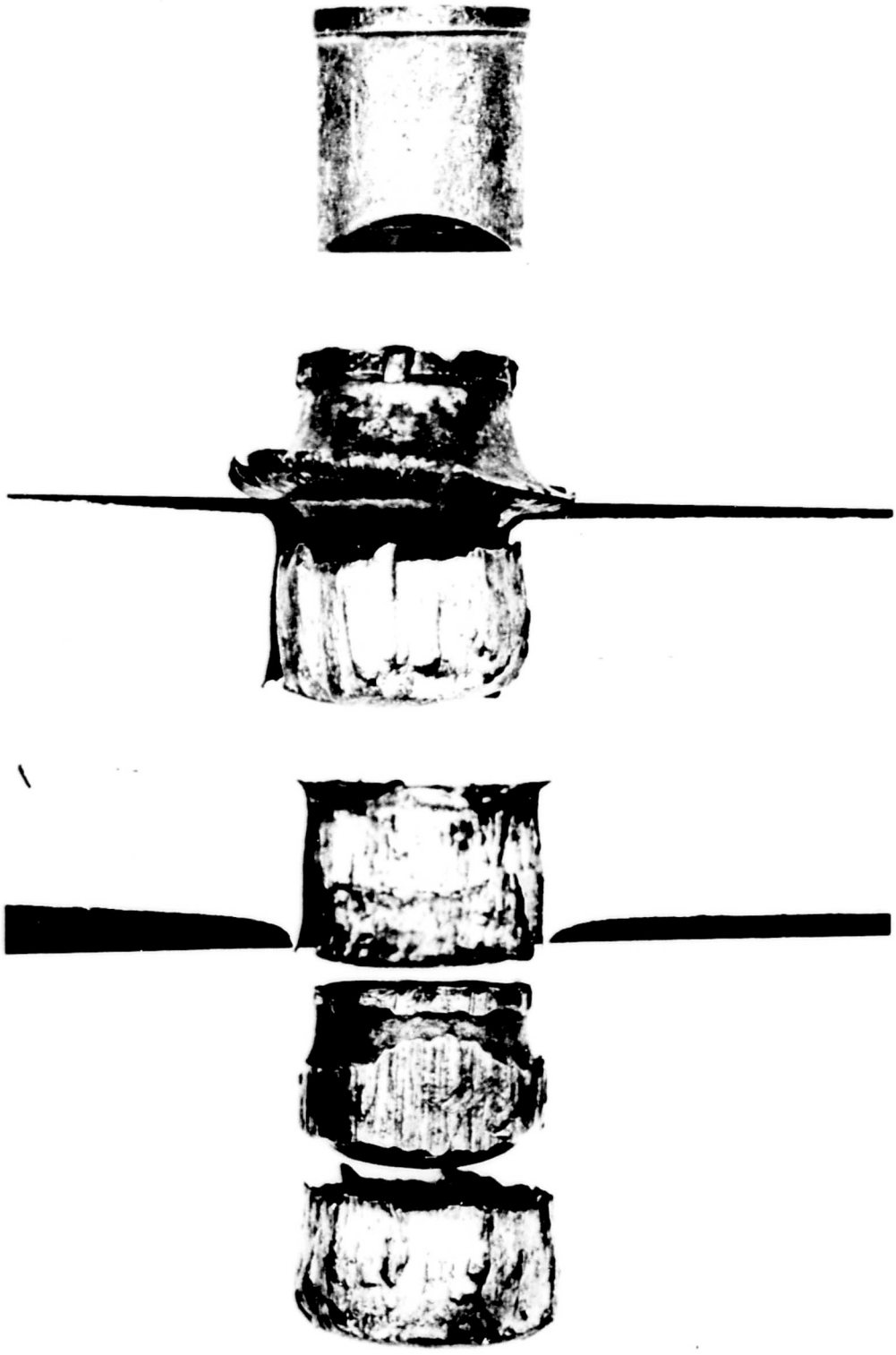

Figure 4. Blunt Fragment Perforation of a Rigid Ductile Plate.

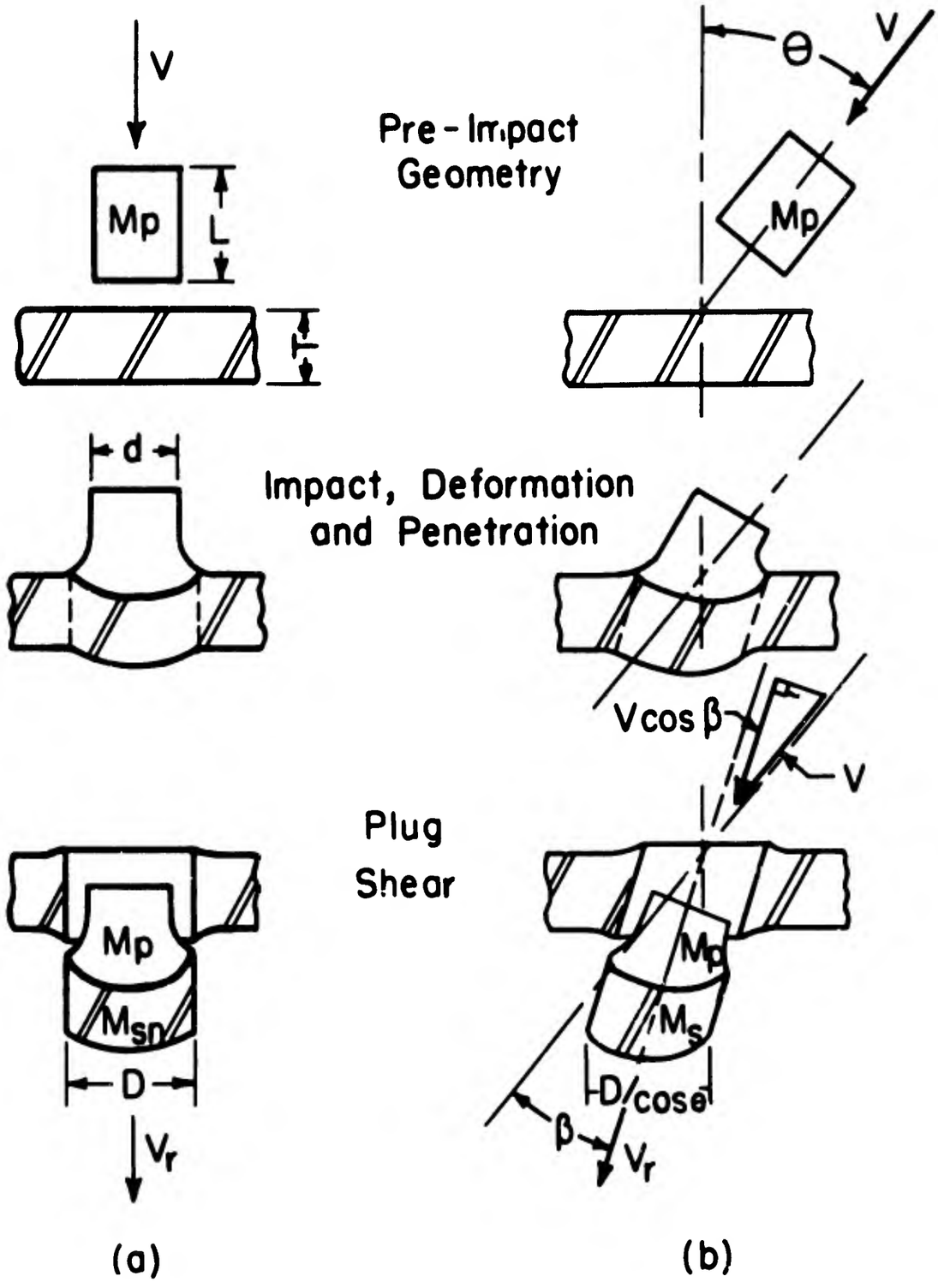

Figure 5. Characteristic Perforation of Thin Rigid Ductile Plates by Hard Blunt Fragments.

occurs in two places. Friction at the projectile periphery is probably quite low and has been neglected in analyses. The authors have derived residual velocity and ballistic limit relationships, using this model, which may be found in the published reference.[8] Figures 6 and 7 show the degree of correlation between residual velocity data and the following analytically derived equation:

$$V_r = \frac{M_p}{M_p + M_{sn}} \sqrt{V^2 - V_{xn}^2} \qquad (7)$$

Figure 6 concerns a thin, mild steel target impacted by a cylindrical steel fragment. Figure 7 concerns a thick aluminum target impacted by the same projectile. In the latter case, the form of the equation is modified somewhat to account for the difference between initial and ejected plate-plug mass; the modified form is derived in the reference. In equation (7) above, the following nomenclature is used:

V = initial (impact) velocity, fps
V_r = residual (post perforation) velocity, fps
V_{xn} = minimum perforation velocity; normal impact, fps
M_p = projectile or fragment mass, slugs
M_{sn} = ejected plate plug mass at normal obliquity, slugs

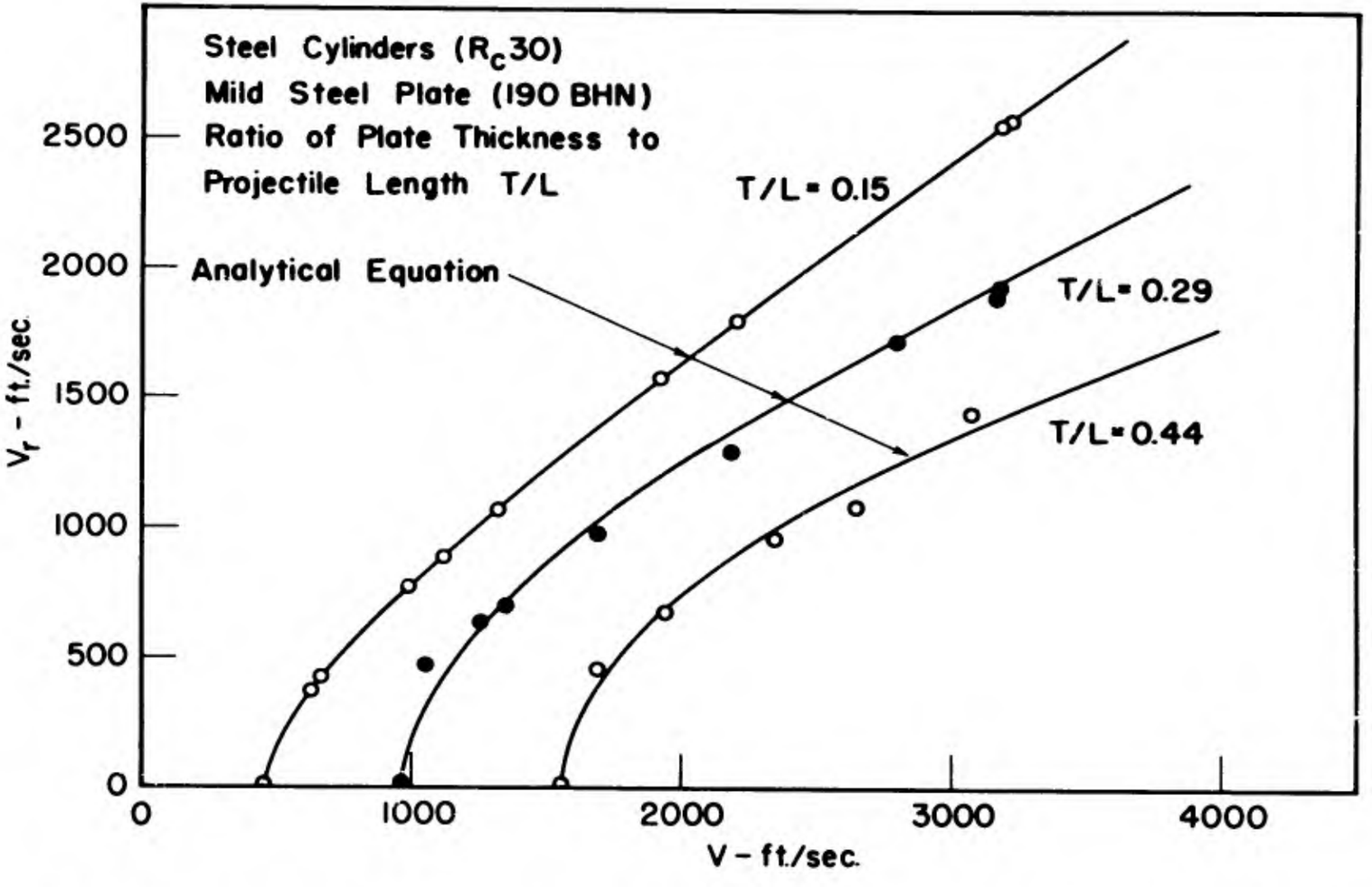

Figure 6. Post Perforation Velocity of Cylindrical Fragments. Normal Impact With Relatively Thin Rigid Ductile Plates.

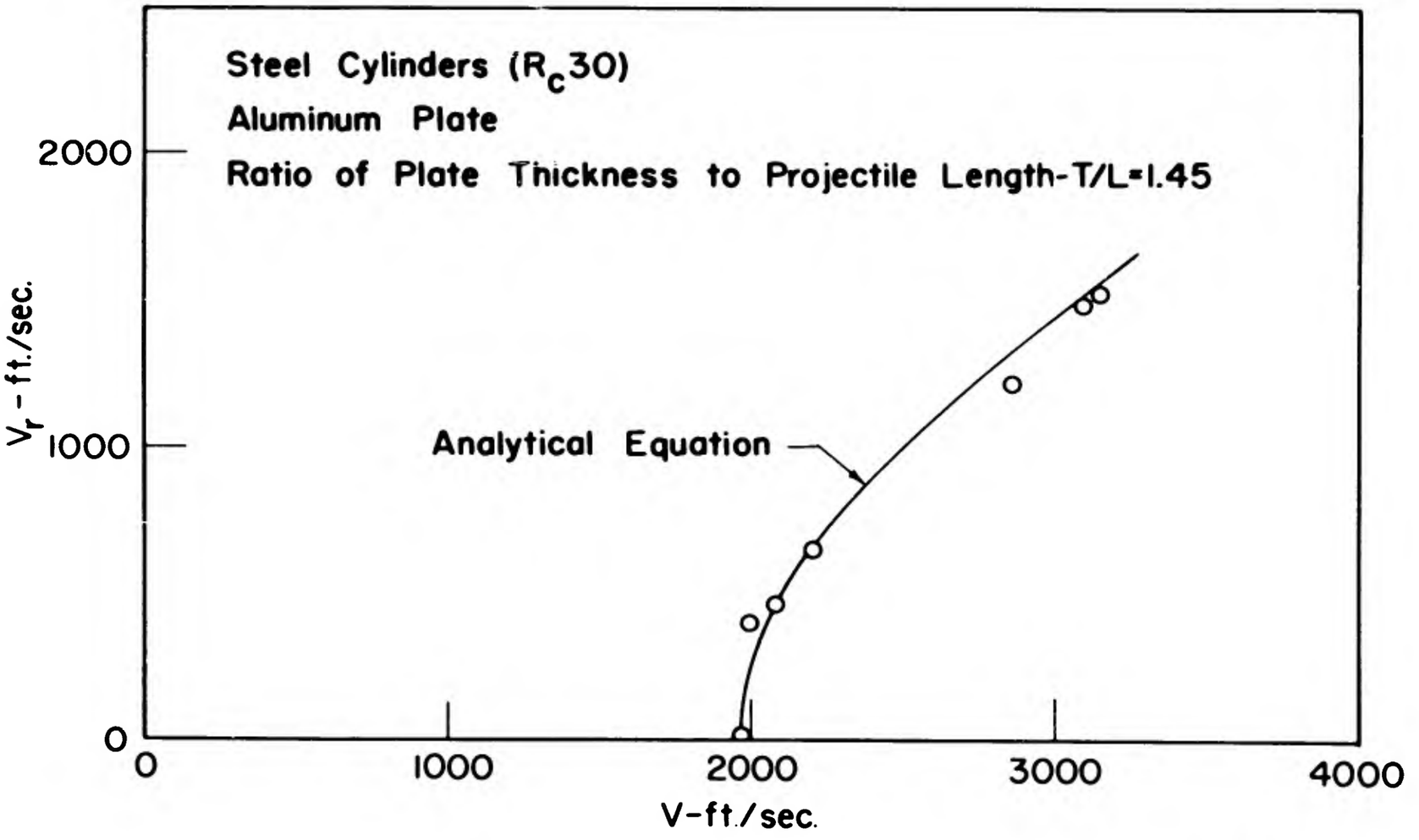

Figure 7. Post Perforation Velocity of Cylindrical Fragments. Normal Impact With Relatively Thick Rigid Ductile Plates.

PENETRATION OF NON-RIGID, DUCTILE TARGETS BY HARD, BLUNT PROJECTILES

Below a certain critical velocity, hard, blunt fragments cannot produce catastrophic shear failure in lightweight, non-rigid, ductile materials at the impact periphery. Instead, shear waves propagate laterally into the material inducing particle velocities in the direction of projectile motion. These shear waves also act to set up longitudinal waves which place the material in radial tension. A cone of material is formed which decelerates the projectile, much like a safety net decelerates a falling acrobat. The lightweight material accelerates rapidly and impact interface pressures are relatively low (typically 10,000 p.s.i.). This type of impact is illustrated in Figures 8 and 9 which show the cone formation in a nylon, non-woven, needled felt, initially 0.4-inch thick (56 ounces per square yard). The initial velocity was about 900 feet per second and the frames show the conditions at 125 and 250 microseconds, respectively. The projectile was completely decelerated in about one millisecond. A complete penetration is shown in Figure 10 at 150 microseconds after impact; initial velocity was about 1400 feet per second. The felt of Figure 11 was about half as thick. The projectile impacted the felt at 765 feet per second, which was very close to the ballistic limit velocity. It is shown 85 microseconds after impact.

To compare this type of penetration with that associated with rigid targets, consider the force components again. The total force which acts to decelerate the projectile is equal to the rate of change of momentum of the target material in the direction of projectile motion. Shear waves produce particle velocities in the direction of motion. Inertia and shear strength will contribute resistance to changes in particle velocity. Once stresses reach the shear yield strength, plastic shear waves will propagate producing plastic deformation in the materials. Tensile stresses in the cone wall will produce slip between fibres, and friction energy will be dissipated. Obviously, separation of individual force components is somewhat more complex during analysis of the penetration process associated with highly deformable felt materials.

Single strands of yarn have been used to study the one-dimensional problem.[9] The single strand is accelerated with little effect on projectile velocity. In this case, shear waves attenuate slowly and, since the projectile maintains an essentially constant velocity, particle velocities at a given radius in the direction of projectile

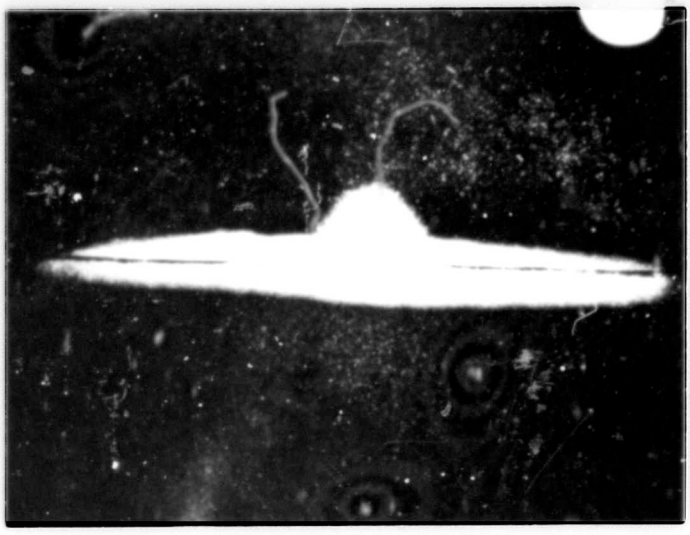

Figure 8. Response of Non-woven Nylon Felt to Ballistic Impact. 125 Microseconds After Impact by 17-Grain Fragment Simulator. Initial Velocity About 900 Feet per Second. Felt - 56 Ounces per Square Yard.

Figure 9. Response of Non-woven Nylon Felt to Ballistic Impact. 250 Microseconds After Impact by 17-Grain Fragment Simulator. Initial Velocity About 900 Feet per Second. Felt - 56 Ounces per Square Yard.

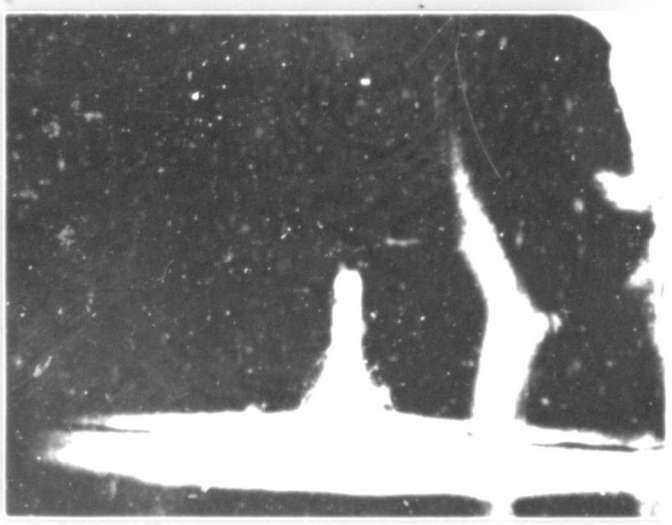

Figure 10. Response of Non-woven Nylon Felt to Ballistic Impact. 150 Microseconds After Impact by 17-Grain Fragment Simulator. Initial Velocity About 1400 Feet per Second. Felt - 56 Ounces per Square Yard.

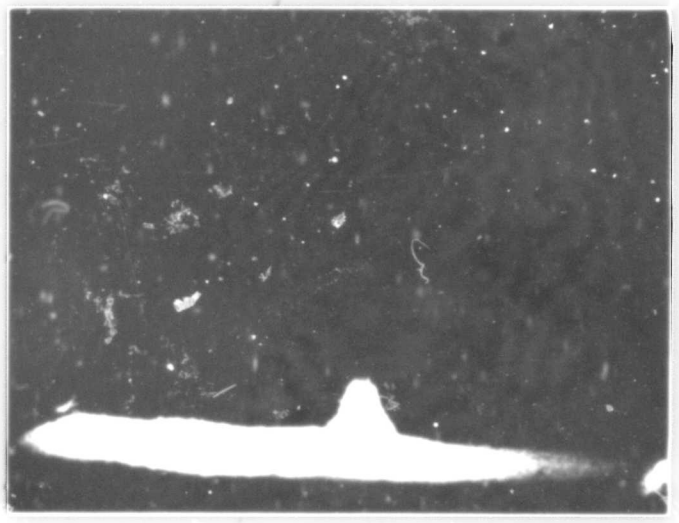

Figure 11. Response of Non-woven Nylon Felt to Ballistic Impact. 85 Microseconds After Impact by 17-Grain Fragment Simulator. Initial Velocity - 765 Feet per Second. Very Close to Ballistic Limit Velocity. Felt - 25 Ounces per Square Yard.

motion are either nearly equal to projectile velocity, or zero, depending upon whether the shear wave has passed that radius. Radial particle velocities normal to the projectile trajectory result from the passage of the tensile wave. These experiments were conducted to obtain dynamic tensile properties of yarn materials.

As a first step in the development of the analytical model, careful experiments are being performed to obtain the information which shows how felts behave during ballistic penetration. Subsequent analyses will seek to illustrate why they behave as they do. These analyses will define the role of the several important material parameters and will provide the basis for material selection and armor design criteria.

EXPERIMENTAL PROGRAM

The objective of the present experimental program is two-fold. The study of the total force opposing projectile motion, as a function of time and displacement during felt material impact, is important. Even more important is the collection of data revealing the manner in which felt materials react to impact. This latter information is utilized to develop relationships defining the various components of the total projectile decelerating force. An experimental procedure has been developed which provides the desired information. The data obtained defines the displacement-time history for numerous points on the rear surface of the felt test specimen. These points form an outline of the felt's deformation profile. Velocity, strain, and strain-rate during the penetration process can be determined. This experimental technique uses an open-shutter camera to photograph the instantaneous location of these points at pre-set time intervals during the history of the impact. The instantaneous location of these points is defined by a spark of one-half microsecond duration, which appears at each of these points at the desired time. This technique eliminates the need for high speed cameras, or of high frequency strobes for illumination. In order to obtain these sparks, a wire is attached to the rear surface of the felt test panel at equally spaced points along a line which passes over the point of impact. At each point of attachment, a small section of the wire is removed to form a gap so that arcing will occur when a high voltage is applied to the wire. Figure 12 is a photograph of the rear surface of a panel that has been tested. This photograph illustrates the wire attachment technique. The slack in the wire is necessary to insure that the movement of the arc-gap will be truly representative of the movement of the felt material at this location. Because of this requirement, it is also necessary to obtain secure attachment over a very small area. This is done by the application of a small amount of plastic cement, or by sewing the wire to the material, depending upon the severity of the test impact conditions.

The voltage pulses necessary to produce the sparks that appear simultaneously at each arc-gap for one-half microsecond at high frequencies, are obtained in the following manner. An aluminum foil switch is mounted on the front surface of the felt material at the point of impact. Upon initial impact of the projectile with the felt, this switch closes causing a capacitor discharge which forms the initial trigger signal. This signal is fed directly into a Tek-Tronix (type 161) pulse generator. The output of this generator is a square gate signal of variable duration. This gate signal activates a Tek-Tronix (type 162)

Figure 12. Attachment of Spark-Gap Wire to Rear Surface of Nylon Felt Sample.

waveform generator, which sends out pulses for the duration of the gate signal. The frequency of these pulses is pre-determined by the setting of the waveform generator and checked by a Hewlett-Packard chronograph. This series of pulses is then fed into a Hewlett-Packard 221A pulse generator, which then sends out pulses of sufficient amplitude to trigger a Model-3 airborne radar modulator. The radar modulator shapes these pulses into square waves of one-half microsecond duration at 12,000 volts. This voltage is applied to the wire attached to the rear surface of the felt. The frequency and total number of voltage pulses can be varied over a wide range of values. Present equipment is capable of 11,600 cycles per second. The number and timing of the voltage pulses obtained during a test are checked by recording the output of the wave generator on an oscillograph. Figure 13 represents such a record. The horizontal sweep speed was one hundred microseconds per division. It can be seen from this record that for this particular test, eleven sparking voltages were applied at 90-microsecond intervals.

Prior to firing a test section of fabric, a calibration picture is taken. This provides the scaling factor necessary when enlarging the negative of the test results so that true dimensional measurements can be made during the data reduction process. The negative is placed in an enlarger, which is adjusted to project the image of the data at the desired magnification. This image is reproduced on a sheet of paper, which is then used to accurately measure the displacements.

Figure 14 is a reproduction of a photograph of test results obtained using the above-described, experimental technique. In this particular test a narrow strip of felt was utilized instead of a square panel. Although it represents an impact condition related to an essentially one-dimensional type target, it is presented here to illustrate the type of data obtained. Eleven arc-gaps were placed at one-half inch intervals on the rear surface of a one-half inch wide strip of nylon felt. The impact velocity was relatively low; approximately 300 f.p.s. Nine voltage pulses were applied at 150-microsecond intervals starting at the time of initial impact. Strain wave propagation is beautifully illustrated in this figure. It is seen that the axial movement of the projectile creates shear waves which propagate outward forming the deformation profile. These shear waves create tensile waves which move out radially at a higher velocity than the shear wave: notice the inward flow of the material before it is displaced axially by the shear wave. This figure illustrates how this test method can be used to investigate strain wave propagation phenomena in felt materials.

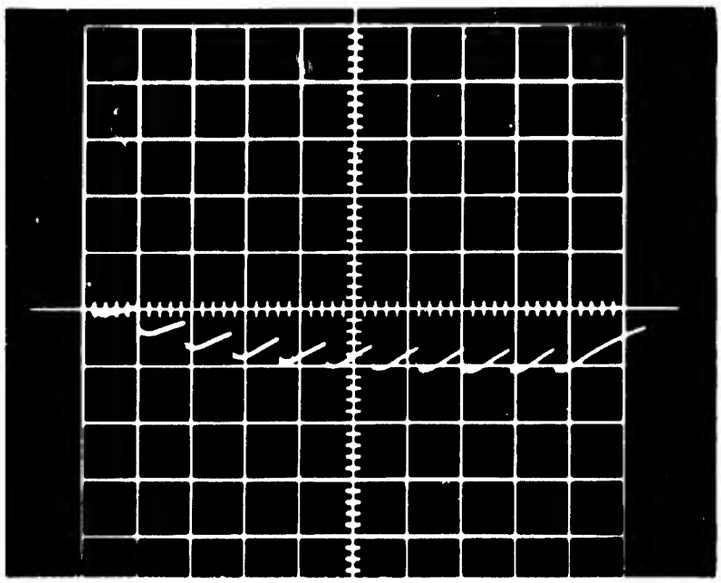

Figure 13. Timing Record of Sparking Sequence.

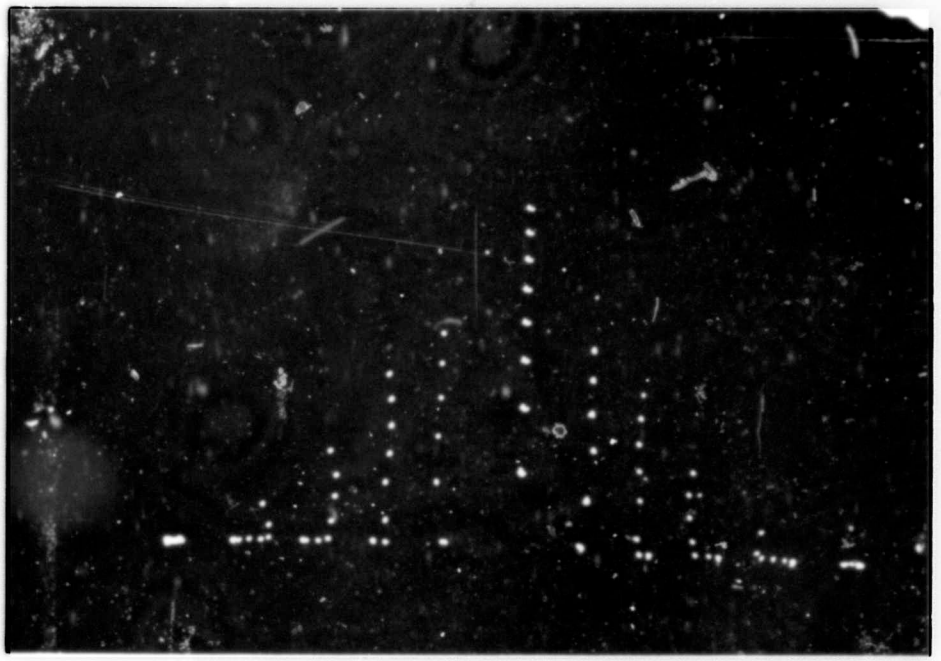

Figure 14. Timed Spark Sequence Recording the Motion of Each Spark-Gap Attached to the Rear Surface of the Felt. Thin Felt Strip Impacted at 300 Feet per Second by 17-Grain Fragment Simulator. 150 Microsecond Interval Between Successive Sparks.

Test data concerning the penetration of felt material by fragments is presented in Figure 15. Eleven arc-gaps were placed at one-half inch intervals on the rear surface of a 7 × 7-inch square piece of 0.40-inch thick nylon, needled felt of the type VEE-1348. The impact velocity of the 17-grain W.A.L. Fragment Simulating Projectile was measured before impact as being 690 feet per second. The electrical equipment was set to produce ten voltage pulses at intervals of 100 microseconds beginning at initial impact; this was verified by the oscillograph record obtained for this test. Therefore, a spark appeared at each arc-gap (thereby causing a pinpoint exposure of the film) at the time of initial projectile-target contact, and every 100 microseconds thereafter, for a total period of 900 microseconds. The points shown on Figure 15 define the location of the immediately adjacent felt material at these instances of time during the deformation process.

Identification as to which set of points represents a given time can easily be made since it is definitely known that ten sparks had to appear at each arc-gap. Referring to Figure 15, ten distinct points are discernible for the center arc-gap which was placed behind the point of impact. The first point (from bottom to top) corresponds to the position of this gap at the time of the first spark, or the original felt position at the time of initial impact; the second point in this series corresponds to the position of this gap at the time of the second spark, or 100 microseconds after impact; the third point 200 microseconds after impact. The tenth and last point is at 900 microseconds. For the arc-gaps placed one-half inch from the center, eight points were obtained. The last point (farthest left) must correspond to the tenth spark or the position of the felt material on a one-half inch radius from the point of impact at 900 microseconds after impact. The next to last spark of this series is the ninth spark (800 microseconds), the next the eighth, etc. By counting back it is seen that the first point represents the first, second, and third sparks, superimposed upon one another. This means that the material at this location (one-half inch from center) was not disturbed by the impact until after the third spark or between 200 and 300 microseconds. Therefore, neither the shear nor tensile waves had propagated out to this radius before 200 microseconds. At one inch radius, it is seen that the tensile wave reached this point some time between 200 and 300 microseconds, but the shear wave did not arrive until after 400 microseconds. This method is used at each radius to establish the timing of each point and, thereby, determine the contour and displacement of the deforming material as a function of time after impact.

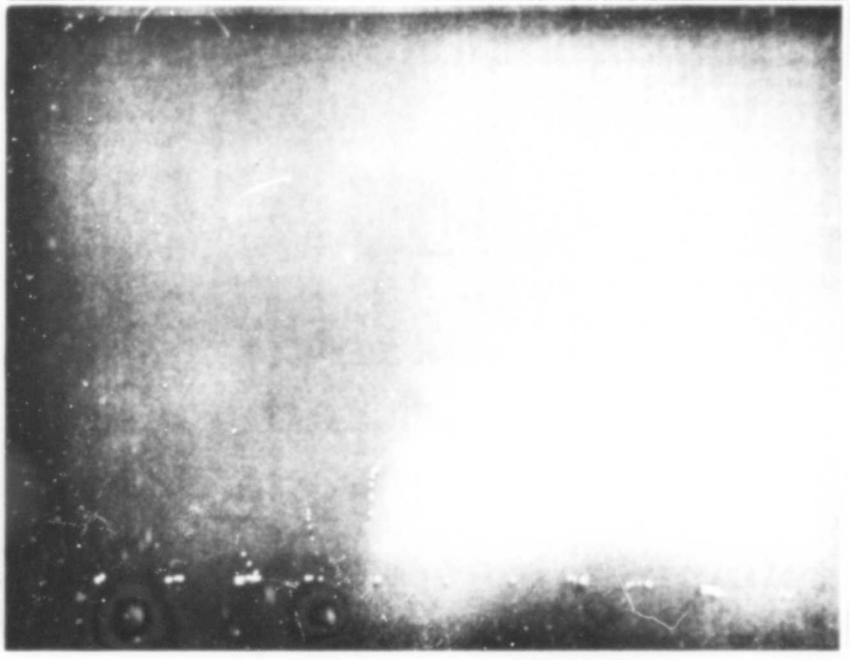

Figure 15. Timed Spark Sequence Recording the Motion of Each Spark-Gap Attached to the Rear Surface of the Felt. 7-Inch Square of 56 Ounce per Square Yard Non-woven Nylon Felt Impacted at 690 Feet per Second by 17-Grain Fragment Simulator. 100 Microsecond Interval Between Successive Sparks.

In order to obtain more accurate data, the arc-gaps are placed at one-quarter inch intervals and higher voltage pulse frequencies are used. Such data are not presented here, because the confusion created by the large number of points would have interfered with the illustration and explanation of the experimental procedure. This data, and photographs such as Figure 15, show that the primary development of the deformation profile is somewhat hemispherical in shape (the initial hemispherical shape becomes less pronounced as the impact velocity approaches the ballistic limit velocity). As the deformation profile continues to develop, the shape becomes more conical, except at the base directly behind the shear wavefront where the material has rotational momentum. This change in shape of the profile is indicative of a changing velocity distribution. This velocity distribution is to be expected due to the shape of the shear stress wave being applied and to the rotational momentum produced by this stress wave. Radial dispersion of the cylindrically expanding stress waves reduces stress magnitudes and the associated particle velocities. The velocity distribution within the deformation profile is very important for the determination of strain and strain rate. The strains developed can be seen in Figure 15 by noting the relative distance between the various points which were initially one-half inch apart.

Other significant data being obtained from the test results are the shear and longitudinal strain wave propagation velocities as related to strain and to strain rate. To date, the data obtained indicate that the shear wave velocity is far from being constant during the penetration process. Early in the process, the shear front is propagating outward at a higher velocity, and then decays to a constant velocity as time progresses. At the early stages of impact, the shear strains and the strain rates are very high. This apparent increase in propagation velocity with strain and with strain rate is evidence that the shear stress-shear strain curve for the felt materials tested is concave upward in nature and/or that the apparent shear modulus is sensitive in a positive degree to strain rate. This situation is also indicated for the tensile strain wave propagation velocity.

To obtain the characteristics of the projectile deceleration as a function of time, the motion of the rear surface of the material behind the point of impact is equated to the projectile motion. This assumption is justified by the fact that this material and the projectile must, very quickly, assume the same velocity. Figure 16 shows a plot of the displacement-time data for the rear surface of the material under the point of impact. These data were obtained from Figure 15 by measuring the

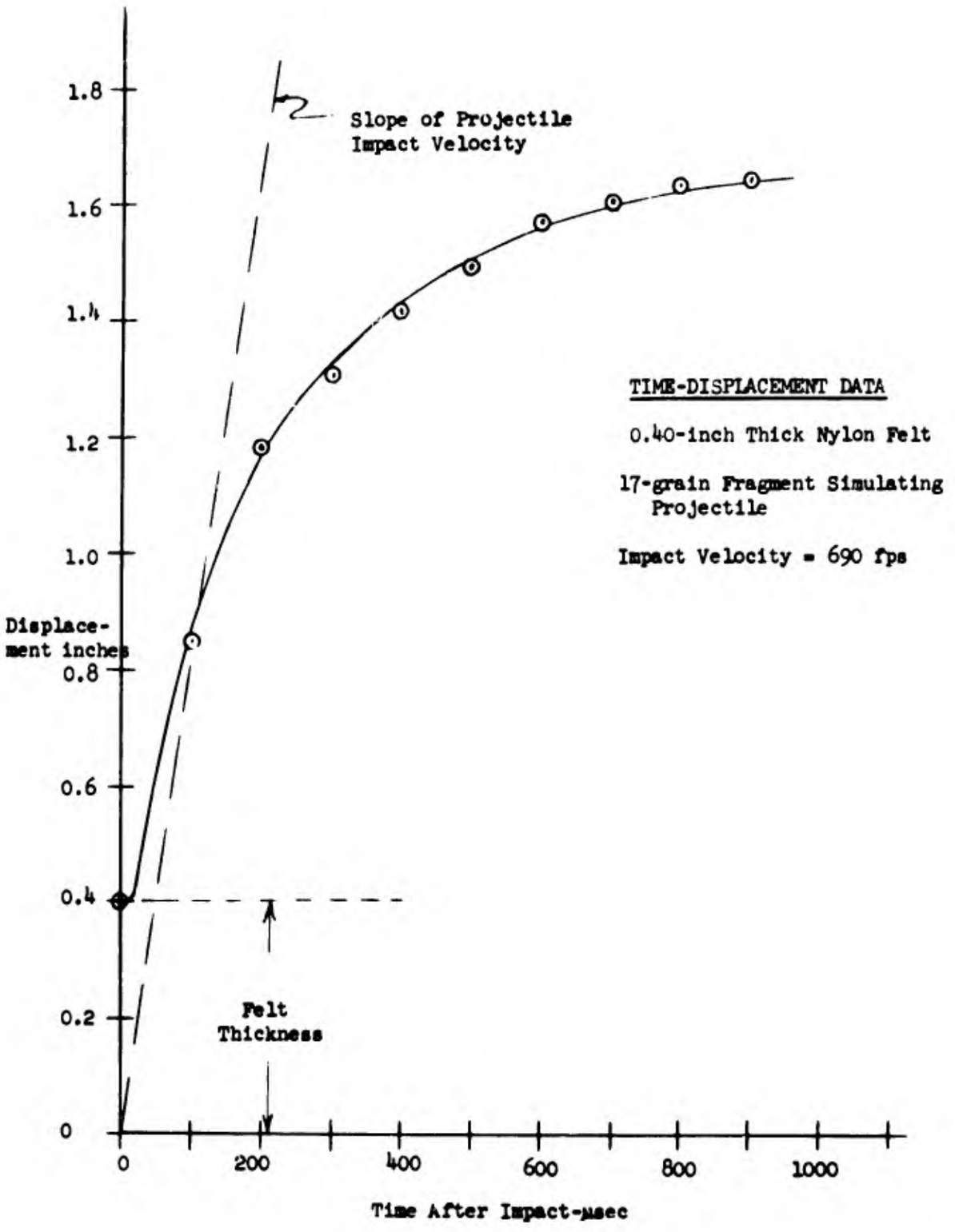

Figure 16. Displacement-Time Curve. 7-Inch Square of 56 Ounce per Square Yard Non-woven Nylon Felt Impacted at 690 Feet per Second by 17-Grain Fragment Simulator. 100 Microsecond Interval Between Successive Sparks.

displacement of the center series of points. Displacement is plotted with reference to the front surface of the test material. The rear surface material under the point of impact remains at its original position for a short period of time until the impact shock wave reaches it and causes it to move. By this time, the projectile will have been decelerated only slightly, and the slope of the time-displacement curve of the projectile and material, at the point of impact, will be slightly less than that which indicates the impact velocity of the projectile (690 feet per second). The impact velocity line is shown on Figure 16. This straight line is used as a guideline in plotting the initial portion of the curve through the data points. The curve represents the projectile time-displacement curve. Figure 16 illustrates the consistency of the data being obtained and the smoothness of the curve described by these points.

In order to obtain the projectile velocity-time relationship, the time-displacement curve is graphically differentiated once with respect to time. Figure 17 shows the results of graphically differentiating the curve of Figure 16. The points shown on Figure 17 are the slopes of the displacement curve measured at 50 microsecond intervals.

The projectile velocity is seen to decrease very quickly with time. However, this deceleration is much less than it would be if the impacted material were rigid. Since the slope of the velocity-time function is proportional to the deceleration force being applied by the felt material, it is seen that the force increases rapidly after impact, reaches a maximum quickly, and then decays with time. The slope of the curve in Figure 17 was measured at various points and plotted as force versus time on Figure 18. The curve, drawn through the points, defines the total reaction force of the felt material which is opposing the projectile motion as a function of time after impact. This curve shows a maximum force being developed of approximately 310 pounds at a time near 80 microseconds after impact. This type of data can be used in conjunction with the analytical model, expressed in terms of stresses, to analyze the maximum stresses being developed during impact, and, thereby determine the relationship between the maximum impact velocity and the various dynamic strength values of the materials.

The corresponding force-distance curve is shown as Figure 19. The area under this curve is equal to the initial kinetic energy of the projectile and, therefore, is also equal to the total amount of work done by the felt during the impact process. This type of data can be used to analyze the amount and manner of energy absorption by the

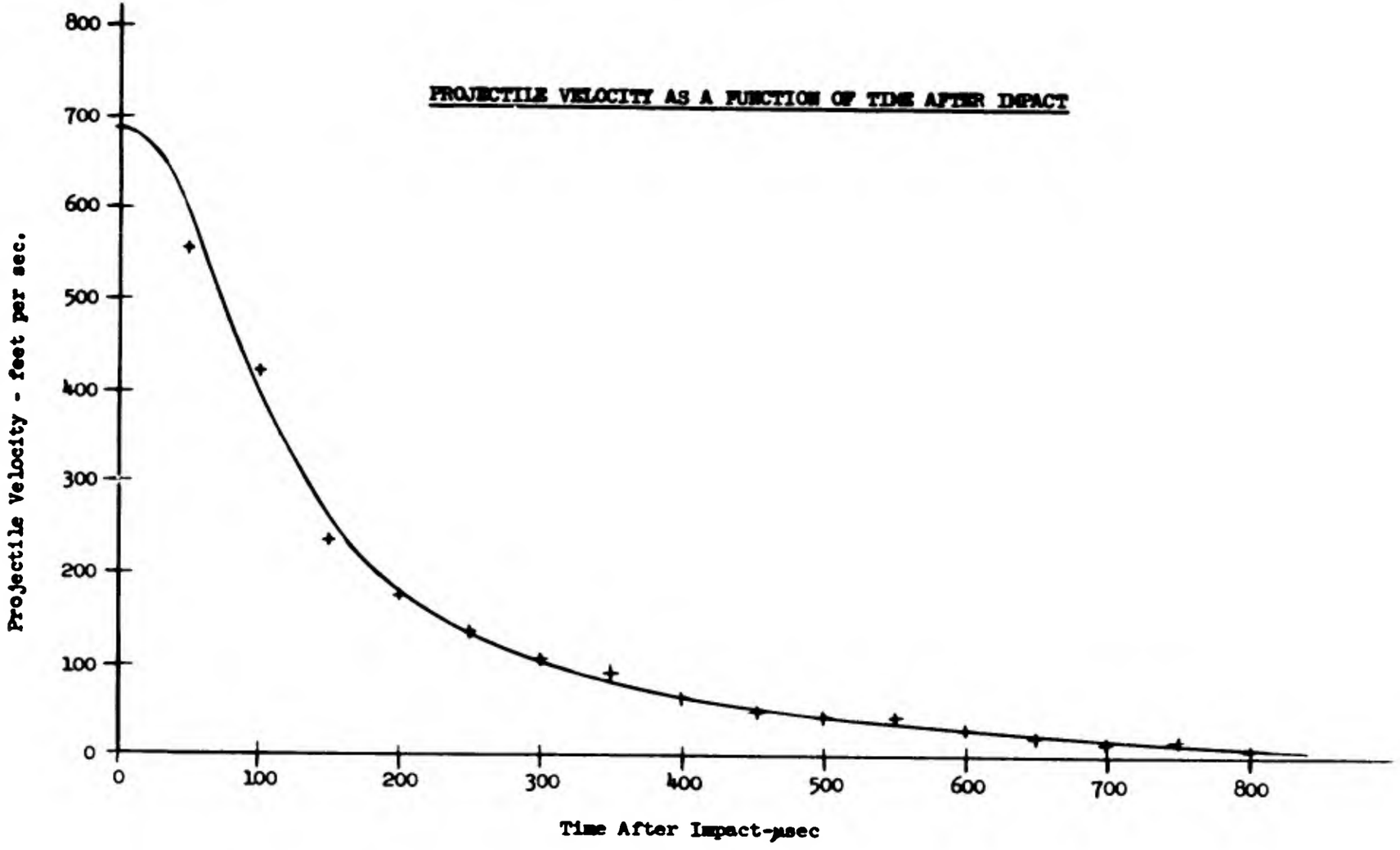

Figure 17. Velocity-Time Curve. 7-Inch Square of 56 Ounce per Square Yard Non-woven Nylon Felt Impacted at 690 Feet per Second by 17-Grain Fragment Simulator. 100 Microsecond Interval Between Successive Sparks.

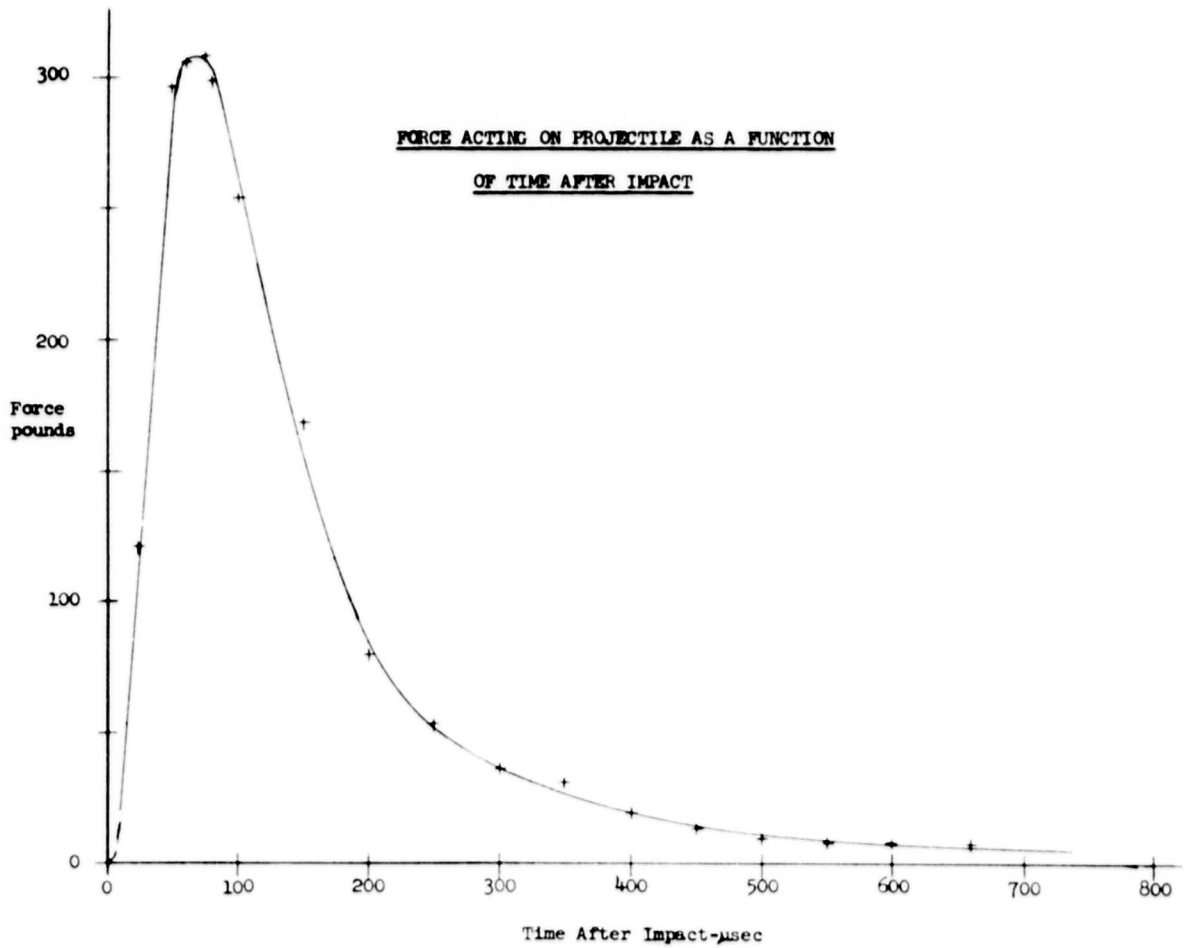

Figure 18. Force-Time Curve. 7-Inch Square of 56 Ounce per Square Yard Non-woven Nylon Felt Impacted at 690 Feet per Second by 17-Grain Fragment Simulator. 100 Microsecond Interval Between Successive Sparks.

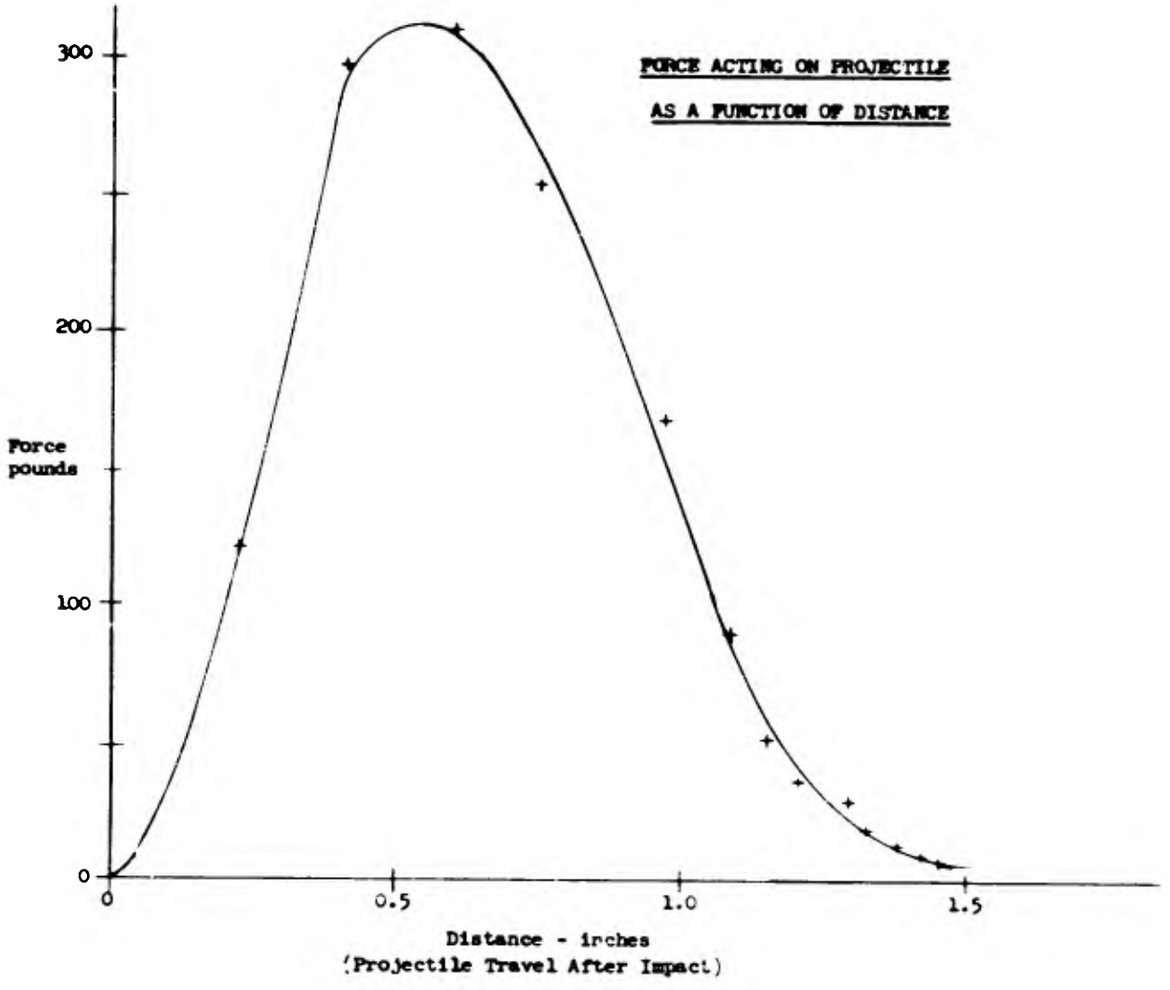

Figure 19. Force-Distance Curve. 7-Inch Square of 56 Ounce per Square Yard Non-woven Nylon Felt Impacted at 690 Feet per Second by 17-Grain Fragment Simulator. 100 Microsecond Interval Between Successive Sparks.

felt material. This energy will be absorbed as kinetic energy of the felt material and as deformation energy. The kinetic energy of the felt material as a function of time can be accurately estimated by complete analysis of the test data shown on Figure 15. By subtracting the kinetic energy of the felt material from the change in kinetic energy of the projectile, the energy absorbed by the felt due to deformation (strain energy and friction) can be determined.

The experimental program is revealing the manner in which felt materials react to impact. It is also providing essential data concerning the dynamic properties of these materials. Analytical equations being developed are expressed in terms of these properties: it is therefore essential that these properties be known.

SUMMARY AND CONCLUSIONS

Non-woven, synthetic, fibre felts offer a lightweight means for defeating blunt projectiles. Below a critical transverse impact velocity, they resist shear at the impact periphery, and momentum is transferred radially into the material by shear waves. For this reason, much more target material must be accelerated. Felts differ from rigid, ductile materials in this respect, and are able to decelerate projectiles over much longer distances and periods of time. Consequently, impact and shear stresses are much lower. This deceleration is accomplished through a deformation of the target which approximates a cone growing with time. The rate of change of momentum of the projectile is equal and opposite to the rate of change of momentum in the target material. To fully understand the penetration process so as to be able to write the equations of motion, the behavior of shear waves, and longitudinal waves induced by the shear waves, will have to be well understood first. These wave mechanics will be a function of the material properties as well as geometry. An experimental program is being conducted to determine how the materials behave. Analytical models will be developed to explain why they behave as they do. These models will include functions relating the material properties to the penetration process, and will serve as the basis for optimizing felts for various armor applications.

BIBLIOGRAPHY

1. Recht, R.F. and T.W. Ipson, "Research to Optimize the Ballistic Performance of Armor Vision Blocks (U)" Final Report, Contract DA-23-072-ORD-1619, for Army Tank Automotive Center, by Denver Research Institute, University of Denver, unclassified report; separately bound confidential appendix, Nov. 1963.

2. Metallurgical Society Conferences, Response of Metals to High Velocity Deformation, Proceedings, A.I.M.E. Conference, July 11-12, 1960, Interscience Publishers, New York, London, 1961, pages 250, 256, 270-271.

3. Rinehart, J.S., "On Fractures Caused by Explosions and Impacts," Quarterly of the Colorado School of Mines, Volume 55, Number 4, October 1960.

4. Frietag, E.H., "Wear and Friction of Metals at Very High Speeds," Institution of Mechanical Engineers, London, Conference on Lubrication and Wear, October 1957, Paper No. 44.

5. Project Thor, "A Suggested Technique for Predicting the Performance of Armor-Piercing Projectiles Acting on Rolled Homogeneous Armor (U)," Technical Report No. 14, Contract No. DA-36-034-ORD-1678, Institute for Cooperative Research, The Johns-Hopkins University, September 1954, Confidential.

6. Zener, Clarence, "The Micro-Mechanism of Fracture," Fracturing of Metals, ASM, 1948, pp. 3-31.

7. Recht, R.F., "Catastrophic Thermoplastic Shear," ASME Transactions, Series E, Journal of Applied Mechanics, presented at ASME Winter Meeting, Nov. 1963, (to be published in 1964).

8. Recht, R.F. and T.W. Ipson, "Ballistic Perforation Dynamics," Journal of Applied Mechanics, Vol. 30, Trans. ASME, Vol. 85, Series E, September 1963, pp. 384-390.

9. Smith, J.C., C.A. Fenstermaker and P.J. Shouse, "Behavior of Filamentous Materials Subjected to High-Speed Tensile Impact," ASTM Materials Science Series 5, Dynamic Behavior of Materials, 1963, pg. 47.

HIGH SPEED IMPACT OF TEXTILES

by

Roy C. Laible

Personnel Armor Materials Research Section
Clothing and Organic Materials Division
U. S. Army Natick Laboratories

BLANK PAGE

CONTENTS

Abstract

The mechanical properties of yarns, felts, and fabrics have been studied in order to gain an understanding of their ballistic properties. From the mechanical properties of polypropylene yarn, good ballistic resistance was predicted. However, the performances of plied polypropylene fabrics under actual ballistic firing was disappointing because their ballistic value in all cases was found to be lower than that of plied nylon fabrics prepared from yarns of comparable stress-strain properties. Possible reasons for this poor performance are low fiber-to-fiber friction, fiber variability, and changes in mechanical properties at ballistic speeds.

Needle-punched nylon felts, on the other hand, gave good ballistic performance. High-speed photography of ballistic impact and high speed testing were both used to determine the reasons for this good performance. In low and high speed tests, felts were found to be subject to much greater elongations than fabrics. Transverse wave or kink velocity is much slower in felts than in fabrics and this partially compensates for the greater elongation. Felts possibly derive their properties during ballistic impact more from fiber-to-fiber friction and fiber straightening than from fiber breakage.

HIGH SPEED IMPACT OF TEXTILES

I. Introduction

From the preceding papers, it is obvious that a great deal of useful work is being conducted in the area of penetration mechanics. In some cases, this work will result in the development of theoretical expressions for the ballistic performance of materials as related to their geometry and material properties. This paper outlines some studies of the mechanical properties of yarns, felts, and fabrics. There are two main reasons for carrying out these studies. The first is based on the hope that from these properties we will be able to predict the type of materials which should show promise ballistically, and this reason ties in with the work which one of the speakers, Mr. Elliot Snell, will report tomorrow. But the second reason is concerned with the work of the previous speakers. Knowledge of material properties should aid workers in penetration mechanics by providing real values for many of the parameters that at present are expressed in letters.

Illustrative of the work on mechanical properties, we will discuss polypropylene as a material and needle-punched felt as a structure.

II. Discussion

A. Polypropylene

Several years ago, a sample of polypropylene yarn with a static strength of 6 gpd (75,000 psi) and an ultimate elongation of 36 percent was obtained. The mechanical properties of this yarn were investigated quite thoroughly, mainly with the objective of understanding its rheological properties. Most of the information on its viscoelastic behavior has been reported in the Journal of Applied Polymer Science[1] and will not be repeated here. It suffices to say here only that it exhibited two pronounced relaxation times and its behavior could be represented fairly well by two Maxwell units in parallel. One of the Maxwell units, representing a relaxation time of $10^{-2.5}$ seconds, indicated a tendency for reasonably good energy absorption at impact speeds. Its ultimate properties were also studied and they showed a tendency for strength to increase and elongation-to-break to decrease with increasing speed of testing. Based upon our previous experience with other high-tenacity fibers (nylon, high strength rayon, and polyvinyl alcohol), we expected good ballistic performance from polypropylene. This expectation, combined with its low moisture absorption and projected low price, encouraged its exploitation.

---

(1) Laible, R. C. and H. M. Morgan, Viscoelastic Behavior of Isotactic Polypropylene Fibers, J. Applied Polymer Science, 6, n21, 269-277 (1962)

T .e ultimate properties of this yarn are shown in Table I.

TABLE I

Mechanical Properties of Moderate Strength Polypropylene Yarn

Property	Rate of Testing		
	20%/min	240%/min	200,000%/min
Tenacity at break (gpd)	5.6	6.3	6.8
Elongation at break (%)	33	30	22

The ballistic properties of a fab ric prepared from this yarn can be expressed as a V_{50} value of 1075 feet/second when plied to give an areal density of 19.2 oz/ft^2. An equivalent areal density in a nylon fabric yields a V_{50} of 1225 feet/second or better.

Two additional polypropylene yarns (PNR #4 and PNR #3) were obtained: one stronger than the original yarn, the other weaker but more extensible. Their properties are given in Table II.

TABLE II

Mechanical Properties of High and Low Strength Polypropylenes

Properties	Rate of Testing		
	20%/min	240%/min	200,000%/min
Material PNR #4			
Tenacity at break (gpd)	8.4	9.2	9.3
Elongation at break (%)	35	27	21
Material PNR #3			
Tenacity at break (gpd)	4.0	4.9	6.2
Elongation at break (%)	75	47	26

The V_{50} values obtained for fabrics made from these two yarns were 1178 feet/second for the PNR #4 and 1100 feet/second for the PNR #3.

The ballistic properties of a fabric are probably dependent in some complex way upon the modulus and work to rupture of the component yarns. Actually, a simple factor composed of the tenacity plus 10 percent of the elongation can be used to relate static mechanical properties to ballistic resistance for a particular fiber type. This was done both for polypropylene and for nylon (Fig. 1). From such curves, one can predict the mechanical properties that should be required of a yarn to reach a particular ballistic value. For example, to obtain a plied polypropylene fabric with a V_{50} of 1300 feet/second would require a yarn with a tenacity of 13.8 gpd and an elongation to break of 12 percent.

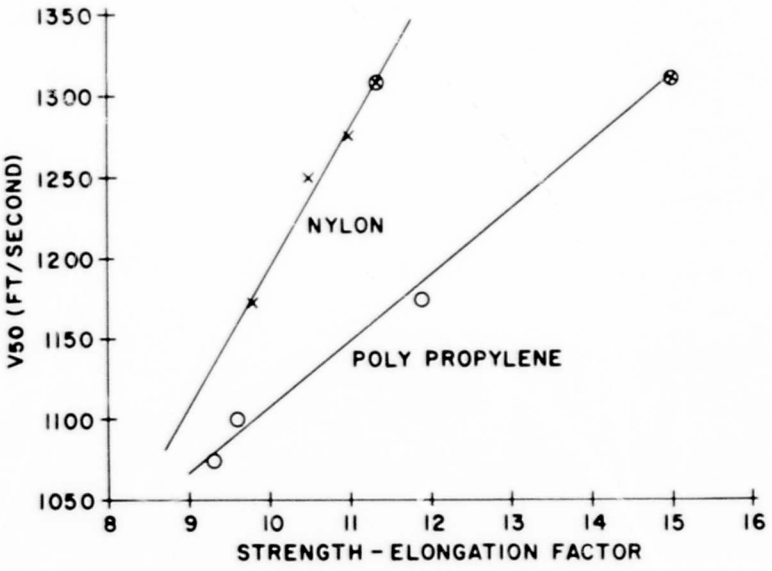

FIG 1 - V_{50} AS A FUNCTION OF STATIC MECHANICAL PROPERTIES

On the other hand, for nylon to reach the same ballistic level, the more moderate requirements of a tenacity of 10 gpd and an elongation of 15 percent would be sufficient. The main conclusion to be drawn from these

results is that the polyolefin type fiber requires much more strength than nylon in order to be ballistically competitive. The Navy is sponsoring work on a super high-strength polypropylene in the 13 to 14 gpd range which will test this conclusion.

The probable reasons for the low ballistic resistance of polypropylene include greater variability of the fiber, its low friction, and possibly some change in the mechanical properties of the component yarns at ballistic speeds. This latter possibility will be checked by high-speed photography of the missile-polypropylene fabric interaction. The effect of friction will be studied by treating fabrics with such agents as colloidal silica.

B. Needle-Punched Felts

Needle-punched felts were of interest because they represent the first fibrous material to show an improvement, ballistically, over the basket-weave nylon used in the armor vest. Earlier work on felts was concerned with laboratory tests that might furnish insight into the reasons for their good ballistic resistance. A series of felts with various degrees of ballistic resistance was prepared. Of the laboratory tests (compression, tensile, dart drop, and punch press penetration), those giving work-to-rupture values (obtained from the punch press penetration) were the best for rating the felts in the order of their ballistic resistance[2].

(2) Laible, R. C. and R. H. Supnik, High Speed Testing as a Measure of the Resistance to Penetration of Needle-Punched Felts, J. Applied Polymer Science, 8, 283-295 (1964)

Figure 2 shows the relationship as the missile energy extracted by the target (calculated from V_{50} values) plotted against the work to rupture from laboratory penetration tests (punch press). Although the the correlation is quite good, the actual values obtained from the laboratory test were of a much lower order of magnitude than the energies extracted from an actual missile. In order to account for this large difference, one of the felts of interest (a 0.1-inch-thick needle-punched nylon felt) was subjected to ballistic impact and the deformation studied by high-speed photography.

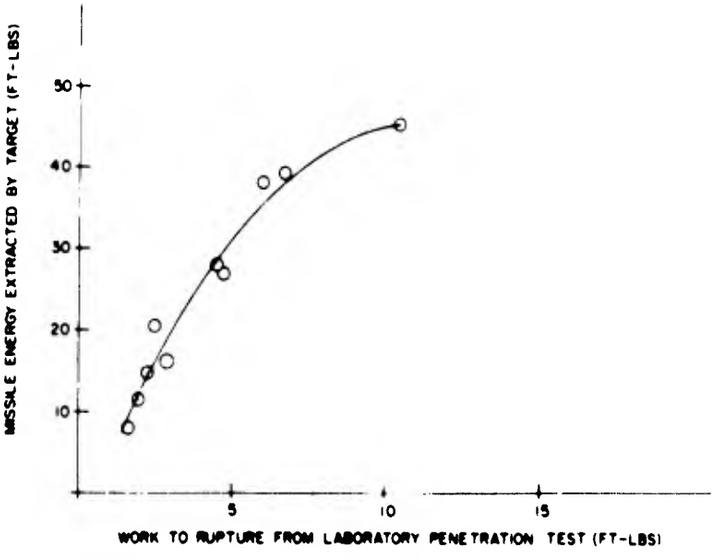

FIG 2 - BALLISTIC PERFORMANCE AS A FUNCTION OF PENETRATION RESISTANCE

The felt was mounted perpendicular to a Beckman and Whitley Dynafax camera for profile photography at a rate of 26,000 frames/second (Fig. 3). A four-millisecond light pulse with an intensity of 10^7 peak beam candlepower obtained from a xenon flash tube provided the lighting. The missile was a 17-grain (1.1-gram) fragment simulator fired from a smooth bore .22 caliber rifle with compressed helium.

A cone was formed from the deformation (Fig. 4). From the cone development, missile velocity and kink wave velocity versus time curves

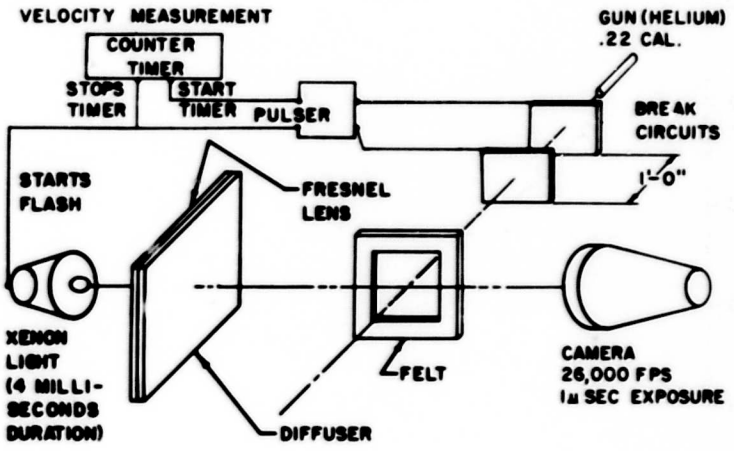

FIG 3 - EXPERIMENTAL SET-UP FOR HIGH SPEED PHOTOGRAPHY TARGET-MISSILE INTERACTION

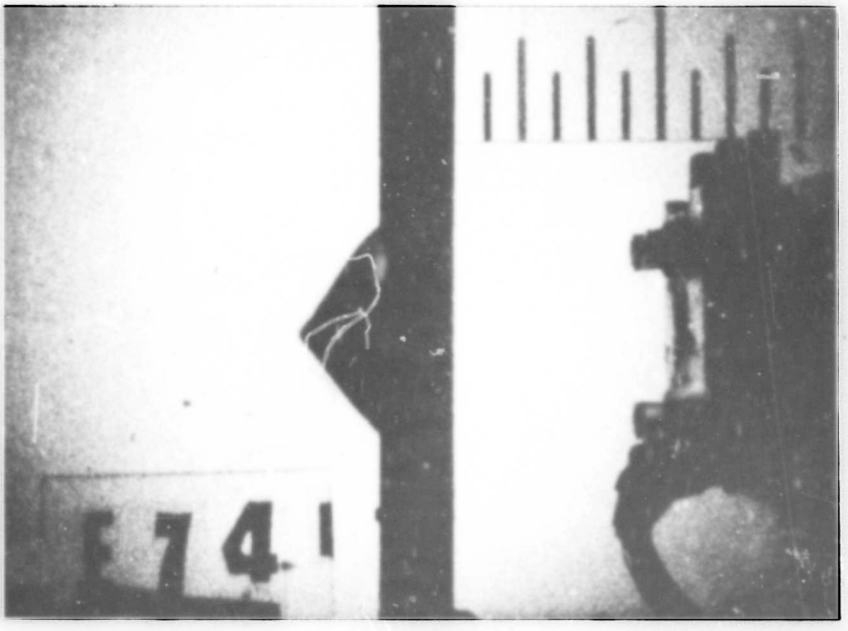

FIG 4 - CONE FORMED DURING FELT DEFORMATION

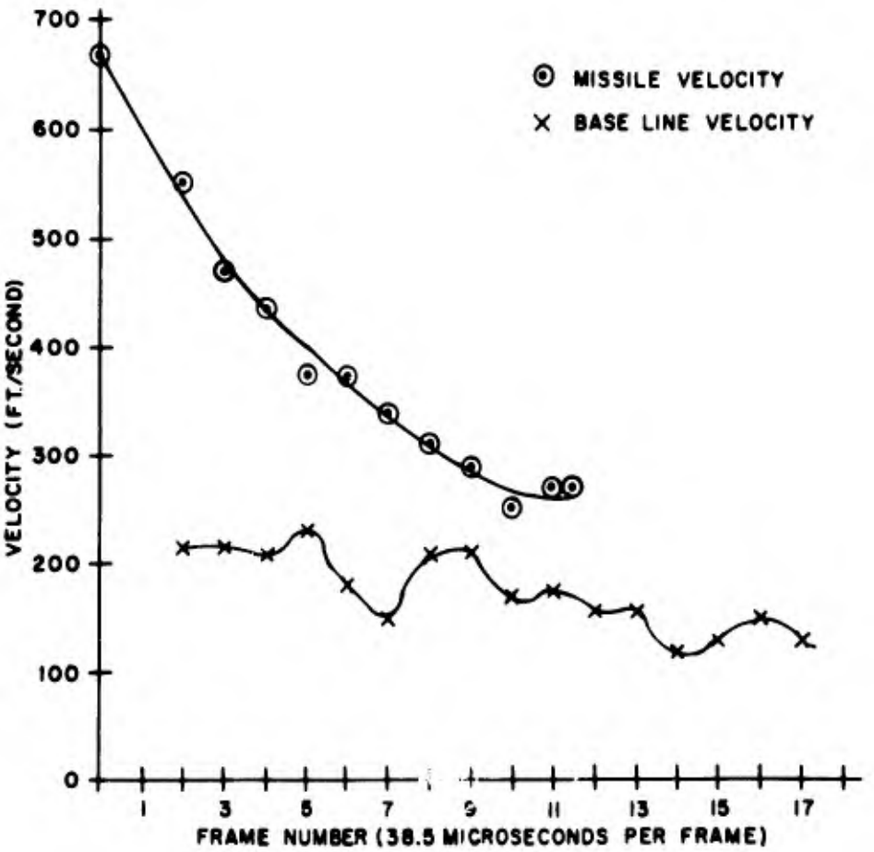

FIG 5 - MISSILE AND BASE LINE VELOCITIES AS FUNCTIONS OF TIME

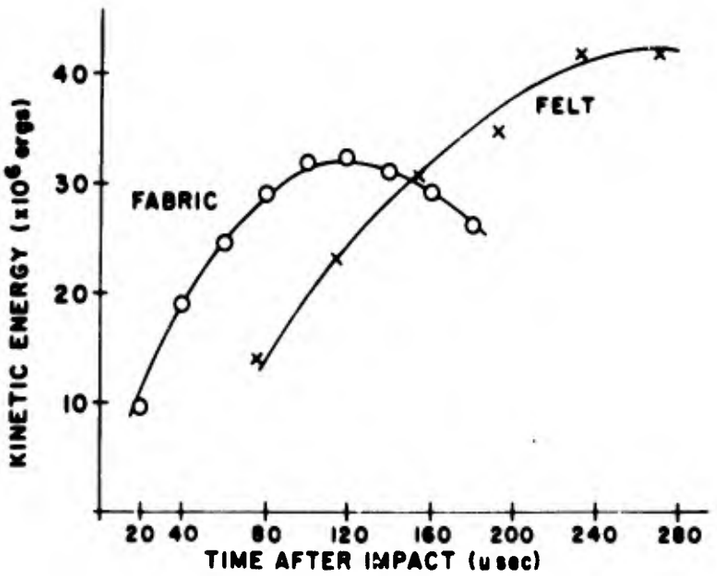

FIG 6 - KINETIC ENERGY OF MOVING TARGET WITHIN THE CONE

were obtained (Fig. 5). Several years ago, somewhat similar studies were conducted on a nylon fabric and it is interesting to compare in Figure 6 the rates of the felt and fabric involvement due to movement of the transverse wave front. The relatively slow rate of the felt involvement in the cone compared to that found in the previous fabric studies is apparent. Thus, although the amount of felt involvement was great enough to account for some of the difference between the laboratory penetration tests and the ballistic tests, one might predict felt to be a poorer ballistic material than fabric because of the slowness of its transverse wave velocity.

In an effort to determine the reasons for the excellent behavior of non-woven nylon felt, or at least for the nature of its deformation, tensile tests were conducted on 1-by 6-inch samples, utilizing a 4-inch gage length. The tests were conducted at rates of elongation of 30, 300 and 300,000 percent/minute.

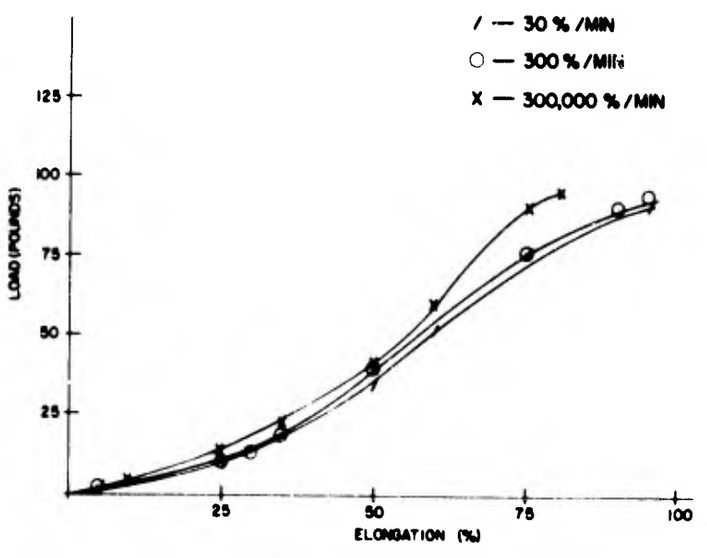

FIG 7 - STRESS-STRAIN CURVES FOR NYLON FELT AT THREE RATES OF ELONGATION

The average stress-strain curves (Fig. 7) show large extensions (80-100%) as compared to other fibrous materials. This is because the elongation in felt is governed by the extent that its fibers are pulled past each other during deformation rather than just by the amount of fiber breakage

that occurs. This type of deformation (fiber-to-fiber friction) is less time-dependent than the usual viscoelastic deformation of continuous filament materials. The first 60 percent of the stress-strain curve is little changed by a 10,000-fold change in the rate of straining. Furthermore, the deformation of felt is of a permanent type--the cone formed persists to a large degree long after impact--while fabrics deformed similarly recover elastically after impact.

III. Conclusions and Future Plans

From the results to date, we can draw the following tentative conclusions:

1. The energy that is absorbed ballistically by felts is greater than that obtained in a laboratory penetration test because the felt involvement is greater than is allowed by the laboratory test.

2. Felt possesses a ballistic advantage over fabrics at low and moderate incident missile velocities because of the mechanism of deformation. This deformation is based upon frictional forces developed between the individual nylon fibers in the felt, thus greater extensions of a plastic and irreversible type are possible than for fabric structures.

Future work will be devoted to defining the missile-felt interaction more thoroughly and to applying the results obtained to the selection of better armor materials.

BLANK PAGE

STUDY OF THE PHENOMENON OF COLD-DRAWING (PLASTIC YIELD) IN HIGH POLYMERS

by

R. D. Andrews, Jr.

Textile Division
Mechanical Engineering Department
Massachusetts Institute of Technology

STUDY OF THE PHENOMENON OF COLD-DRAWING (PLASTIC YIELD) IN HIGH POLYMERS

An exploratory study of the phenomena of cold-drawing and plastic yield in high polymers has been conducted in which the stress-strain properties and the geometry of yielding were investigated for two glassy amorphous polymers: polystyrene and polymethyl methacrylate. Stress-strain properties and cold-drawing behavior of polystyrene (PS) were obtained in tensile tests at constant strain rate as a function of temperature and degree of pre-orientation. The drawing of polystyrene in dead-load tensile creep was also investigated. The properties of polymethyl methacrylate (PMMA) were investigated in tensile tests at constant strain rate as a function of temperature, strain rate, molecular weight, and cross-linking. Compression tests were run on both polymers to study the effect of a different stress field; effects of temperature and of density changes produced by thermal history were also examined. Throughout these experiments, the exact deformation and/or fracture mode was noted.

Our work has presented the results of a preliminary six-month research project having as its aim a general exploratory survey of the effects of several of the significant variables, utilizing these two amorphous polymers -- PS and PMMA. We wished to characterize as well as possible some of the principal features of the drawing (or yield) phenomenon, in such a way that recommendations could be made as to what approach would be desirable in a more full-scale and long-range investigation of the phenomenon.

PRELIMINARY INVESTIGATION OF MECHANICAL AND OPTICAL RESPONSE OF POLYMERS TO IMPACT

by

Anthony F. Wilde
John J. Ricca
Francis deS. Lynch

Personnel Armor Materials Research Section
Clothing & Organic Materials Division
U. S. Army Natick Laboratories

BLANK PAGE

CONTENTS

ABSTRACT

To obtain basic information about the mechanical and optical response of polymers, studies are being made of stress-wave propagation in transparent plastics by observing the dynamic strain and birefringence produced by mechanical impact. Instrumentation and techniques have been developed for: synchronization; projectile alignment; intense, monochromatic illumination; and achievement of one-dimensional wave propagation in the impacted specimen. Preliminary studies have been made of the wave shape and velocity in polymers; changes in wave characteristics have been noted during their crossing of interfaces between dissimilar materials.

The dynamic strain-fringe constant of CR-39 plastic has been studied over a range of strain rates by simultaneous measurement of the strain and birefringence occurring during the nearly linear leading edge of the strain pulse. No distinct strain-rate dependence could be discerned over this range. However, comparison of the average dynamic strain-fringe constant with the static value indicated a slight rate dependence over this larger range of strain rates.

PRELIMINARY INVESTIGATION OF MECHANICAL AND OPTICAL RESPONSE OF POLYMERS TO IMPACT

I. Introduction

Studies of dynamic mechanical and optical properties of transparent materials are being conducted in order to obtain a better understanding of the mechanisms involved in deformation, penetration, and fracture during a ballistic impact. To understand these mechanisms in detail, the dynamic behavior must be related to the molecular and structural make-up of the material. The phenomena exhibited by the material in response to the impact can be used to determine certain of its dynamic properties and to serve as a basis for correlation with the material's molecular and micro-structural features.

This initial study has been concerned with non-destructive low-speed impaction of transparent organic polymers. One of the phenomena chosen for investigation was stress-wave behavior. This choice was made for the following reasons:

a) The stress wave is the first disturbance propagated into the material by impacts occurring at sub-sonic velocities, and hence may govern to a certain extent the subsequent deformation and fracturing processes.

b) Stress-wave study can lead to the determination of dynamic modulus, attenuation (energy dissipation), and dynamic stress distribution at high loading rates in impacted materials.

Stress waves can be detected by devices sensitive to the mechanical strain produced and, with certain transparent specimens, by observation of the dynamic birefringence accompanying the disturbance. Birefringence can be used to observe stress-wave propagation, distribution, and transmission or reflection at interfaces. This information would be of great interest in an engineering study of armor behavior during and after impact. In addition, birefringence data can provide information of a more basic nature because the birefringence results from orientation of molecular groups or structural entities which have different polarizabilities in different directions, i.e., they are optically anisotropic. Identification of these anisotropic groups and characterization of their response to mechanical deformation should ultimately lead to a better understanding of material behavior on a micro scale during mechanical impact.

II. Types of Studies Using Birefringence

A. Engineering Approach

Brown and Selway (1) used an electromagnetic shaker to apply sinusoidal axial displacements to a low-modulus plastic material at strain rates up to 3500 percent strain per second.* They derived the stress, strain, birefringence, phase angles between them, and stress-optic coefficients of the material. Dally, Riley, and Durelli (2) observed the behavior of low-modulus plastic materials undergoing impact by dynamic

*Strain rates were not specified in these references; instead, for purposes of comparison, the authors of this paper estimated the values given here from the data in the cited works.

pendulums and by dropped weights. Dynamic moduli, stress- and strain-optic coefficients, energy loss, and pulse degradation were computed at strain rates up to 6400 percent strain per second. Clark and Sanford (3, 4) impacted high-modulus plastics with pointed projectiles to produce strain rates generally less than 10,000 percent strain per second.* Dynamic moduli and stress- and strain-optic coefficients were calculated from these experiments. Flynn, Gilbert, and Roll (5, 6) explosively loaded both low- and high-modulus plastics by detonation of electric primers, producing considerably higher strain rates.* A dual-beam polariscope enabled them to separate the principal stresses and to observe the distribution of dynamic stresses.

The above mentioned investigators developed experimental techniques involving photoelasticity and high-speed photography. The birefringence, stress, and strain were used as tools to measure stress-wave propagation, attenuation, and distribution. The chemical and structural properties of the material were not considered in the interpretation of results.

B. Chemical and Structural Approach

Andrews, Rudd, and Gurnee (7, 8, 9) investigated several glassy amorphous polymers and obtained static moduli and stress-optic coefficients. Correlations were made with the nature and location of the optically anisotropic groups in the polymer molecules; effects of temperature and molecular pre-orientation upon these photoelastic properties

*See footnote on p. 184.

were also observed and discussed. Stein et al (10) measured the dynamic birefringence of partially crystalline polymer films during extension and also during sinusoidal vibration at low frequencies. The birefringence was attributed largely to transient orientation of anisotropic crystals in the film.

These last two groups of investigators were attempting to explain the photoelastic mechanism in terms of the fundamental physical behavior of the molecular groups and structural entities comprising the material. The rates of strain used were relatively low or zero (static testing); thus the experimental conditions were even farther from those which simulate ballistic impact.

C. Approach to be Used in This Investigation

It is reasonable that a fundamental understanding of material behavior during high-rate loading or ballistic impact should require the combination of both approaches outlined above. The techniques of rapid loading and the accurate recording of transient phenomena should be applied to materials possessing known systematic variations in structure or composition. Comparison of high-rate mechanical behavior with specific material structural properties can then be started, with the aim of providing correlations between the two for subsequent analysis and interpretation.

The work to be described in this paper covers just the development of certain experimental techniques and the preliminary results, without any correlations with the structural features of the specimen material.

III. Instrumentation and Procedure

The experimental objective involved in this study was the simultaneous measurement of dynamic mechanical strain and birefringence experienced by transparent polymeric materials under various rates of impact loading.

Loading and strain measurement techniques and specimen dimensions were the same for all experiments. Two methods used separately in observing dynamic birefringence were: 1) high-speed photography, and 2) photocell detection.

A. Loading Technique and Specimen Dimensions

Transparent plastic strips 1/4 inch thick, 1-1/2 inches wide, and approximately 18 inches long were impacted symmetrically at one end by cylindrical steel missiles 1/2 inch in diameter and 1 inch long fired from an air gun in a velocity range of approximately 100 to 150 feet/sec.

The air gun consisted of a steel pipe 1/2 inch internal diameter and 20 inches long connected to a solenoid valve which led to a helium gas cylinder. Before firing, the gas cylinder reduction valve was opened to provide the desired pressure. The gun was fired by manual closure of an electrical circuit which opened the solenoid valve. A "break wire"

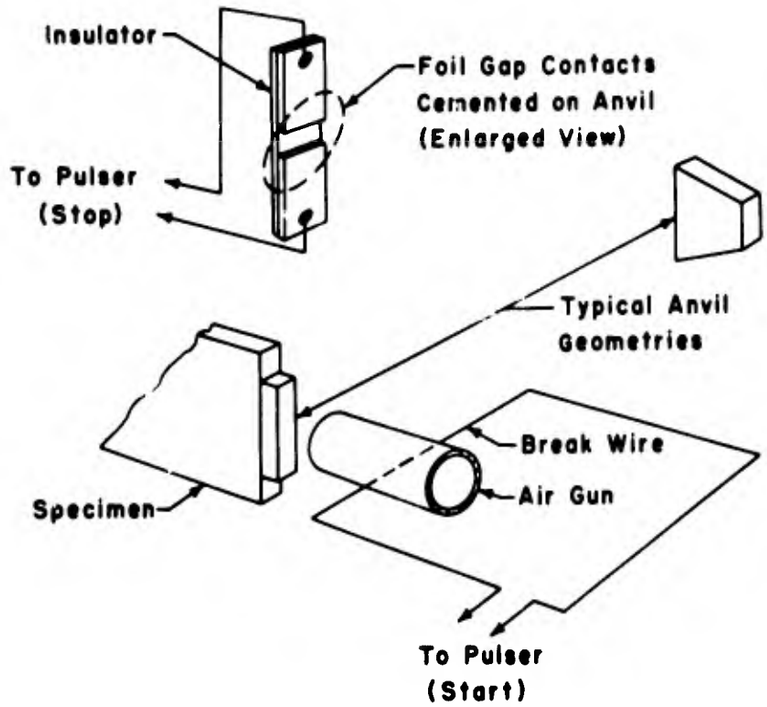

Figure 1 - Missile velocity measurement and anvil geometry.

circuit and a "make foil gap" circuit (Fig 1) provided the start and stop pulses to a 10-megacycle electronic counter (Systron-Donner, Model 1034) for time interval measurements used in calculating missile velocities.

The loading rate was varied by lead and steel anvils of various shapes cemented to the end of the specimen which was to undergo impact. The anvils were used to modify the shape of the pulse propagated into the specimen and to prevent fracture of the specimen at the impacted edge. Typical anvil geometries and the location on the specimen are shown in Figure 1.

B. Strain Measurement Technique

The strain records were obtained by a method similar to that used by Clark (3). Two etched Constantan foil strain gages (Baldwin-Lima-Hamilton, FA-03-12-L, 120 ohm, gage factor 2.00, 0.04-inch gage length) were cemented (EPY-150) on opposite sides of the plastic specimen and connected in series to cancel bending strains. The strain gages were located

6 inches from the impacted end of the specimen. The strain gage potentiometer circuit consisted of these two gages in series with a 1000-ohm output resistor and a 7-1/2-volt battery. An oscilloscope was used to record the strain pulse.

C. Birefringence Measurement Techniques

1. High Speed Photography. The plastic specimen was placed within a dark field circular polariscope (Figs. 2 and 3) and impacted as described above. The resulting optical disturbance propagating through the specimen was then photographed with a Beckman & Whitley (B&W) Dynafax camera (Model 326), which recorded two rows of 16 mm images on 35 mm film at 26,000 frames per second with 1 microsecond exposure time per frame. The framing rate was determined by means of the Systron-Donner 10-megacycle electronic counter. Kodak Royal-X pan film was used and was developed in DK-50 at 68°F for 10 minutes with constant agitation. The light source consisted of a xenon flash lamp (General Electric FT-506) used with a B&W electronic flash unit (Model 357). The B&W flash unit had been modified to increase the intensity of the light pulse. The new measured approximate value was 10^7 peak beam candlepower as determined with a commercial light-measurement device. This modified light pulse had a duration of 4 milliseconds; however, the light intensity decreased during this

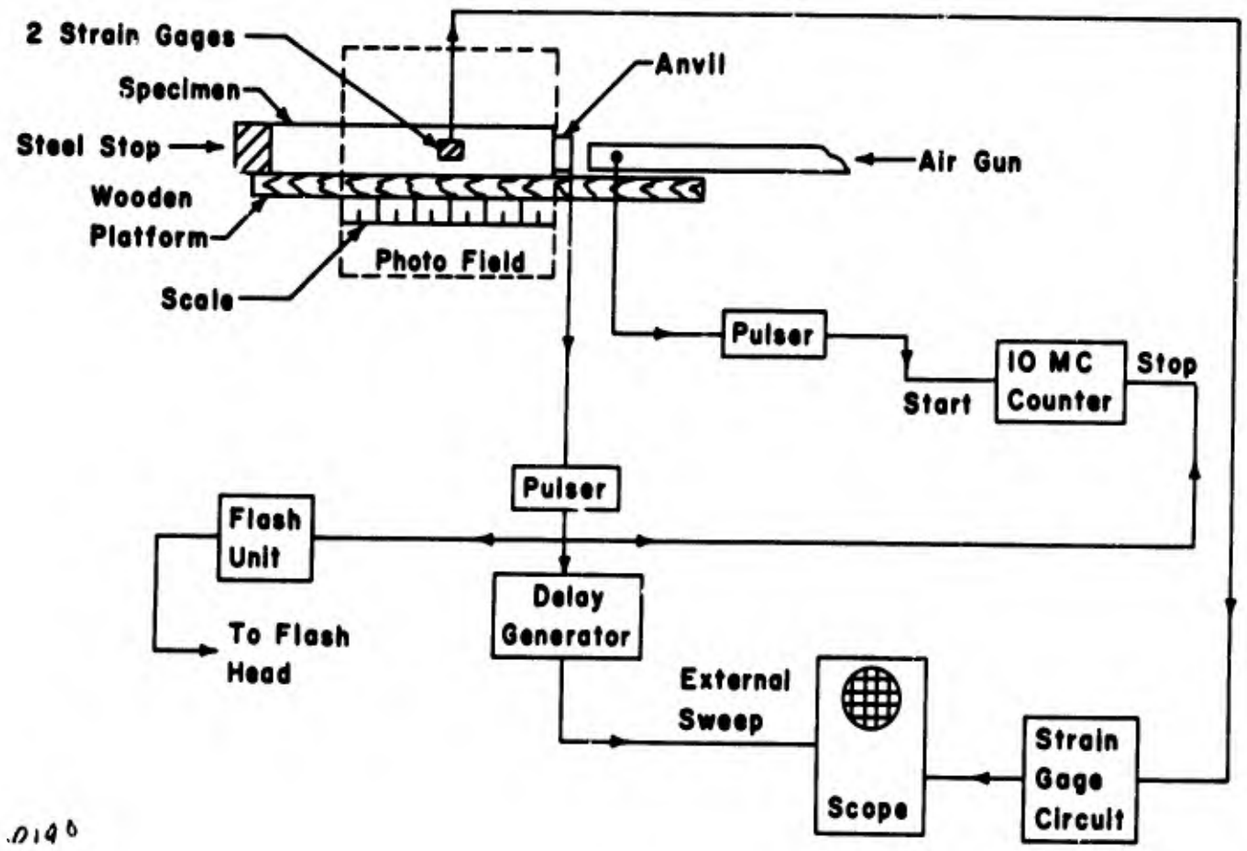

Figure 2 - Schematic diagram of apparatus for loading, strain measurement, and synchronization.

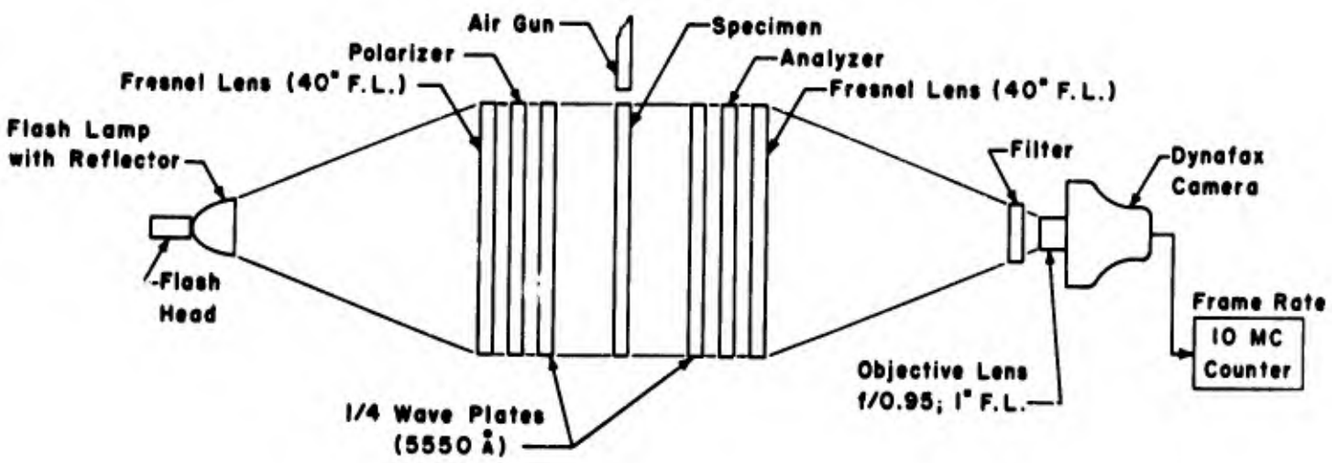

Figure 3 - Arrangement of photographic and optical components.

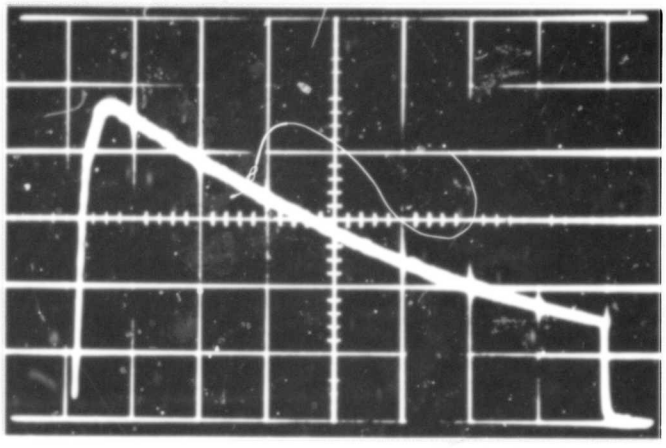

Figure 4 - Oscilloscope record of the modified light pulse intensity. Each large horizontal unit equals 0.5 millisecond.

interval, as is shown in Figure 4. The useful portion of the pulse occurred during the first millisecond following the peak. A bandwidth of light from approximately 5000 to 6000 angstroms was obtained with a Wratten 58B filter.

2. Photocell Detection.

The photocell technique was an alternate method used in observing dynamic birefringence. The same B&W flash system served as the light source. The technique consisted of projecting left-handed circularly polarized light through a slit 1/16-inch wide and 1/2-inch high masked off on the specimen. The light emerging from the slit then passed through a right-handed circular polarizer, a combination of filters (Wratten 77A and 58B), and a lens which converged the light on a small area of the photocell cathode (RCA Type 935).

When the specimen was impacted, the fringes, seen as alternate light and dark areas in Figure 5, produced a modulation of light intensity on the photocell as this optical disturbance propagated past the slit. The slit was located a measured distance (1/2 inch or less) in front of the strain gage.

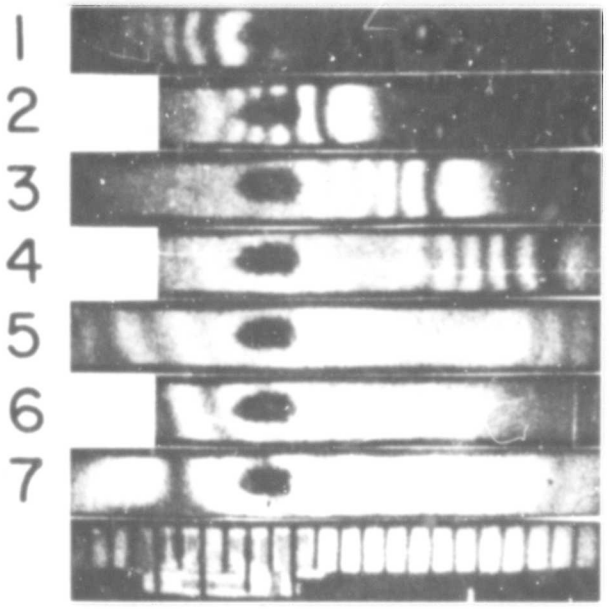

Figure 5 - CR-39 specimen impacted from the left (missile not shown in photograph). Optical wave is propagating to the right at approximately 5000 feet per second. Large dark spot in each frame is the strain gage. Time interval between frames is 38.5 microseconds; exposure time of each frame is 1 microsecond. Scale marked in 1/2-inch divisions.

The outputs from the photocell circuit and the strain gage circuit were simultaneously recorded with a dual-beam oscilloscope (Tektronix, Type 551) fitted with a Polaroid camera.

IV. Experimental Results

The preliminary experimental efforts were concerned with production and detection of stress waves in commercially available transparent plastics. For the initial tests, the photographic method of detecting birefringence was chosen to observe the propagating stress wave. The purpose was to observe the performance of the apparatus and to determine if the wave propagation was essentially one-dimensional in the regions more than several inches from the impacted surface. For one-dimensional propagation, where the component wavelengths are long compared to the transverse dimensions of the specimen, the elastic wave velocity is given by the simple relationship

$$c = \sqrt{E^*/\rho} \qquad \text{Equation (1)}$$

where E^* is the dynamic modulus of elasticity and ρ is the density of the material.

Figure 5 is a photographic record of a propagating stress wave produced in CR-39 plastic by an impact. In frame 1, the fringes are moving to the right and are approaching the strain gage; subsequent frames show the fringes passing the gage. In frame 5 a second group of fringes appears at the left end and moves to the right; these correspond to the trailing edge of the pulse. The area between the two groups of fringes defines the peak of the pulse, where the fringe order is almost constant. The fringes at the leading edge of the pulse are perpendicular to the longitudinal axis of the strain gage, showing that propagation is essentially one-dimensional in this region. These optical data delineate the general shape of the pulse.

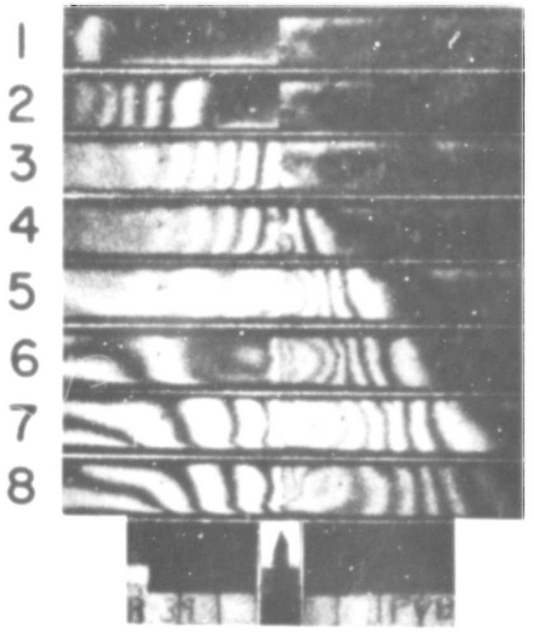

Figure 6 - CR-39 (left) and PVB (right) composite specimen impacted from the left. Arrow points to the interface. (Missile not shown in photograph). Optical wave is propagating to the right at approximately 5000 feet per second in the CR-39 and 2300 feet per second in the PVB. Time interval between frames is 38.5 microseconds; exposure time of each frame is 1 microsecond. Scale marked in 1-inch divisions.

Birefringence can also be used to show a strain pulse crossing an interface between two unlike materials. Figure 6 illustrates this for a similar impact with photographic conditions identical to those of the previous figure.

In each frame the arrow points to the interface between CR-39 (a high-modulus, rigid plastic) and plasticized polyvinylbutyral (PVB, a low-modulus, flexible plastic). In frames 1, 2, and 3, the fringes are moving in the CR-39 to the right toward the interface. Later frames show the fringes traveling in the PVB. Several differences can be noted in the behavior of these two materials:

a) The fringes move faster in the CR-39, owing to its greater value of $\frac{E^*}{\rho}$.

b) Near the interface, the fringes are more closely spaced in the PVB than in the CR-39 owing to different optical activity and lower value of $\frac{E^*}{\rho}$ for the PVB.

c) The fringe spacing in the PVB rapidly increases with increasing distance from the interface, showing a marked attenuation of the strain pulse with a concurrent decrease in steepness of the wave front.

Observations of this type can be used in the study of stress-wave propagation, transmission at interfaces, and full-field stress distribution in a transparent material which has undergone mechanical impact.

Birefringence and mechanical response data are frequently expressed in terms of a strain-fringe constant (C) for the material,

$$C = \frac{\epsilon_1 t}{n} \qquad \text{Equation (2)}$$

where ϵ_1 is the longitudinal strain, n is the fringe order, and t is the thickness of the specimen. Strain-fringe constants have been measured

for many types of materials, but there is little published information concerning their rate dependences.

The above-described experimental techniques were used to determine for CR-39 the values of strain-fringe constants over a range of strain rates. CR-39 was chosen for this study because the degree of optical activity was conveniently large for development and testing of the apparatus, and birefringence data were available (3) for the lower values of strain rates attainable by this technique.

In order to specify a rate of strain, only the leading edge of the strain pulse was examined; the slope of this approximately linear portion was defined as the strain rate. The slopes were determined from the strain gage records by fitting the data to a straight line by the method of least squares. The durations of these linear portions varied from about 15 to 200 microseconds, depending on the strain rate. This portion of the pulse, corresponding to these time durations, has a length in CR-39 plastic of 1-inch or greater, thus the averaging effect of the 0.04-inch gage can be neglected. At strain rates greater than 10,000 percent per second, the fringes were so closely spaced that they could not be resolved by the high-speed photographic system. Accordingly, in all dynamic tests, the fringes were detected by a photocell whose

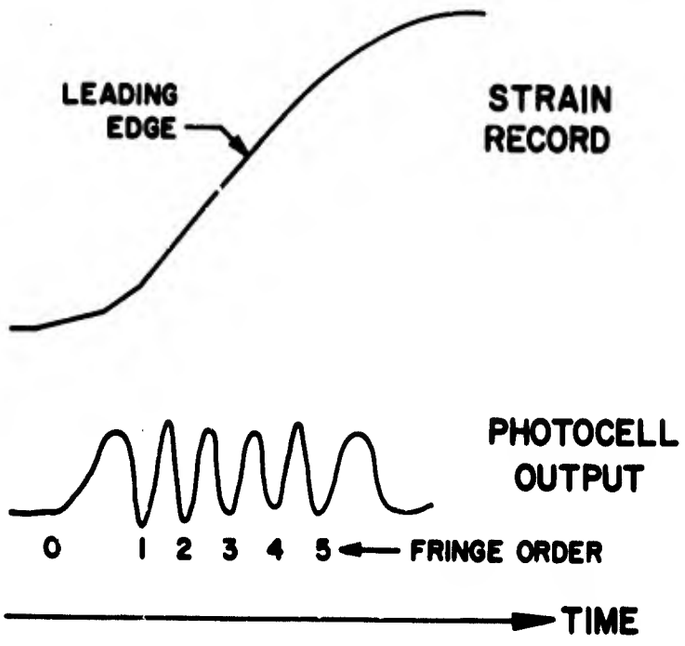

Figure 7 - Sketch of typical strain and photocell records obtained simultaneously with the oscilloscope.

output is shown in the sketch of the oscilloscope record (Fig 7).

When the integral and half-integral fringe orders were plotted against the corresponding strain magnitudes, a linear graph was obtained (Fig 8). The slope of this line was determined by the method of least squares; the slope was then

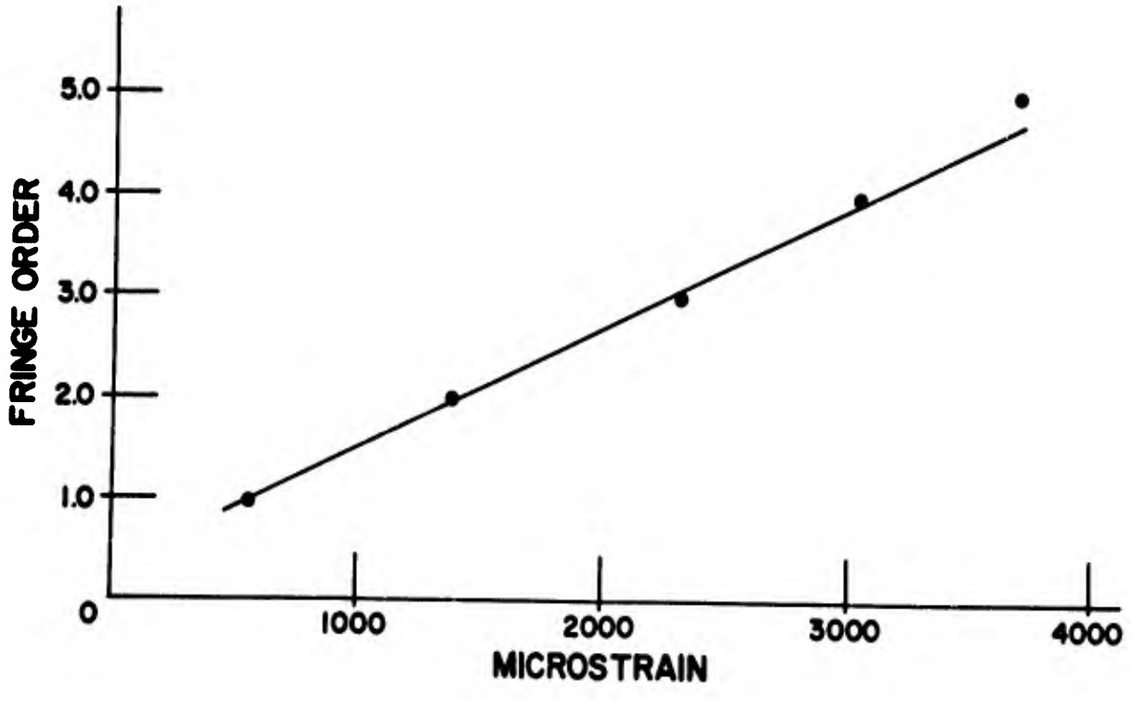

Figure 8 - Typical relationship between integral fringe order and strain magnitude for the leading edge of the pulse.

used in calculating the dynamic strain-fringe constant. A series of strain rates was obtained by varying the type of anvil. To avoid any possible effect of amplitude upon the results, all calculations of strain rate and strain-fringe constant were restricted to data occurring between fringe orders 1.5 through 4.0, inclusive.

The static value of strain-fringe constant was obtained by stretching the specimen in an Instron Tester, Model TT-Cl, at a rate of 0.34 percent strain per minute. As each dark fringe appeared, the machine was stopped for a few seconds and the strain value was obtained from an extensometer mounted on the specimen (Riehl "clamp-o-matic", graduated in 0.0001-inch divisions with a 2-inch gage length). A plot similar to that of Figure 8 yielded the value of the static strain-fringe constant.

The average value of static strain, indicated by the strain gages when computed from the manufacturer's gage factor, was found to be about 96.5 percent of the true strain. This was determined by comparing the gage reading with that indicated by the extensometer during extension of the CR-39 specimen by the Instron at a rate of 0.34 percent strain per minute. This response factor, which is in good agreement with a published figure (4) for foil strain gages, was assumed to give the dynamic response factor also and was therefore used to correct all the strain gage measurements obtained dynamically.

TABLE I

STRAIN RATE AND STRAIN-FRINGE CONSTANT VALUES FOR CR-39 STRIP SPECIMEN

Test No.	Strain Rate (in units of 1000% strain/second)	Strain-Fringe Constant (in units of microstrain-inches/fringe)
1	13.5	242
2	12.4	249
3	10.3	247
7	2.3	272
8	2.7	253
10	5.3	257
11	7.4	257
12	11.9	257
13	23.5	255
14	30.6	275
15	30.3	269
18	28.9	280
19	23.4	251
20	3.2	267
21	23.7	259
23	14.0	241
24	11.8	255
27	22.9	261
28	22.7	242
29	20.3	239
30	14.3	223
31	4.8	254

The static modulus of CR-39 was determined by stretching the specimen in the Instron at a rate of 2.8 percent strain per minute; readings were taken from a load cell and the extensometer. The dynamic modulus, E, of CR-39, was estimated by means of the equation, $E = \rho c^2$. The density, ρ, which was found to be 1.32 grams per milliliter, was determined from the buoyant force exerted on a specimen immersed in water. The longitudinal wave velocity, c, was obtained from the time required for a longitudinal strain pulse, produced by impact, to travel from the strain gage site to the end of the specimen and return to the gage site as a reflected pulse. This velocity was found to be 1.56×10^5 centimeters per second.

A total of 22 dynamic strain-fringe experiments was performed. The strain rate varied from 2,300 to 30,600 percent strain per second; the longitudinal strain-fringe constants varied from 223 to 280 microstrain-inches per fringe. The data are presented in Table I. It can be seen that no distinct trend emerges from these results. Attempts to fit these data to a straight line by the method of least squares indicated a very low coefficient of correlation. Although it might be possible, empirically, to fit these data to higher order non-linear equations, it was felt that the consequent implication of a transition due to an apparent minimum in the strain-fringe values was not warranted.

Accordingly, the dynamic strain-fringe data were averaged and then compared to the static value. Table II summarizes the results both from this investigation and from that of Clark (3).

TABLE II

STRAIN-FRINGE CONSTANTS AND MODULI FOR CR-39

	This Investigation	Clark Investigation (3)
Range of Dynamic Strain Rates (percent strain/sec)	2, 300 to 30, 600 (22 values)	3, 800 to 14, 600* (10 values)
Average Dynamic Strain Rate (percent strain/sec)	15, 400	7, 400*
Range of Dynamic Strain-Fringe Constants (microstrain-inches/fringe)	223 to 280 (22 values)	237 to 276 (10 values)
Average Dynamic Strain-Fringe Constant (microstrain-inches/fringe)	255	260
Average Static Strain-Fringe Constant (microstrain-inches/fringe)	299	280
Static Modulus (psi)	278, 000	276, 000 to 330, 000
Dynamic Modulus (psi)	468, 000	452, 000

*Values estimated by the authors of this paper; see footnote Section II, A

Clark did not characterize his dynamic values in terms of a strain rate but used, instead, an effective loading time. He averaged his 10 dynamic values and made a linear interpolation between this average

and his static values when all were plotted as functions of the logarithm of loading time. The authors of this paper treated their data in a similar fashion, i.e., by making a linear interpolation between the averaged dynamic and static points when they were all plotted against the logarithm of strain rate. Both treatments illustrate a similar trend, i.e, the longitudinal strain-fringe constant decreases with increasing strain rate (decreasing loading time). This trend is small, only 6 or 7 strain-fringe units per order of magnitude in strain rate, hence is too slight to be detected by these types of dynamic experiments alone, even over the considerably wider range of dynamic strain rates provided by this investigation in comparison to that of Clark (3).

V. Discussion

It is concluded that, at room temperature, the longitudinal strain-fringe constant of CR-39 plastic decreases slightly with increasing strain rate in the range of 10^{-2} to 3×10^{4} percent strain per second.

A preliminary molecular interpretation of these results must involve those groups of the molecule which are optically anisotropic. A smaller strain-fringe constant means a smaller ratio of mechanical strain to optical retardation. If there is only one optically active group in the specimen repeat unit, the data indicate that this group would apparently undergo more orientation relative to the total strain as the strain rate increases. If several types of optically active groups

are present, each type may contribute different amounts and directions of retardation to the overall optical effect. Unfortunately, with CR-39 the latter is probably the case. This thermosetting material, a polymer of allyl diglycol carbonate, contains a complex repeat unit with several probable sources of optical activity, namely, two carbonate groups and an ether linkage. Therefore discussion of the observed time-dependent effect in terms of specific molecular group(s) is not now possible.

From an engineering point of view, the observed rate dependency is an important factor to be considered in any dynamic study involving the photoelastic properties of CR-39. Measurements of stress or strain distribution or of wave transmission at interfaces with armor that contains CR-39 components would have to be corrected accordingly. These strain-optic data would also be necessary in studies of dynamic stresses in other mechanical structures where CR-39 models are used for photoelastic measurements and analysis.

VI. References

1. Brown, G. W. and D. R. Selway, Frequency Response of a Photo-Viscoelastic Material, Experimental Mechanics, 4, 57 (1964)

2. Dally, J. W., W. F. Riley, and A. J. Durelli, A Photoelastic Approach to Transient Stress Problems Employing Low-Modulus Materials, J. Applied Mechanics, 26, 613 (1959)

3. Clark, A. B. J., Static and Dynamic Calibration of a Photoelastic Model Material, CR-39, S.E.S.A. Proceedings, 14, 195 (1956)

4. Clark, A. B. J. and R. J. Sanford, A Comparison of Static and Dynamic Properties of Photoelastic Materials, Experimental Mechanics, 3, 148 (1963)

5. Flynn, P. D., J. T. Gilbert, and A. A. Roll, Photoelastic Studies of Dynamic Stresses in Low Modulus Materials, Proceedings of the Army Conference on Dynamic Behavior of Materials and Structures, Springfield, Mass. Sept. 1962

6. Flynn, P. D., J. T. Gilbert, and A. A. Roll, Some Recent Developments in Dynamic Photoelasticity, S.P.I.E. Journal, 2, 128 (1964)

7. Andrews, R. D., and J. F. Rudd, Photoelastic Properties of Polystyrene in the Glassy State. I. Effect of Molecular Orientation, J. Applied Physics, 28, 1091 (1957)

8. Rudd, J. F., and E. F. Gurnee, Photoelastic Properties of Polystyrene in the Glassy State. II. Effect of Temperature, J. Applied Physics, 28, 1096 (1957)

9. Rudd, J. F. and R. D. Andrews, Photoelastic Properties of Polystyrene in the Glassy State, III. Styrene Derivatives and Copolymers, J. Applied Physics, 31, 818 (1960)

10. Stein, R. S., S. Onogi, K. Sasaguri, and D. A. Keedy, Dynamic Birefringence of High Polymers II, J. Applied Physics, 34, 80 (1963)

EVALUATION OF CERAMICS FOR PERSONNEL PROTECTION

by

Dr. Richard S. Liebling

The Carborundum Company

EVALUATION OF CERAMICS FOR PERSONNEL PROTECTION

The purpose of this study is to correlate physical properties of various ceramics with their ballistics performance. An attempt has been made to choose materials with a significant range in properties. Table I lists the materials to be investigated and some of their properties:

TABLE I

	SiC	Al_2O_3	TiB_2	BN
Hardness, Mohs	9.2	9	9	2
Knoop (100g)	2500-3000	2000	2700	-
Density (g/cc) (Theoretical x-ray density)	3.21	3.986	4.52	2.27
Density (g/cc) (available and to be used in this program)	2.1 2.7 3.1	3.5 3.7 3.9	4.3	2.1
Modulus of Rupture (psi at rt)	20-30,000	30-60,000	19,000	7-16,000
Modulus of Elasticity (psi at rt)	$56\text{-}60\times10^6$	50×10^6	53×10^6	$5\text{-}12\times10^6$

Specifically, Carborundum intends to use "KT" silicon carbide, a self-bonded silicon carbide having a density of 3.1; an SG silicon carbide composition, a material similar to "KT" silicon carbide but not as dense; and a "Delta" silicon carbide composition, a low density recrystallized form of polycrystalline silicon carbide. The alumina used in this study will, in large measure, be sintered alumina. Tests will also be conducted on hot pressed alumina having a density of about 3.93. The titanium diboride and boron nitride will be hot pressed materials. Boride "Z", a zirconium diboride, molybdenum silicide composition, will also be investigated.

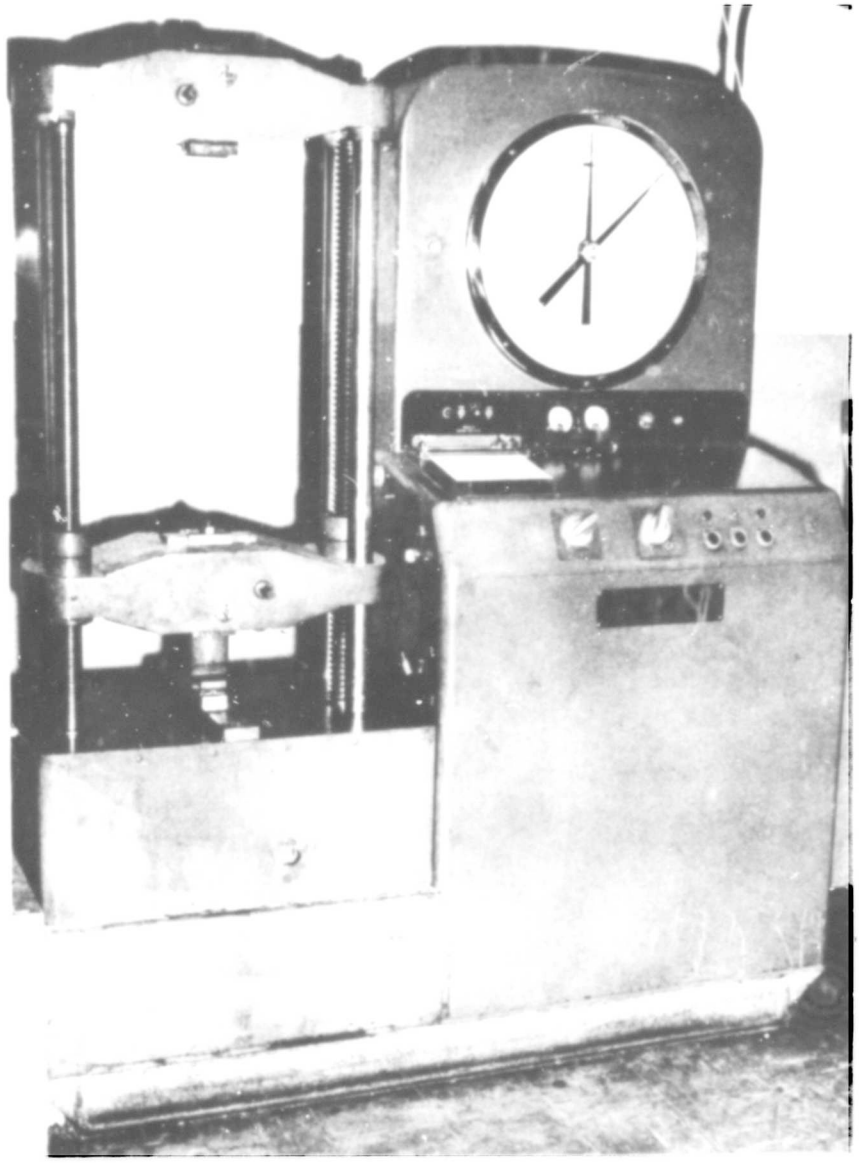

Figure 1 - Riehle Universal Screw Testing Machine

The tests to be made include: modulus of rupture, compressive strength, impact strength, modulus of elasticity and microhardness. The results of these tests will be correlated with density and microstructure.

The equipment available for this program includes: a Riehle Universal Screw Testing Machine, an Impact Tester of Carborundum design, a Tukon Hardness Tester, a sonic modulus of elasticity apparatus, and a variety of metallographs. The Riehle apparatus (Fig. 1) may be used for compressive and tensile strength measurements. The use of such accessories as the model DU deflectometer and the Pend-O-Matic Strain Rate Indicator make it possible to measure moduli of rupture and elasticity. A four-point loading jig will be used for MOR (flexural) testing. A maximum load of 60,000 pounds can be applied at a controlled rate. The impact tester (Figs. 2 & 3) is a device used to measure the energy required to break ceramic bars. A stainless steel plunger is permitted to fall upon the sample from a controllable height. The energy absorbed in breaking the bar is determined by subtracting the kinetic energy of the plunger after breaking the bar from the kinetic energy of the plunger dropped with no test bar. The kinetic energy is computed by measuring the velocity of the plunger by using an electric eye, the light of which is cut by a shoulder on the plunger, and an electronic counter which measures the time the electric eye current is interrupted. Microscopic examinations will be made to determine grain size, shape, and orientation, and other features of importance. Modulus of elasticity measurements will also be made sonically for comparison with those made using the Riehle Tester. The sonic apparatus is shown in Fig. 4.

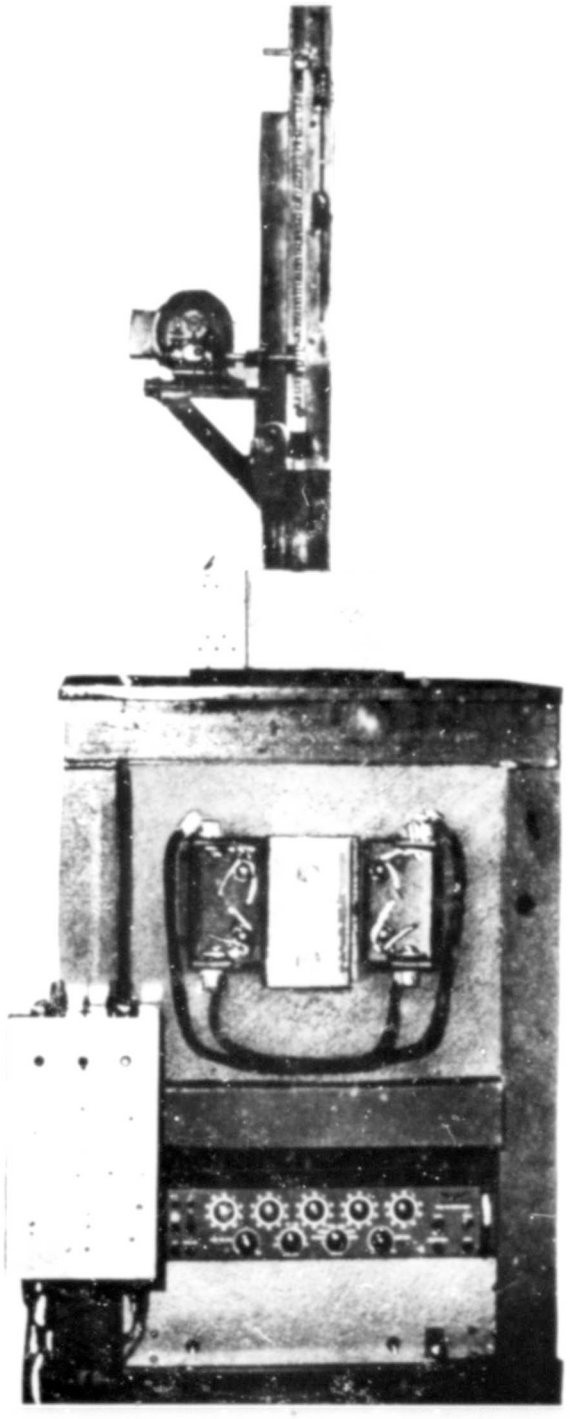

Figure 2 - Impact Tester

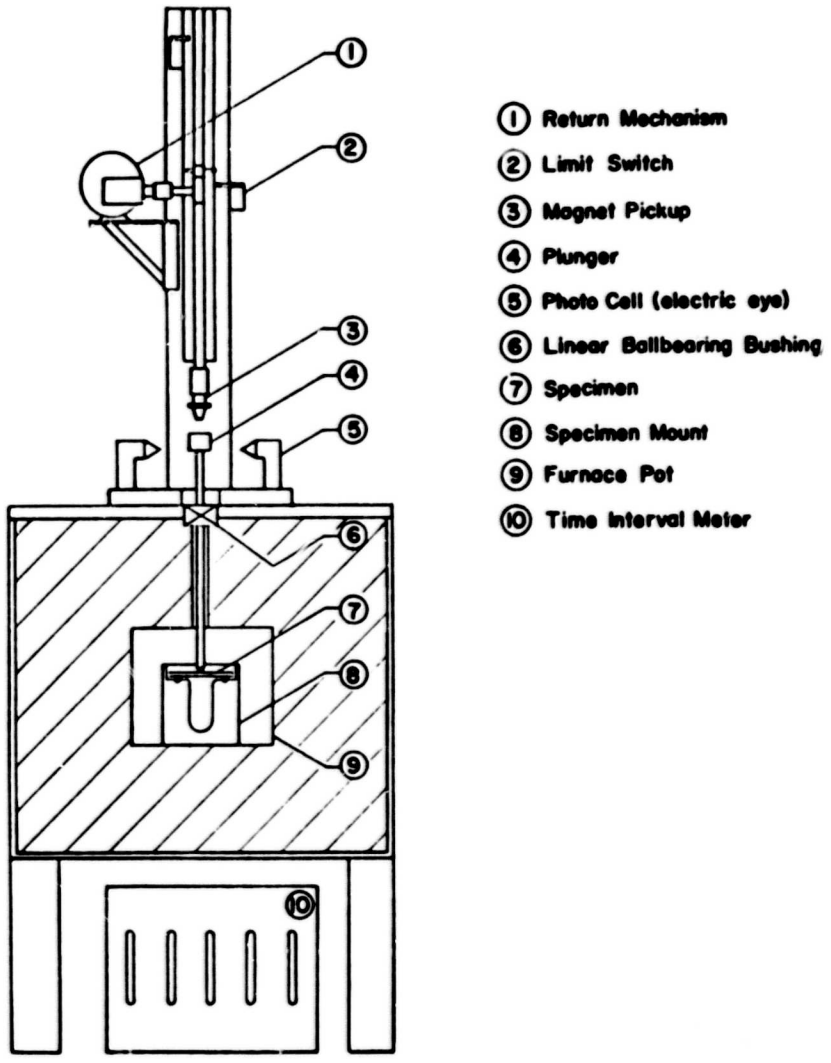

Figure 3 - Impact Tester

During testing, the plunger, 4, is dropped from a height controlled by the limit switch, 2. After breaking the specimen, 7, the plunger is returned to its former height by means of a magnetic pick-up, 3, which is part of the return mechanism, 1. The time interval meter, 10, measures the length of time the electric eye current, 5, is interrupted.

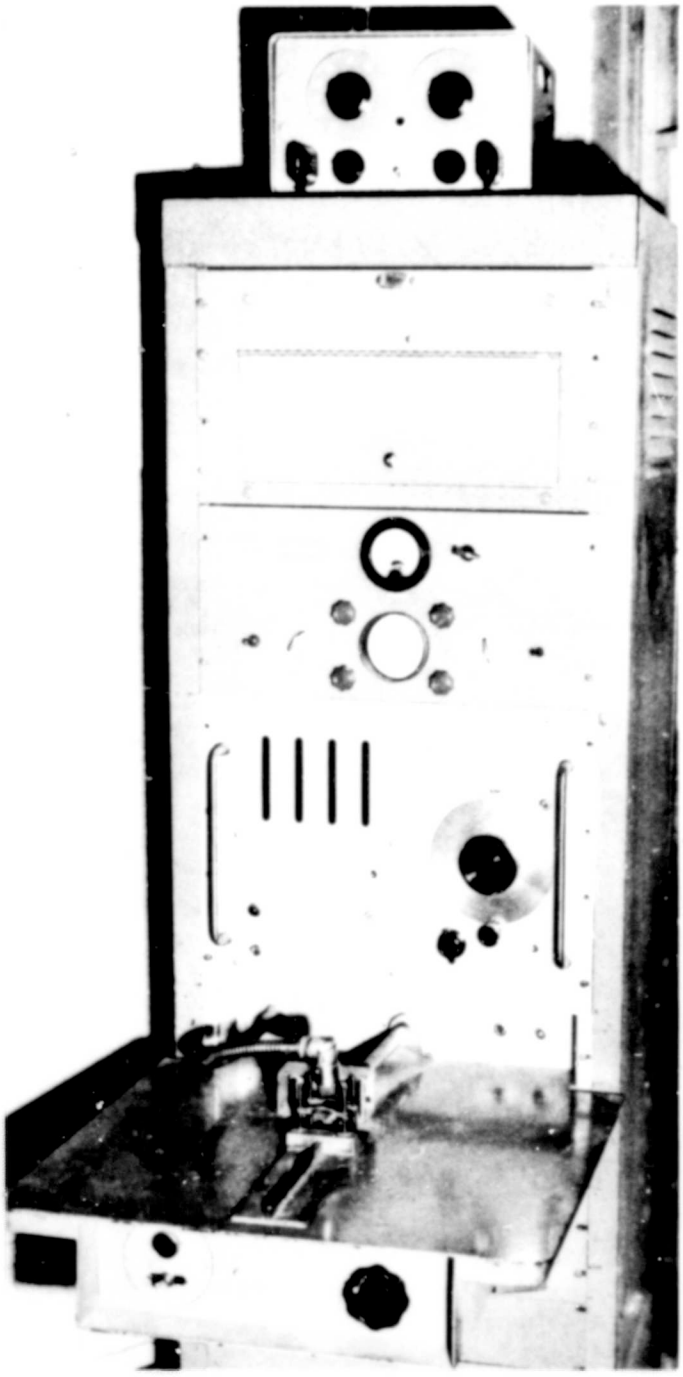

Figure 4 - Sonic Apparatus for Measuring Modulus of Elasticity

Samples used in modulus of rupture, modulus of elasticity, and impact strength tests will measure 3" x 1/2" x 1/4". Compressive strength tests will be performed on specimens 1/4" in diameter and 1/2" in length. Ten specimens will be used in each test. Ballistics test specimens will be of two sizes: 5" in diameter with an areal density of 6 pounds per square foot and 3" in diameter with an areal density of 1.75 pounds per square foot.

Physical properties will be analyzed statistically and correlated with ballistic test results. Our Mathematics Branch is directed by Charles A. Bicking, noted for his work in the field of statistics. He was associated with General Leslie E. Simon (Ret.), formerly the Director of Carborundum's Research and Development Division.

Purchase orders for the necessary materials have been submitted and testing will begin as soon as possible.

BLANK PAGE

Unclassified
Security Classification

DOCUMENT CONTROL DATA - R&D

(Security classification of title, body of abstract and indexing annotation must be entered when the overall report is classified)

1. ORIGINATING ACTIVITY *(Corporate author)*
U. S. ARMY NATICK LABORATORIES

2a. REPORT SECURITY CLASSIFICATION
Unclassified

2b. GROUP

3. REPORT TITLE
ARMOR MATERIALS RESEARCH. Part I. Proceedings of a Meeting of Armor Materials Research Contractors, 19-20 May 1964

4. DESCRIPTIVE NOTES *(Type of report and inclusive dates)*

5. AUTHOR(S) *(Last name, first name, initial)*

6. REPORT DATE
August 1965

7a. TOTAL NO. OF PAGES
221

7b. NO. OF REFS
53

8a. CONTRACT OR GRANT NO.

b. PROJECT NO.

c.

d.

9a. ORIGINATOR'S REPORT NUMBER(S)
C&OM-5

9b. OTHER REPORT NO(S) *(Any other numbers that may be assigned this report)*

10. AVAILABILITY/LIMITATION NOTICES
Qualified requestors may obtain copies of this report from DDC.
Released to the Clearing House for Federal Scientific and Technical Information, Springfield, Virginia 22151, for sale to the public.

11. SUPPLEMENTARY NOTES
Part II is published separately as report number C&OM-6 and is classified "Confidential".

12. SPONSORING MILITARY ACTIVITY
Clothing and Organic Materials Division, U. S. Army Natick Laboratories, Natick, Massachusetts 01762

13. ABSTRACT
These proceedings report the technical progress presented at a meeting called by the U. S. Army Natick Laboratories of those of its contractors who are engaged in research on armor penetration and on the development of armor materials. Included also are papers presented by U. S. Army Natick Laboratories research workers in the same fields. The papers represent the status of contract and in-house work in armor at the time of the meeting.

DD FORM 1 JAN 64 1473

Unclassified
Security Classification

14. KEY WORDS	LINK A		LINK B		LINK C	
	ROLE	WT	ROLE	WT	ROLE	WT
Materials	8					
Penetration	8					
Armor	9					
Armor plate	9					

INSTRUCTIONS

1. ORIGINATING ACTIVITY: Enter the name and address of the contractor, subcontractor, grantee, Department of Defense activity or other organization *(corporate author)* issuing the report.

2*a*. REPORT SECURITY CLASSIFICATION: Enter the overall security classification of the report. Indicate whether "Restricted Data" is included. Marking is to be in accordance with appropriate security regulations.

2*b*. GROUP: Automatic downgrading is specified in DoD Directive 5200.10 and Armed Forces Industrial Manual. Enter the group number. Also, when applicable, show that optional markings have been used for Group 3 and Group 4 as authorized.

3. REPORT TITLE: Enter the complete report title in all capital letters. Titles in all cases should be unclassified. If a meaningful title cannot be selected without classification, show title classification in all capitals in parenthesis immediately following the title.

4. DESCRIPTIVE NOTES: If appropriate, enter the type of report, e.g., interim, progress, summary, annual, or final. Give the inclusive dates when a specific reporting period is covered.

5. AUTHOR(S): Enter the name(s) of author(s) as shown on or in the report. Enter last name, first name, middle initial. If military, show rank and branch of service. The name of the principal author is an absolute minimum requirement.

6. REPORT DATE: Enter the date of the report as day, month, year; or month, year. If more than one date appears on the report, use date of publication.

7*a*. TOTAL NUMBER OF PAGES: The total page count should follow normal pagination procedures, i.e., enter the number of pages containing information.

7*b*. NUMBER OF REFERENCES: Enter the total number of references cited in the report.

8*a*. CONTRACT OR GRANT NUMBER: If appropriate, enter the applicable number of the contract or grant under which the report was written.

8*b*, 8*c*, & 8*d*. PROJECT NUMBER: Enter the appropriate military department identification, such as project number, subproject number, system numbers, task number, etc.

9*a*. ORIGINATOR'S REPORT NUMBER(S): Enter the official report number by which the document will be identified and controlled by the originating activity. This number must be unique to this report.

9*b*. OTHER REPORT NUMBER(S): If the report has been assigned any other report numbers *(either by the originator or by the sponsor)*, also enter this number(s).

10. AVAILABILITY/LIMITATION NOTICES: Enter any limitations on further dissemination of the report, other than those imposed by security classification, using standard statements such as:

(1) "Qualified requesters may obtain copies of this report from DDC."

(2) "Foreign announcement and dissemination of this report by DDC is not authorized."

(3) "U. S. Government agencies may obtain copies of this report directly from DDC. Other qualified DDC users shall request through _____."

(4) "U. S. military agencies may obtain copies of this report directly from DDC. Other qualified users shall request through _____."

(5) "All distribution of this report is controlled. Qualified DDC users shall request through _____."

If the report has been furnished to the Office of Technical Services, Department of Commerce, for sale to the public, indicate this fact and enter the price, if known.

11. SUPPLEMENTARY NOTES: Use for additional explanatory notes.

12. SPONSORING MILITARY ACTIVITY: Enter the name of the departmental project office or laboratory sponsoring *(paying for)* the research and development. Include address.

13. ABSTRACT: Enter an abstract giving a brief and factual summary of the document indicative of the report, even though it may also appear elsewhere in the body of the technical report. If additional space is required, a continuation sheet shall be attached.

It is highly desirable that the abstract of classified reports be unclassified. Each paragraph of the abstract shall end with an indication of the military security classification of the information in the paragraph, represented as *(TS)*, *(S)*, *(C)*, *or (U)*.

There is no limitation on the length of the abstract. However, the suggested length is from 150 to 225 words.

14. KEY WORDS: Key words are technically meaningful terms or short phrases that characterize a report and may be used as index entries for cataloging the report. Key words must be selected so that no security classification is required. Identifiers, such as equipment model designation, trade name, military project code name, geographic location, may be used as key words but will be followed by an indication of technical context. The assignment of links, rules, and weights is optional.